A SYSTEM-BASED MODELING AND SIMULATION OF A FLOATING PRODUCTION STORAGE AND OFFLOADING (FPSO) ELECTRIC POWER SYSTEMS AND CORE LOSS ANALYSIS OF SYNCHRONOUS GENERATOR AND INDUCTION MOTOR

A Dissertation

by

ABDULKADIR BOSTANCI

Submitted to the Office of Graduate and Professional Studies of
Texas A&M University
in partial fulfillment of the requirements for the degree of

DOCTOR OF PHILOSOPHY

Chair of Committee,	Hamid A. Toliyat
Committee Members,	Le Xie
	Shankar P. Bhattacharyya
	Won-Jong Kim
Head of Department,	Miroslav M. Begovic

May 2017

Major Subject: Electrical Engineering

ABSTRACT

In this dissertation, a system based modeling and simulation were investigated for FPSO power system components and a few experimental results were evaluated to determine core losses in a synchronous generator under non-sinusoidal current.

Modeling and simulation results are presented to predict both the utility and the motor side challenges caused by different harmonic distortion levels. VFD was modeled as a rectifier and an inverter isolated by the DC link in the middle of the rectifier and the inverter in order to have faster and more accurate analysis of harmonics on both the utility and the motor side. Finite element analysis shows that reducing current harmonic level causes lower core losses in the machine.

Each component from the simulation, specifically synchronous generator, phase shifting transformer, multipulse rectifier, multilevel inverter, umbilical cable and induction motor, can be replaced or combined with any other topologies which is one of the biggest benefits of the system based modeling and simulation.

DEDICATION

I dedicate my dissertation to

My mother for her prayers which make me feel safe all the time

My father for being my guide

My grandmother and my sisters for their love

My lovely wife for her support

ACKNOWLEDGEMENTS

I would like to thank my advisor, Dr. Hamid A. Toliyat, for his guidance and support throughout my Ph.D. study.

I thank my committee members, Dr. Xie Le, Dr. Shankar P. Bhattacharyya, and Dr. Won-Jong Kim, for their contributions and supports.

I thank my colleagues at the Advanced Electric Machines and Power Electronics Laboratory. Thanks to my friends Mustafa, Gokhan, Burak, Yusuf, Ufuk, Yasin, and Celal. I also thank my brother Eyup Cem Erdogan.

Finally, thanks to my family for their encouragement and to my wife for her patience and love.

CONTRIBUTORS AND FUNDING SOURCES

This work was supervised by a dissertation committee consisting of Professor Hamid A. Toliyat and Professors Xie Le and Shankar P. Bhattacharyya of the Department of Electrical Engineering and Professor Won-Jong Kim of the Department of Mechanical Engineering. All work for the dissertation was completed independently by the student.

The student has been sponsored by Turkish Educational Department during his Ph.D. at Texas A&M University.

TABLE OF CONTENTS

Page

LIST OF FIGURES

Page

LIST OF TABLES

Page

1. INTRODUCTION

Decreasing of the onshore oil and gas reserves pushed the oil companies to search for offshore reserves to fulfill their production needs. Although there are large reserves under the seabed, accessing them is much harder than accessing onshore reserves. Oil has been produced from offshore since the 1950s but oil exploration moved to deeper waters further from the shore in the 1970s; thus, floating production systems have started to be used. Floating, Production, Storage and Offloading (FPSO) systems are floating vessels located near oil platforms. A FPSO may produce up to 300,000 barrels of oil per day (BOPD) and it may store more than two million barrel of on-board oil in the vessel. In the beginning, converted tankers were used for floating oil production systems.

Due to the development on the FPSO technology, more modern systems have been built. The offshore electrical generation and distribution design depends on the driver system selection. FPSOs include large rotating equipment such as large compressors, large pumps and large generators. The drivers for the large compressors and pumps must be determined before determining the power generation system [1]. The rotating components such as compressors and pumps used to be driven by gas turbines. However, the gas turbines are being replaced by electric motors such as induction motors. In recent years, gas turbines have only been used for power generation. Variable frequency drive systems (VFDs) are becoming more popular to drive the large electric motors which are connected to the compressors and pumps on a FPSO. Although there are numerous benefits to installing VFDs, there are some disadvantages. Inrush current or voltages and high orders

of current harmonics are the main downsides of the VFDs [2]. These harmonics cause more core losses in both generators and motors. In this dissertation, core losses in a synchronous generator and induction motor are described with the finite element analysis (FEA) simulations and experimental studies.

The VFD is located between the utility and the motors, and it includes a transformer, a rectifier, and an inverter. Multi-winding phase-shifting transformers allow the reduction of the harmonic levels produced by rectifiers. Transformers also limit the short circuit power which may be provided by the grid and they provide great isolation between the utility and semiconductors [2]. The transformer's number of windings depends on the number of pulses of the rectifier and the level of the multilevel inverter.

Umbilical cables are used to deliver the power to the motors located under the sea. These cables cannot be evaluated in the same way as onshore power distribution cables. Resonance issues are challenges to installing umbilical cables which causes motor starting issues [3].

Due to the size, cost and environmental challenges of the FPSO systems, simulation and smaller scale experimental analysis are important to predict future problems. In this study, the main power components from the generator to the motor shown in Figure 1 are simulated and the results are discussed. System based simulations simplify the improvement of each component, which can be replaced with new topologies. These main power components are only part of the FPSO power systems. The other power components are shown in a general electric schematic of a FPSO in Appendix A.

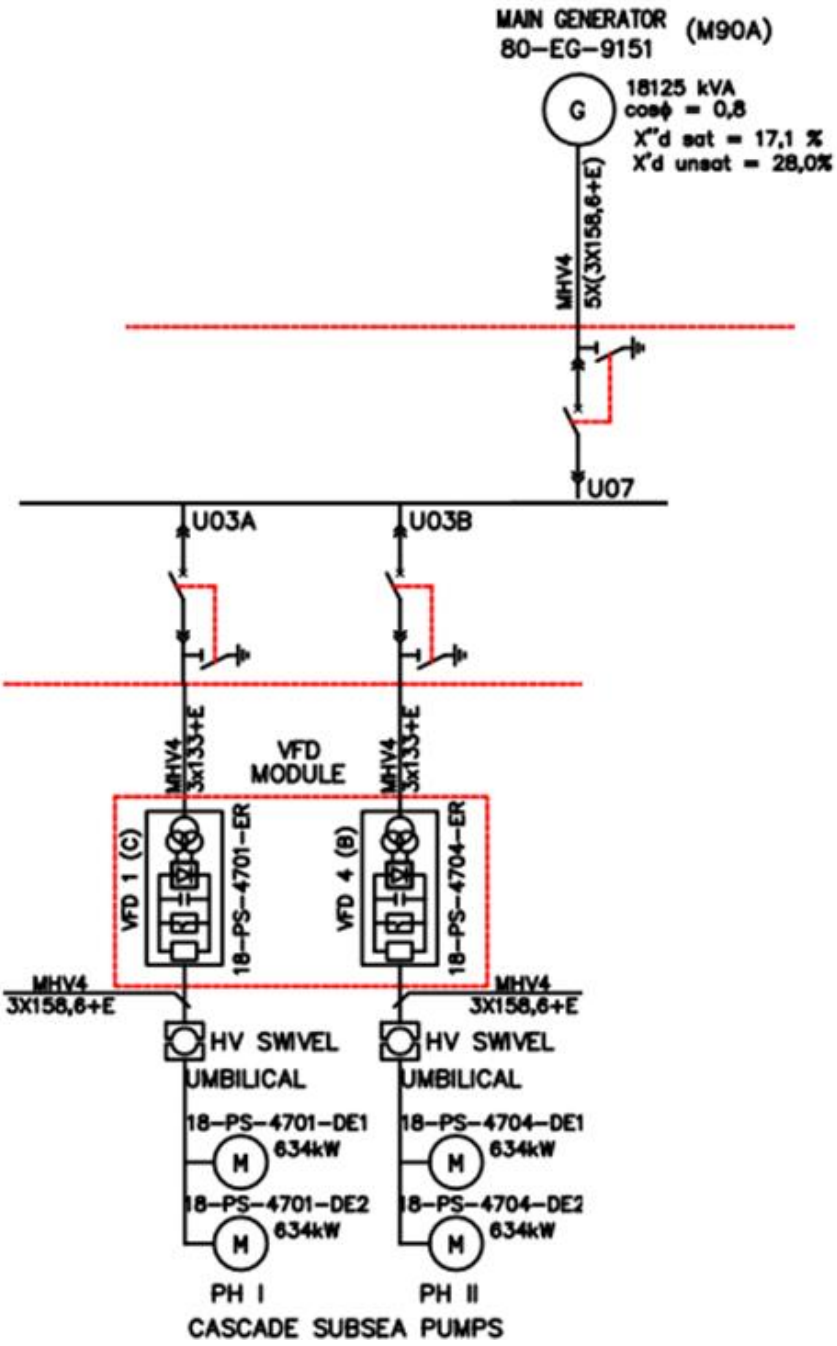

Figure 1: Main power system components

2. FLOATING PRODUCTION STORAGE AND OFFLOADING (FPSO) PLATFORMS

In recent years, FPSOs are becoming more popular with the oil industry as it tends to search for more offshore sources. These systems are designed to be an alternative to other types of offshore oil production systems such as fixed oil platforms. FPSOs are huge and costly floating vessels which can cost up to 1 billion dollars. They are equipped with the technology for separation and treatment of crude oil, gas and water. Produced fluid oil and gas from sub-sea arrive on board through flexible pipelines. FPSOs have a huge capacity for storage and are able to transfer stored oil and gas to the shore using shuttle tankers. Figure 2 shows a typical FPSO while transferring stored oil to a shuttle tanker.

Figure 2: Typical FPSO while transferring oil to a shuttle tanker adapted from [4]

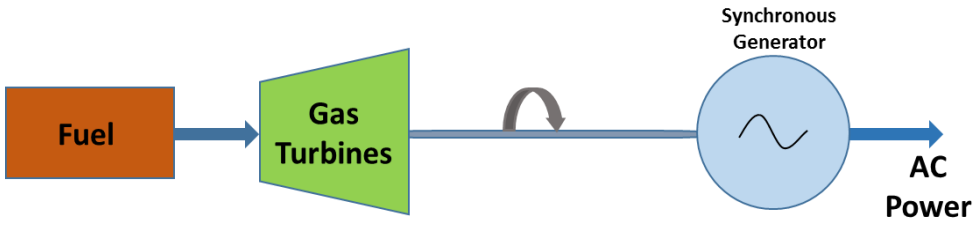

Figure 3: Gas turbines are used for power generation

FPSOs are also grid free power supplies to oil production systems. Treated gas is used for power generation, and one of the biggest advantages of an FPSO is that produced gas is processed and used in gas turbines as shown in Figure 3. An FPSO can supply multiple oil platforms or mobile sub-sea oil pumps as shown in Figure 4. These oil production units need electrical power to inject water to the reserve and to pump the oil and gas to the earth's surface. Subsea umbilical cables are used for energy distribution to the subsea and oil platforms. The power cables and other flexible pipelines must be protected from damage due to the harsh offshore weather conditions. Therefore, turret mooring technology is used for FPSOs.

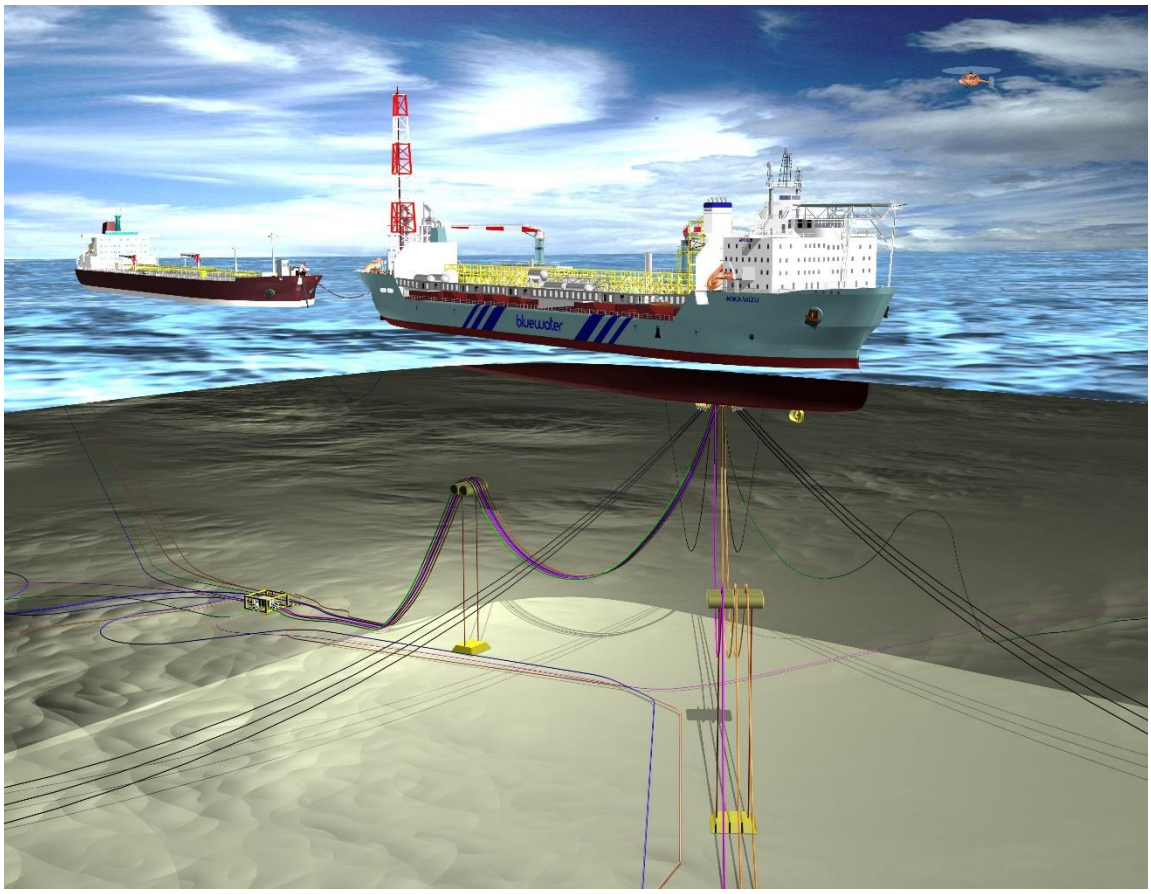

Figure 4: Multiple oil pumping systems can be supplied by an FPSO adapted from [4]

2.1 Turret Mooring System

All of the power cable and pipelines going to the oil platforms and sea-bed pumps go through the turret, which is attached to the hull of the vessel. The turret mooring system is an essential feature of an FPSO. The turret is moored to the seabed with chains, anchors, and wires. It also has a bearing system that allows the FPSO free 360° rotation around the

turret. Therefore, strong winds occurring offshore cannot force the subsea cables and pipelines to move and be damaged. Figure 5 shows the connection of the mooring chairs and anchors under the sea.

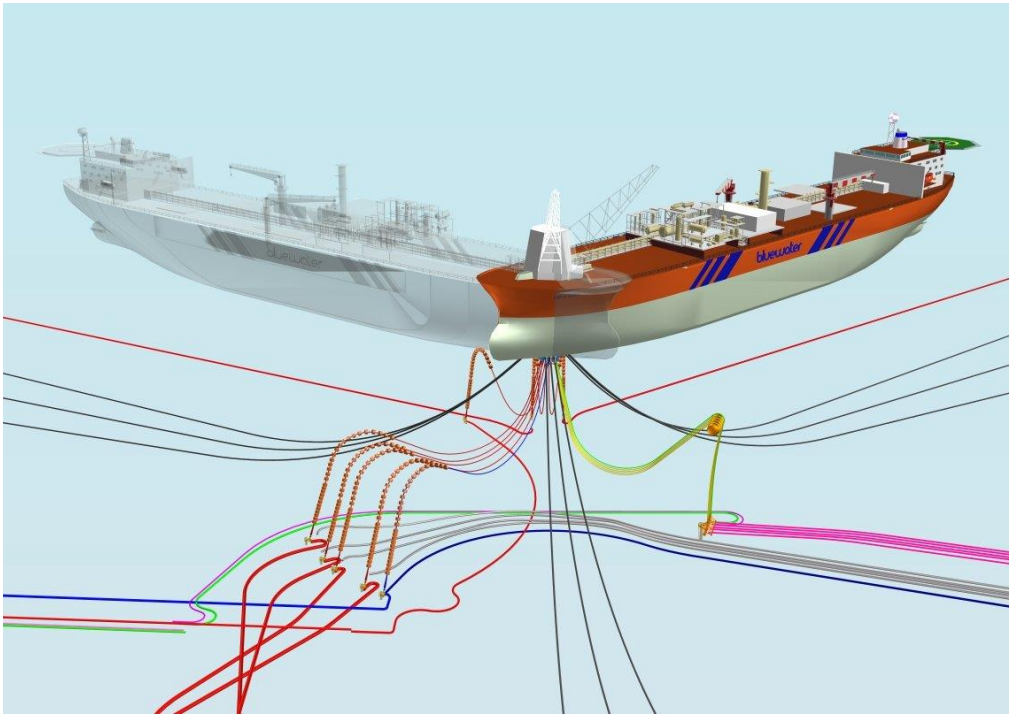

Figure 5: Turret mooring system adapted from [4]

2.2 Main Electric Power Components of an FPSO

Most of the parts used for oil and gas production demand electrical power. Figure 6 shows the electrical power components on a FPSO. The main equipment on a FPSO consists mostly of electrically driven systems such as compressors and pumps. Machine

drive systems, such as VFDs, increase the efficiency, availability and reliability [3]. However, VFDs includes many semiconductors, which produce high current harmonic distortions. These harmonic distortions produce different challenges on both the generator side and the motor side.

The motor drive system is connected between the generator and the motors in order to adjust the desired voltage and current for the motors. The motors are connected to electrical submersible pump (ESP) systems which are able to pump the offshore oil and gas through umbilical subsea cables. The components of a simplified main power system are illustrated in Figure 7. Gas turbines are usually used as a prime mover for the generators on a FPSO. ESP systems are used to pump the oil and gas, and these pumps are usually operated with induction motors.

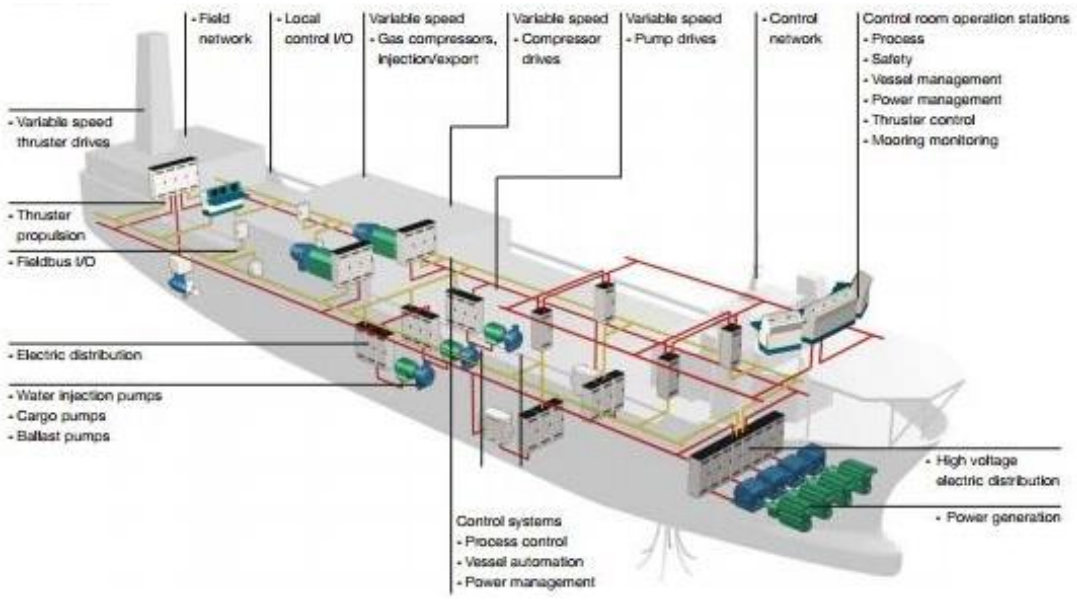

Figure 6: Power system components on a FPSO adapted from [5]

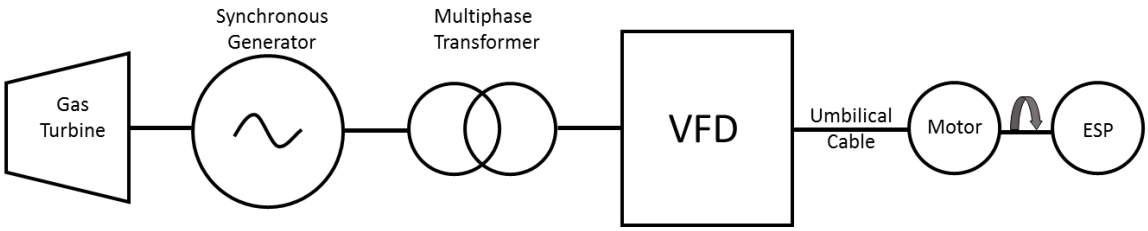

Figure 7: Simplified power system components on a FPSO

3. POWER SYSTEM COMPONENTS

In this section, the main power system components of a FPSO; synchronous generator, phase-shifting transformer, VFD, subsea cable and induction motor as shown in Figure 8 will be described.

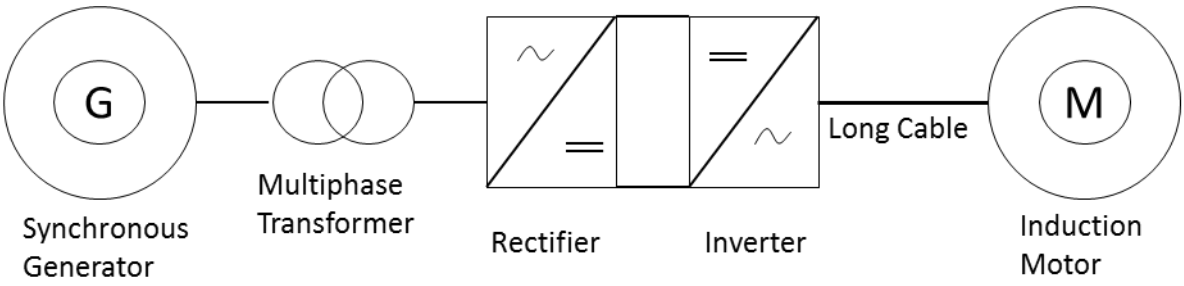

Figure 8: The main power components used for this dissertation

3.1 Synchronous Generator

Synchronous generators are commonly used for power generation. They are high efficient electric machines. Generated waveform is synchronized with the rotor speed and the frequency can be easily calculated by f=N*P/120. Where P is the number of the poles and N is the speed of the rotor. Synchronous generator can be started by exciting the rotor field with a DC source. However, permanent magnet synchronous generators do not require a DC excitation.

Synchronous generators used for FPSOs are huge generators. They can be up to 40-50 MW. In given electric schematic of the FPSO, 18 MW synchronous generator has been used. However, simulations and experimental results have been obtained on a smaller scale synchronous generator which will be described in following sections.

Although synchronous generators are high efficient machines, the efficiency can be lower due to the high harmonic distortions at the output of the generators. Variable frequency drive used to drive induction motors on a FPSO are the main harmonic producers which cause higher copper and core losses in the synchronous generator. Therefore, determining harmonic content is very important in order to maintain generator efficiency at high values.

3.2 Medium Voltage Variable Frequency Drives

Variable frequency converters are connected as an interface between the utility supply and the induction motor. VFDs must be able to maintain the following requirements: adjusting the frequency to the required output speed, adjusting the output voltage in order to have constant air gap flux in constant torque region, and supplying continuous rated current at any frequency [6].

Medium voltage drives have voltage ratings from 2.3kV to 13.8kV, and they are mostly used for fan, compressor, and pump applications [7]. Although VFDs generate a large amount of harmonics and heat, they are widely used because of their economic and operation benefits. VFDs mostly provide economic benefits to fans and pumps. For

instance, when a pump runs at 80% of full speed, it uses around 50% of full load power. The other economic benefit is the reduction of maintenance when using a VFD; there is no need to use mechanical speed control gearboxes.

VFDs basically consist of a rectifier and an inverter. The rectifier converts the AC supply voltage to a DC voltage at the output, and the inverter converts this DC voltage to an adjustable AC voltage and frequency. VFDs can be categorized as uncontrolled DC bus VFDs, which are shown in Figure 9, and controlled DC bus VFDs, which are shown in Figure 10. For uncontrolled DC bus VFDs, diode rectifiers are used with a fixed DC voltage, and they are commonly used for motor drives. However, in controlled DC bus VFDs, the DC bus voltage is flexible and is controlled using semiconductors.

Rectifiers produce high harmonic distortions and North American and European standards such as IEEE Standard 519-1992 limit the harmonic distortion level [8]. Therefore, multipulse rectifiers are commonly used in the most motor drive applications.

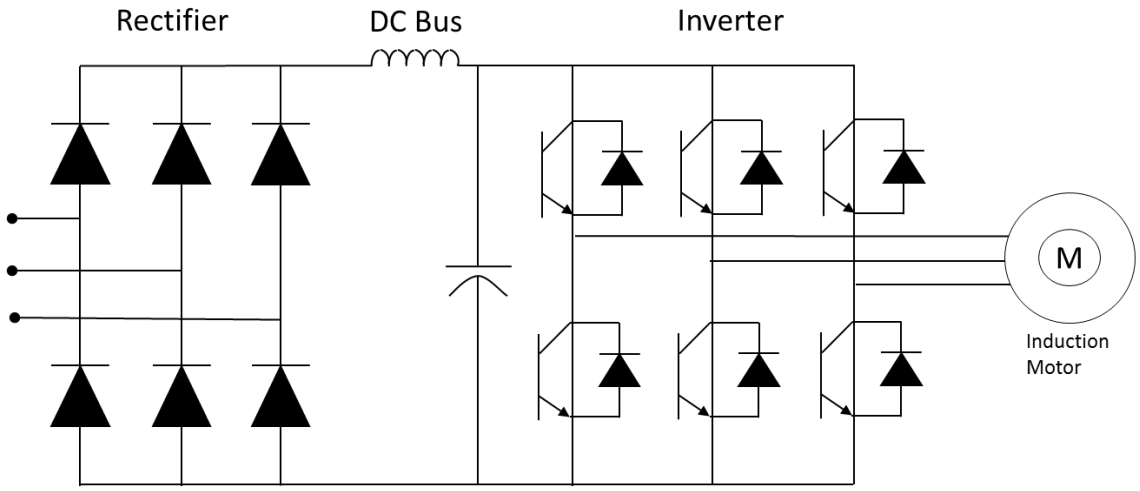

Figure 9: Uncontrolled DC bus VFD

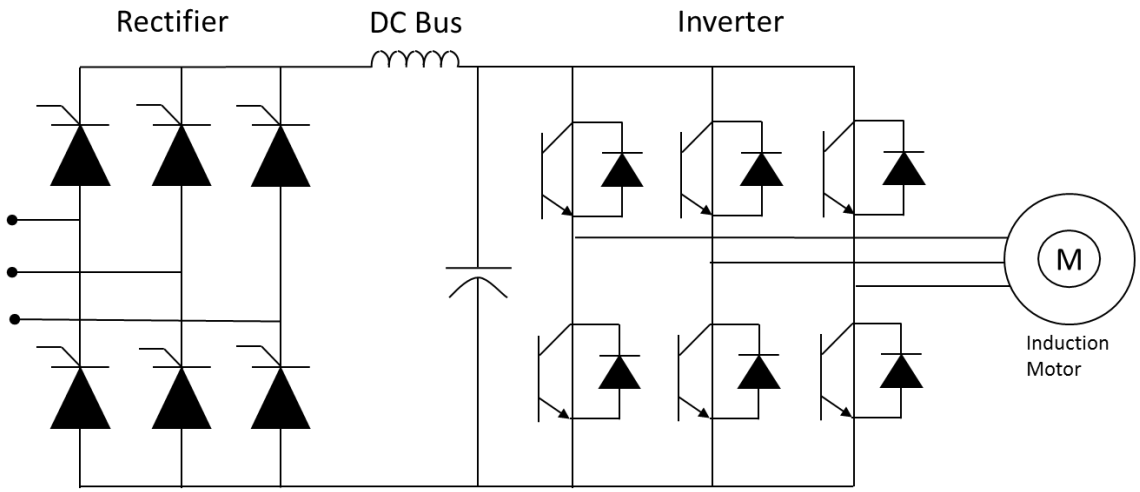

Figure 10: Controlled DC bus VFD

3.3 Multipulse Diode Rectifier

Harmonic requirements are the motivation for the use of multipulse diode rectifiers by most of the high-power drive manufacturers. These requirements are set by the harmonic standards [8]. Multipulse rectifiers are used with phase shifting transformers, which are able to reduce the current harmonic distortions. Some of the low-order harmonics generated by six pulse rectifiers are cancelled by those transformers. Increasing the pulse number of the rectifier reduces line current harmonics. 30-pulse rectifiers or more are rarely used in practice because increasing the number of pulses increases the cost of the transformers without significant performance improvement. Another advantage of the phase shifting transformer is to block the common-mode voltages generated by

rectifiers and inverters. This protects the motor terminals from the premature winding insulation failure caused by the common-mode voltages [9].

3.3.1 Six-Pulse Diode Rectifier

A simplified model of a six-pulse rectifier is shown in Figure 11. v_a, v_b and v_c are the AC phase voltages. Assuming all diodes are ideal with no voltage drop and no loss. The phase voltages;

$$v_a = \sqrt{2}V_{PH}sin(\omega t)$$

$$v_b = \sqrt{2}V_{PH}sin(\omega t - 2\pi/3)$$

$$v_c = \sqrt{2}V_{PH}sin(\omega t - 4\pi/3)$$

V_{PH}: rms phase voltage

ω : angular frequency $\omega = 2\pi f$

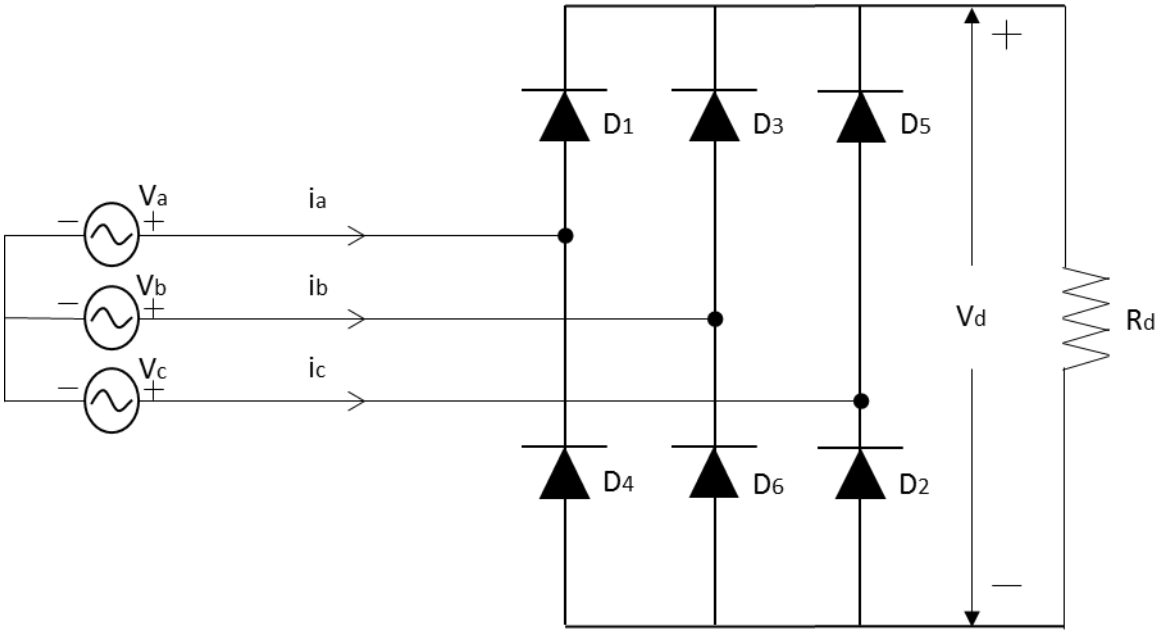

Figure 11: Six pulse diode rectifier with a resistive load adapted from [9]

The line to line voltage can be calculated as follows;

$$v_{ab} = v_a - v_b = \sqrt{2}V_{LL}sin(\omega t + \pi/6)$$

V_{LL}: rms value of the line to line voltage $V_{LL} = \sqrt{3}V_{PH}$

The average DC voltage, $V_{davg} = \frac{1}{\pi/3}\int_{\pi/6}^{\pi/2}\sqrt{2}V_{LL}\sin(\omega t + \pi/6)d(\omega t) = \frac{3\sqrt{2}}{\pi}V_{LL}$

The DC voltage V_d has 6 pulses per cycle of the AC voltage source frequency, which is why it is called a six-pulse rectifier, and the phase current i_a has 2 pulses per half cycle of the source frequency as shown in Figure 12.

For six pulse rectifiers, the total harmonic distortion is too high, but it decreases as the pulse number of the rectifier increases. This will be discussed in following chapters.

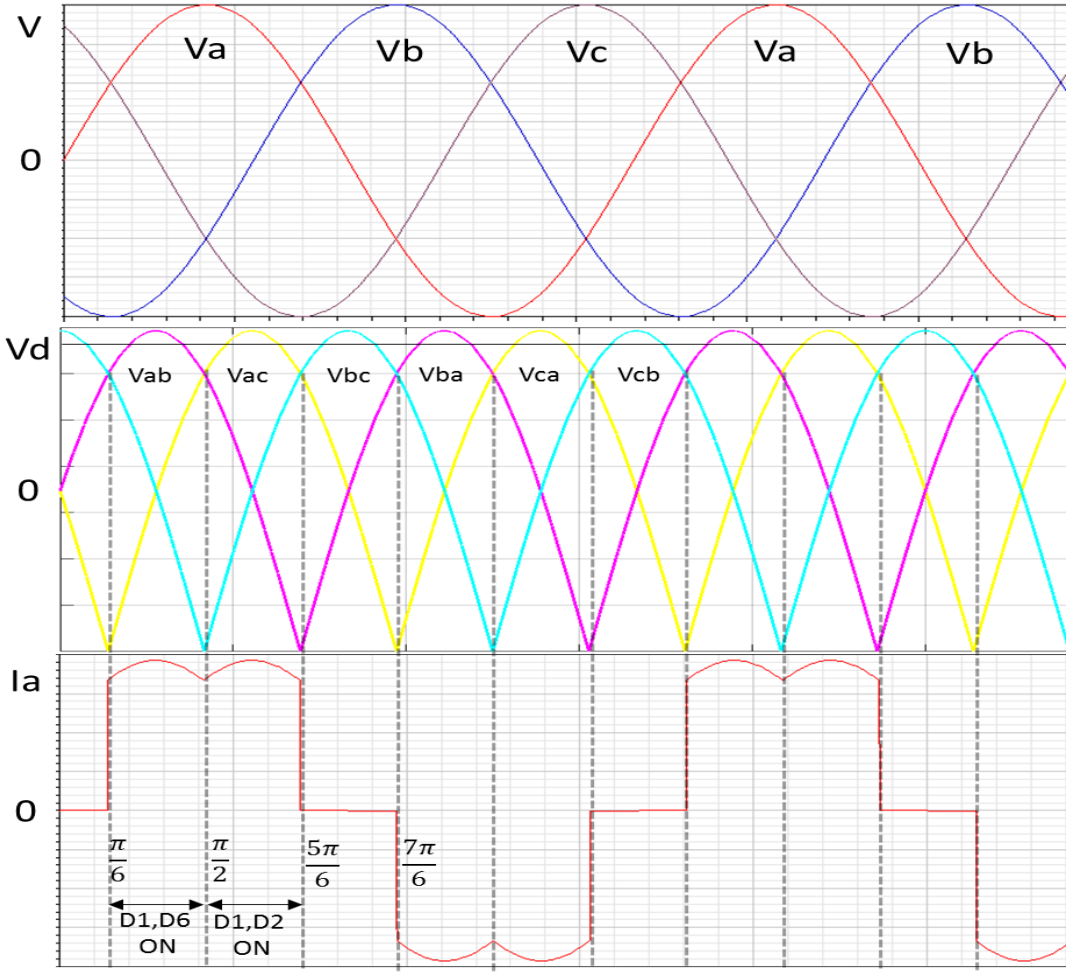

Figure 12: Six pulse diode rectifier waveforms with a resistive load adapted from [9]

3.3.2 Series Type of Multipulse Diode Rectifier

Figure 13 shows the 12 pulse series type of diode rectifier, which is supplied by a phase shifting transformer. The transformer has two secondary windings for each phase in order to supply two series connected six pulse rectifiers. To achieve the desired phase shifting angle $\delta = \frac{60}{\#\ of\ six\ pulse\ rectifiers}$ between secondary windings, the upper secondary windings are connected as a wye connection and the lower secondary windings are connected as a delta connection. If the rectifiers have more than 12 pulses, the phase shifting angle can be adjusted by making zigzag connections in the secondary windings of the transformer, which will be discussed later. C_d is the DC filter capacitance, which is usually selected to be sufficiently large to have no ripple in the DC voltage V_d. Simulation results for the primary side current waveforms and harmonic analysis will be discussed in following sections for the series type of the rectifier up to 36 pulses [9].

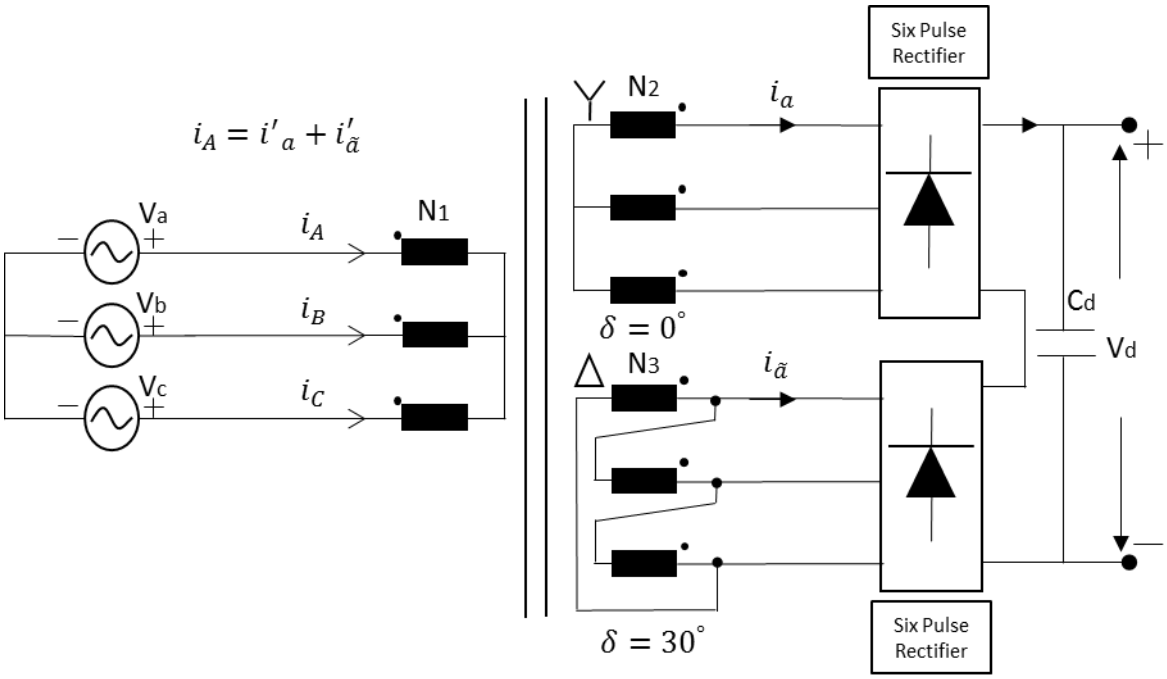

Figure 13: Series type 12-pulse rectifier adapted from [9]

3.3.3 Separate Type of Multipulse Diode Rectifier

The difference from the series type of 12 pulse rectifier is that each six pulse rectifier is connected to different DC loads instead of a single DC load. These rectifiers are used with cascaded H-bridge multilevel inverter drives. The pulse number of the rectifier can be increased based on the desired multilevel inverter level. Each six pulse rectifier supplies an isolated DC voltage to cascaded H-bridge inverters. The phase shifting transformer again has six windings on the secondary side for a 12 pulse diode rectifier; the upper three windings are wye connected and the lower three windings are delta connected in order to achieve the desired phase shifting as shown in Figure 14 [9].

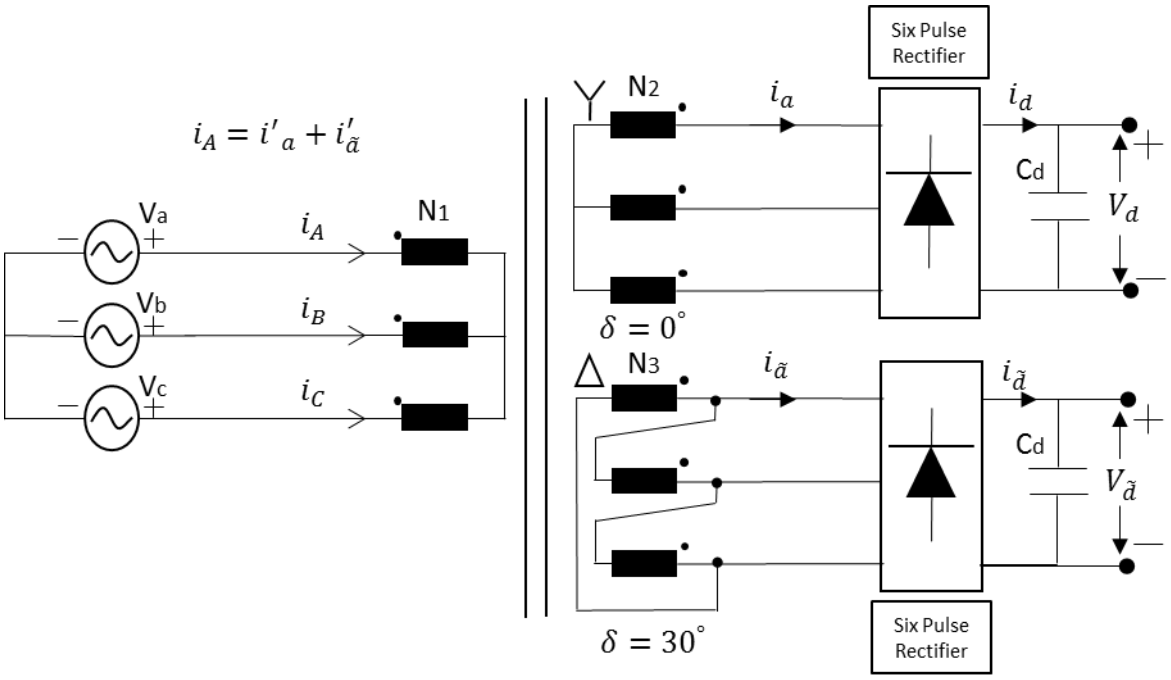

Figure 14: Separate type 12-pulse diode rectifier adapted from [9]

3.4 Phase-Shifting Transformers

Phase-shifting transformers are designed for non-linear loads in order to reduce current harmonic distortions. They usually have multi-windings in the secondary side of the transformer, thus multiphase nonlinear loads can be connected. Using phase-shifting transformers is mandatory for multipulse diode rectifiers. They provide three main advantages: electric isolation between the utility supply and the rectifier, harmonic cancellation by phase displacement, and a proper secondary side voltage [9].

3.4.1 Harmonic Current Cancellation

This section explains the phase displacement of the current harmonics when the secondary side of the phase shifting transformer is referred to the primary side. This method shows that certain current harmonics are cancelled by the phase displacement. Figure 15 shows a nonlinear load connected to a delta/wye transformer. This nonlinear load can be a six pulse rectifier [9].

Assuming windings turns ratio, $\frac{N_1}{N_2} = \sqrt{3}$

the voltage ratio becomes, $\frac{V_{AB}}{V_{ab}} = \sqrt{3}$

The line currents of the non-resistive load can be expressed by the following equations for a balanced three-phase system.

$$i_a = \sum_{n=1,5,7,11,13,\ldots}^{\infty} I_n \sin(n\omega t) \ldots$$

$$i_b = \sum_{n=1,5,7,11,13,\ldots}^{\infty} I_n \sin(n(\omega t - 120°)) \ldots$$

$$i_c = \sum_{n=1,5,7,11,13,\ldots}^{\infty} I_n \sin(n(\omega t - 240°)) \ldots$$

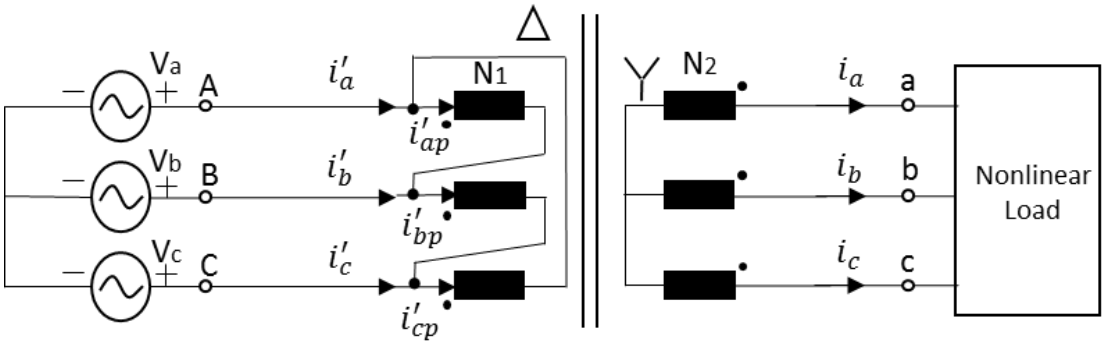

Figure 15: Harmonic currents in both sides of the transformer adapted from [9]

i'_{ap} and i'_{bp} are the secondary side currents referred to the primary side of the phase shifting transformer and I_n is the peak value of the nth order current harmonic.

$$i'_{ap} = i_a \frac{N_2}{N_1} = \frac{1}{\sqrt{3}}(I_1 \sin(\omega t) + I_5 \sin(5\omega t) + I_7 \sin(7\omega t) + I_{11} \sin(11\omega t) + I_{13} \sin(13\omega t) + \cdots)$$

$$i'_{bp} = i_a \frac{N_2}{N_1} = \frac{1}{\sqrt{3}}(I_1 \sin(\omega t - 120°) + I_5 \sin(5\omega t - 240°) + I_7 \sin(7\omega t - 120°) + I_{11} \sin(11\omega t - 240°) + I_{13} \sin(13\omega t - 120°) + \cdots)$$

The primary current can be described as

$$i'_a = i'_{ap} - i'_{bp}(I_1 \sin(\omega t + 30°) + I_5 \sin(5\omega t - 30°) + I_7 \sin(7\omega t + 30°) + I_{11} \sin(11\omega t - 30°) + I_{13} \sin(13\omega t + 30°) + \cdots)$$

$$i'_a = \sum_{n=1,7,13,19,\ldots}^{\infty} I_n \sin(n\omega t - \delta) + \sum_{n=5,11,17,23,\ldots}^{\infty} I_n \sin(n\omega t + \delta)$$

Positive sequence harmonics Negative sequence harmonics

When the secondary side currents are referred to the primary side of the phase-shifting transformer, the relationship between the phase angles of the harmonic current can be expressed as;

$\angle i'_{an} = \angle i_{an} - \delta$ for n = 1,7,13,19… Positive sequence harmonics

$\angle i'_{an} = \angle i_{an} + \delta$ for n = 5,11,17,23… Negative sequence harmonics

The above equations are valid for any values of δ.

As explained before, multipulse rectifiers are used with phase shifting transformers. Increasing the pulse number of the multipulse rectifier moves the dominant current harmonics to higher orders. The following example investigates the harmonic cancellation of the 12 pulse rectifier by a phase shifting transformer as shown in Figure 16 [9].

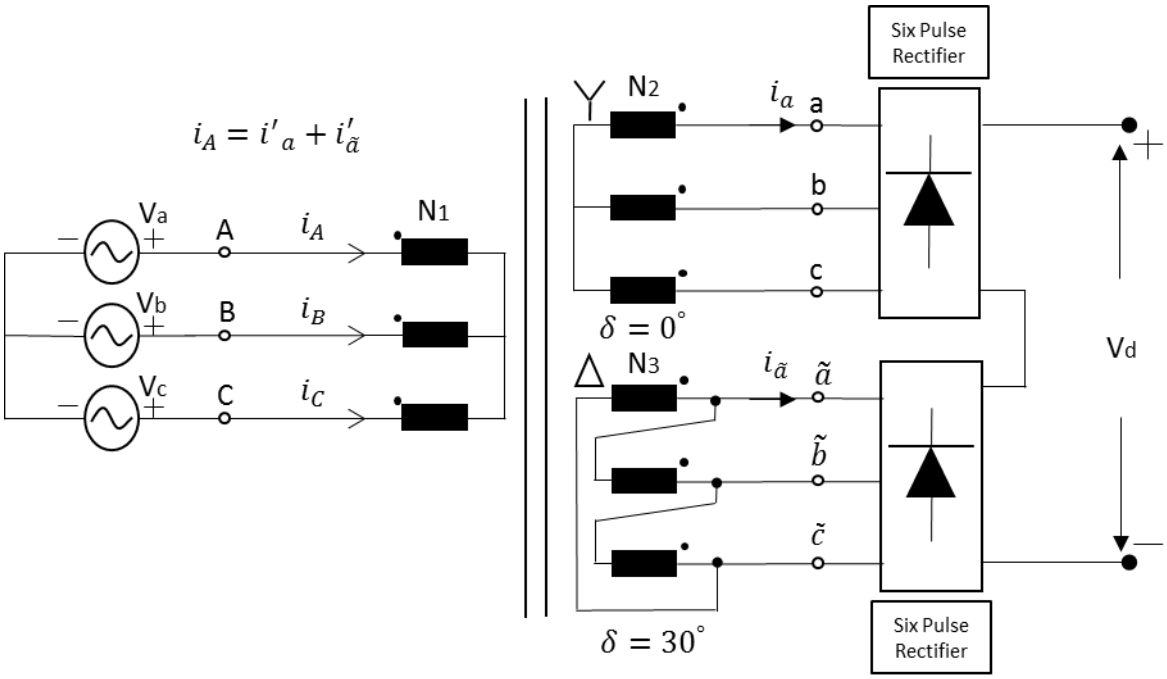

Figure 16: Harmonic current cancellation of 12 pulse rectifier adapted from [9]

Assuming the voltage ratio is $\frac{V_{AB}}{V_{ab}} = \frac{V_{AB}}{V_{\tilde{a}\tilde{b}}} = 2$ and the phase shifting angle δ of the secondary side windings are 0° and 30° respectively because of the wye/delta connection in the secondary side of the transformer, the secondary side line currents can be described as

$$i_a = \sum_{n=1,5,7,11,13,\ldots}^{\infty} I_n \sin(n\omega t) \ldots$$

$$i_{\tilde{a}} = \sum_{n=1,5,7,11,13,\ldots}^{\infty} I_n \sin(n(\omega t + \delta) \ldots$$

The phase angles of all the harmonic currents of the primary side referred current i'_a remain the same because of the wye/wye connection. However, they change for the referred current $i'_{\tilde{a}}$ because of delta connection.

$$i'_a = \frac{1}{2}(I_1 \sin(\omega t) + I_5 \sin(5\omega t) + I_7 \sin(7\omega t) + I_{11} \sin(11\omega t) + I_{13} \sin(13\omega t) + \cdots)$$

$$i'_{\tilde{a}} = \frac{1}{2}\left(\sum_{n=1,7,13,\ldots}^{\infty} I_n \sin(n(\omega t + \delta) - \delta) + \sum_{n=5,11,17,\ldots}^{\infty} I_n \sin(n(\omega t + \delta) + \delta)\right)$$

For $\delta = 30°$

$$i'_{\tilde{a}} = \frac{1}{2}(I_1 \sin(\omega t) - I_5 \sin(5\omega t) - I_7 \sin(7\omega t) + I_{11} \sin(11\omega t) + I_{13} \sin(13\omega t) - \cdots)$$

The primary side line current can be calculated as

$$i_A = i'_a + i'_{\tilde{a}} = I_1 \sin \omega t + I_{11} \sin \omega t + I_{13} \sin \omega t + I_{23} \sin \omega t + \cdots$$

where the dominant current harmonics are the 11th and 13th, and the 5th, 7th, 17th, and 19th harmonic currents are $180°$ out of phase, which means that they are cancelled. The following sections will give more examples of this harmonic cancellation with simulation results.

3.4.2 Mathematical Model of the Three-Phase Transformer

There are three windings in each side of the transformer: a_p, b_p, and c_p represent primary side windings and a_s, b_s and c_s represent secondary side windings of the transformer a shown in Figure 17.

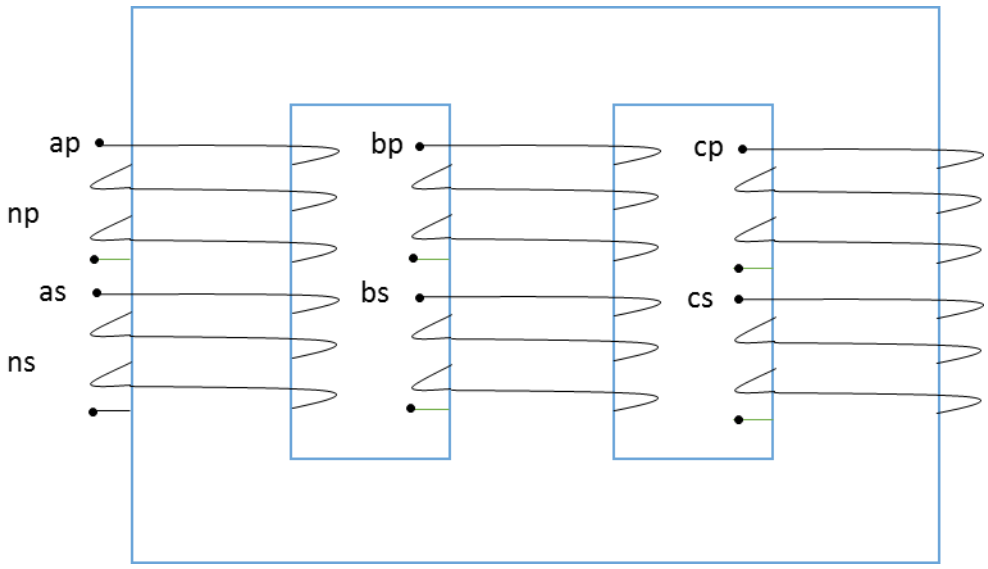

Figure 17: Three-phase transformer windings

Terminal voltages equations

$$V_{ap} = r_{ap} i_{ap} + \frac{d\lambda_{ap}}{dt}$$

$$V_{bp} = r_{bp} i_{bp} + \frac{d\lambda_{bp}}{dt}$$

$$V_{cp} = r_{cp} i_{cp} + \frac{d\lambda_{cp}}{dt}$$

$$V_{as} = r_{as} i_{as} + \frac{d\lambda_{as}}{dt}$$

$$V_{bs} = r_{bs} i_{bs} + \frac{d\lambda_{bs}}{dt}$$

$$V_{cs} = r_{cs} i_{cs} + \frac{d\lambda_{cs}}{dt}$$

Flux linkages for primary side windings

$$\lambda_{ap} = \left(L_{lp} + L_{apap}\right) i_{ap} + L_{apbp} i_{bp} + L_{apcp} i_{cp} + L_{apas} i_{as} + L_{apbs} i_{bs} + L_{apcs} i_{cs}$$

$$\lambda_{bp} = \left(L_{lp} + L_{bpbp}\right) i_{bp} + L_{apbp} i_{ap} + L_{bpcp} i_{cp} + L_{bpas} i_{as} + L_{bpbs} i_{bs} + L_{bpcs} i_{cs}$$

$$\lambda_{cp} = \left(L_{lp} + L_{cpcp}\right) i_{cp} + L_{apcp} i_{ap} + L_{bpcp} i_{bp} + L_{cpas} i_{as} + L_{cpbs} i_{bs} + L_{cpcs} i_{cs}$$

Flux linkages for secondary side windings,

$$\lambda_{as} = (L_{ls} + L_{asas}) i_{as} + L_{asbs} i_{bs} + L_{ascs} i_{cs} + L_{asap} i_{ap} + L_{asbp} i_{bp} + L_{ascp} i_{cp}$$

$$\lambda_{bs} = (L_{ls} + L_{bsbs}) i_{bs} + L_{asbs} i_{as} + L_{bscs} i_{cs} + L_{bsap} i_{ap} + L_{bsbp} i_{bp} + L_{bscp} i_{cp}$$

$$\lambda_{cs} = (L_{ls} + L_{cscs}) i_{cs} + L_{ascs} i_{as} + L_{bscs} i_{bs} + L_{csap} i_{ap} + L_{csbp} i_{bp} + L_{cscp} i_{cp}$$

L_{lp} : self inductance

L_{apap}: magnetizing inductance

L_{apbp}: mutual inductance

$$L_{apap} = L_{bpbp} = L_{cpcp} = K_s N_p^2 \mathrel{\widehat{=}} L_{sp}$$

$$L_{apbp} = L_{apcp} = L_{bpcp} = -K_m N_p^2 \mathrel{\widehat{=}} -L_{mp}$$

$$L_{asas} = L_{bsbs} = L_{cscs} = K_s N_s^2 \mathrel{\widehat{=}} L_{ss}$$

$$L_{asbs} = L_{ascs} = L_{bscs} = -K_m N_s^2 \mathrel{\widehat{=}} -L_{ms}$$

$$L_{apas} = L_{bpbs} = L_{cpcs} = K_s N_p N_s \mathrel{\widehat{=}} L_{sps}$$

$$L_{apbs} = L_{apcs} = L_{cpbs} = -K_m N_p N_s \mathrel{\widehat{=}} -L_{mps}$$

Voltage equations become

$$V_{ap} = r_p i_{ap} + L_{lp}\frac{di_{ap}}{dt} + L_{sp}\frac{di_{ap}}{dt} - \frac{1}{2}L_{sp}\frac{di_{bp}}{dt} - \frac{1}{2}L_{sp}\frac{di_{cp}}{dt} + L_{sp}\frac{di'_{as}}{dt} - \frac{1}{2}L_{sp}\frac{di'_{bs}}{dt} - \frac{1}{2}L_{sp}\frac{di'_{cs}}{dt}$$

$$V_{bp} = r_p i_{bp} + L_{lp}\frac{di_{bp}}{dt} + L_{sp}\frac{di_{bp}}{dt} - \frac{1}{2}L_{sp}\frac{di_{ap}}{dt} - \frac{1}{2}L_{sp}\frac{di_{cp}}{dt} + L_{sp}\frac{di'_{bs}}{dt} - \frac{1}{2}L_{sp}\frac{di'_{as}}{dt} - \frac{1}{2}L_{sp}\frac{di'_{cs}}{dt}$$

$$V_{cp} = r_p i_{cp} + L_{lp}\frac{di_{cp}}{dt} + L_{sp}\frac{di_{cp}}{dt} - \frac{1}{2}L_{sp}\frac{di_{ap}}{dt} - \frac{1}{2}L_{sp}\frac{di_{bp}}{dt} + L_{sp}\frac{di'_{cs}}{dt} - \frac{1}{2}L_{sp}\frac{di'_{as}}{dt} - \frac{1}{2}L_{sp}\frac{di'_{bs}}{dt}$$

$$V'_{as} = r'_s i'_{as} + L'_{ls}\frac{di'_{as}}{dt} + L_{sp}\frac{di'_{as}}{dt} - \frac{1}{2}L_{sp}\frac{di'_{bs}}{dt} - \frac{1}{2}L_{sp}\frac{di'_{cs}}{dt} + L_{sp}\frac{di_{ap}}{dt} - \frac{1}{2}L_{sp}\frac{di_{bp}}{dt} - \frac{1}{2}L_{sp}\frac{di_{cp}}{dt}$$

$$V'_{bs} = r'_s i'_{bs} + L'_{ls}\frac{di'_{bs}}{dt} + L_{sp}\frac{di'_{bs}}{dt} - \frac{1}{2}L_{sp}\frac{di'_{as}}{dt} - \frac{1}{2}L_{sp}\frac{di'_{cs}}{dt} + L_{sp}\frac{di_{bp}}{dt} - \frac{1}{2}L_{sp}\frac{di_{ap}}{dt} - \frac{1}{2}L_{sp}\frac{di_{cp}}{dt}$$

$$V'_{cs} = r'_s i'_{cs} + L'_{ls}\frac{di'_{cs}}{dt} + L_{sp}\frac{di'_{cs}}{dt} - \frac{1}{2}L_{sp}\frac{di'_{as}}{dt} - \frac{1}{2}L_{sp}\frac{di'_{bs}}{dt} + L_{sp}\frac{di_{cp}}{dt} - \frac{1}{2}L_{sp}\frac{di_{ap}}{dt} - \frac{1}{2}L_{sp}\frac{di_{bp}}{dt}$$

Since current equations

$$i_{ap} + i_{bp} + i_{cp} = 0 \Longrightarrow i_{ap} = -(i_{bp} + i_{cp})$$

$$i'_{as} + i'_{bs} + i'_{cs} = 0 \Longrightarrow i'_{as} = -(i'_{bs} + i'_{cs})$$

Final voltage equations

$$V_{ap} = r_p i_{ap} + L_{lp}\frac{di_{ap}}{dt} + \frac{3}{2}L_{sp}\frac{di_{ap}}{dt} + \frac{3}{2}L_{sp}\frac{di'_{as}}{dt}$$

$$V_{bp} = r_p i_{bp} + L_{lp}\frac{di_{bp}}{dt} + \frac{3}{2}L_{sp}\frac{di_{bp}}{dt} + \frac{3}{2}L_{sp}\frac{di'_{bs}}{dt}$$

$$V_{cp} = r_p i_{cp} + L_{lp}\frac{di_{cp}}{dt} + \frac{3}{2}L_{sp}\frac{di_{cp}}{dt} + \frac{3}{2}L_{sp}\frac{di'_{cs}}{dt}$$

$$V'_{as} = r'_s i'_{as} + L'_{ls}\frac{di'_{as}}{dt} + \frac{3}{2}L_{sp}\frac{di'_{as}}{dt} + \frac{3}{2}L_{sp}\frac{di_{ap}}{dt}$$

$$V'_{bs} = r'_s i'_{bs} + L'_{ls}\frac{di'_{bs}}{dt} + \frac{3}{2}L_{sp}\frac{di'_{bs}}{dt} + \frac{3}{2}L_{sp}\frac{di_{bp}}{dt}$$

$$V'_{cs} = r'_s i'_{cs} + L'_{ls}\frac{di'_{cs}}{dt} + \frac{3}{2}L_{sp}\frac{di'_{cs}}{dt} + \frac{3}{2}L_{sp}\frac{di_{cp}}{dt}$$

3.4.3 Mathematical Model of the Multi-Winding Phase-Shifting Transformer

In this study, three-phase in the primary side and 18-phase in the secondary side phase-shifting transformer is modeled. 18-phase in the secondary side supplies 36-pulse rectifier, each three phases are connected to each six pulse diode rectifiers. All windings are located in the same core as shown in Figure 18. Zigzag connection is used for the secondary side windings in order to achieve required phase shifting angle between the windings. In zigzag connection two windings needed for each secondary phase.

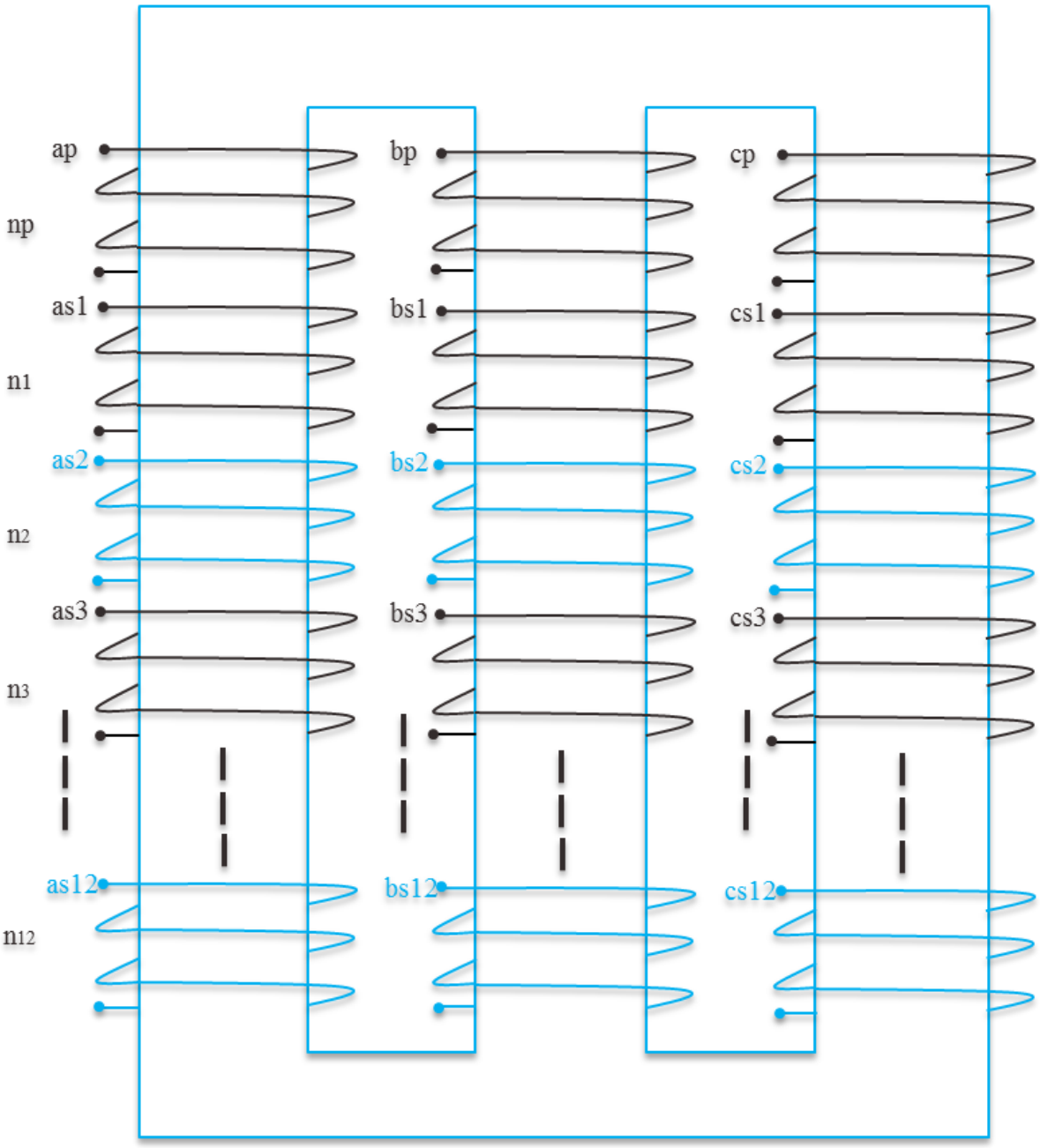

Figure 18: Multi-winding phase-shifting transformer windings

Same voltage equations are used for the calculations but each two secondary side windings are zigzag connected as shown in Figure 19. $V_{ax1}, V_{bx1}, and\ V_{cx1}$ are the new secondary side voltages for three phases and it continues up to $V_{ax6}, V_{bx6}, and\ V_{cx6}$. They must be in same voltage level but phase-shifted. As mentioned before phase shifting angle $\delta = {}^{60}/_{6} = 10°$ for the 18-phase phase-shifting transformer. Secondary side voltages waveform example is shown in Figure 20.

$$V_{ax1} = V_{as1} + V_{cs2}$$

$$V_{bx1} = V_{bs1} + V_{as2}$$

$$V_{cx1} = V_{cs1} + V_{bs2}$$

$$\vdots$$

$$\vdots$$

$$\vdots$$

$$V_{ax6} = V_{as11} + V_{cs12}$$

$$V_{bx6} = V_{bs11} + V_{as12}$$

$$V_{cx6} = V_{cs11} + V_{bs12}$$

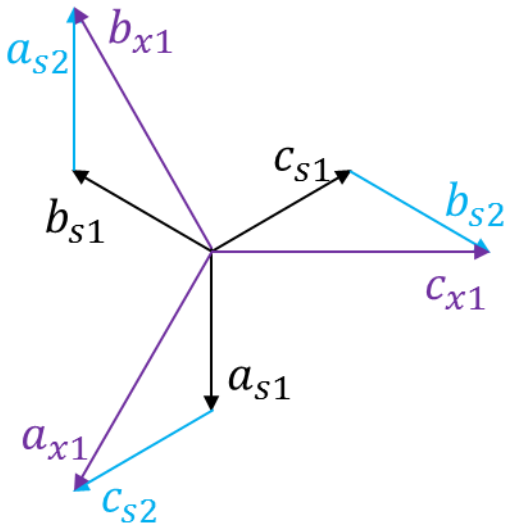

Figure 19: Zigzag winding connection

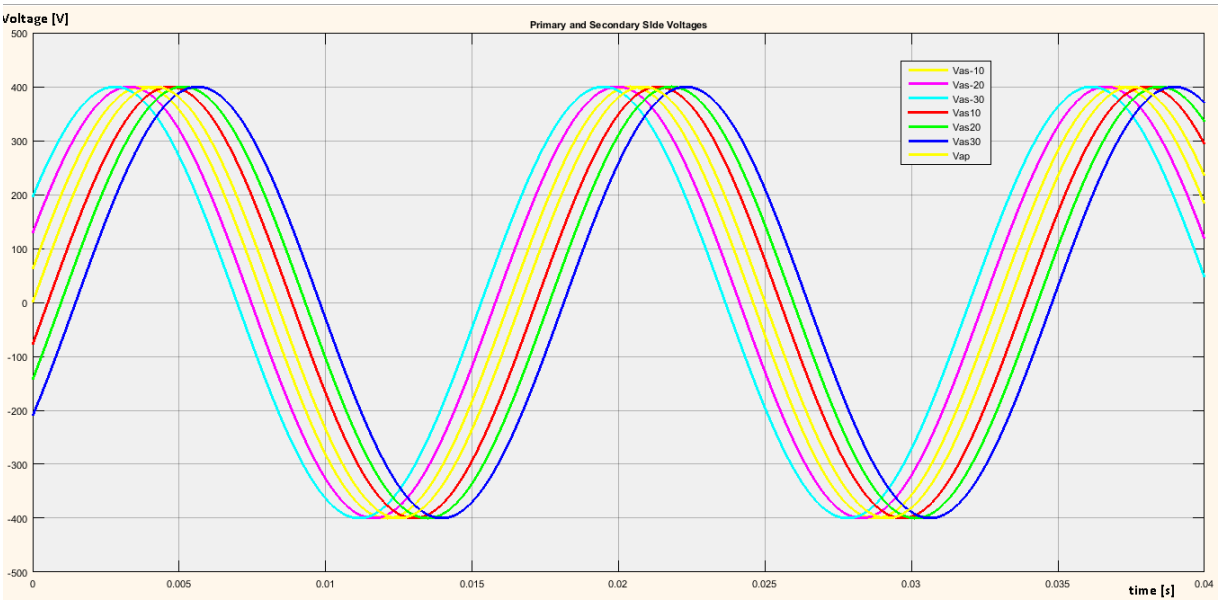

Figure 20: Secondary side voltages of the 18-phase phase-shifting transformer

3.5 Multilevel Inverter

Inverters are used to convert DC power to AC power of desired voltage and frequency. Controlling the switches of the inverter, any required AC voltage and frequency can be obtained at the output. Multilevel inverters are able to provide required AC voltage level using multiple DC sources as an input. In recent years, multilevel inverters have become more popular especially for motor drive systems due to their high power ratings, high efficiency and lower switching losses [10]. There are several multilevel inverter topologies but diode-clamped multilevel inverters, flying capacitor multilevel inverters and cascaded H-bridge multilevel inverters are most commonly used for motor drive applications.

3.5.1 Diode-Clamped Multilevel Inverters

Diode-clamped multilevel inverter is one of the well-known multilevel inverter topologies. The diodes are used as clamping devices to clamp the dc input voltage in order to produce AC voltage at the output [9, 10]. A three phase three-level diode clamped multilevel inverter is shown in Figure 21. D_{Z1} and D_{Z2} are clamping diodes and S_1, S_2, S_3 and S_4 are the active switches with the anti-parallel diodes D_1, D_2, D_3 and D_4. When S_2 and S_3 are on, output of phase A is connected to neutral point Z and the DC voltage across each capacitor is E which is normally equal to half of V_d.

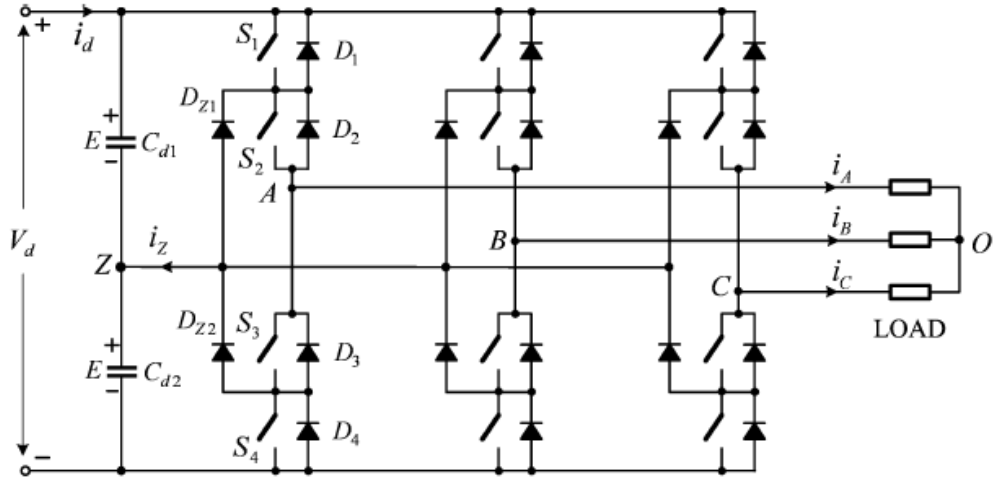

Figure 21: Three-level diode-clamped multilevel inverter adapted from [9]

Table 1 shows the switching states of the phase A. When switching states P and N define upper and lower two switches respectively, switching state O represents inner two switches. When both upper switches are on, output voltage v_{az} is +E and when lower two switches are on, output voltage v_{az} is –E. Output voltage is zero while inner two switches are on. The direction of load current i_A decides which clamping diodes will be on or off. For a positive load current, upper clamping diode D_{Z1} is on and for a negative load current, lower clamping diode D_{Z2} is on.

Table 1: Switching states adapted from [9]

Switching States	Device Switching Status for Phase A				Inverter terminal Voltage V_{AZ}
	S_1	S_2	S_3	S_4	
P	On	On	Off	Off	E
O	Off	On	On	Off	0
N	Off	Off	On	On	-E

Figure 22 shows an example of the switching states, gate signals and inverter output voltages of the three-level diode clamped multilevel inverter. V_{g1}, V_{g2}, V_{g3} and V_{g4} are gate signals for the switches. The gate signals can be generated by different modulation techniques such as carrier-based modulation. Terminal voltage V_{AZ} has three level as +E, 0 and –E. Terminal voltages of all three phases are balanced with a $2\pi/3$ phase shifting angle and line-to-line voltage has 5 voltage levels as shown in Figure23 [9].

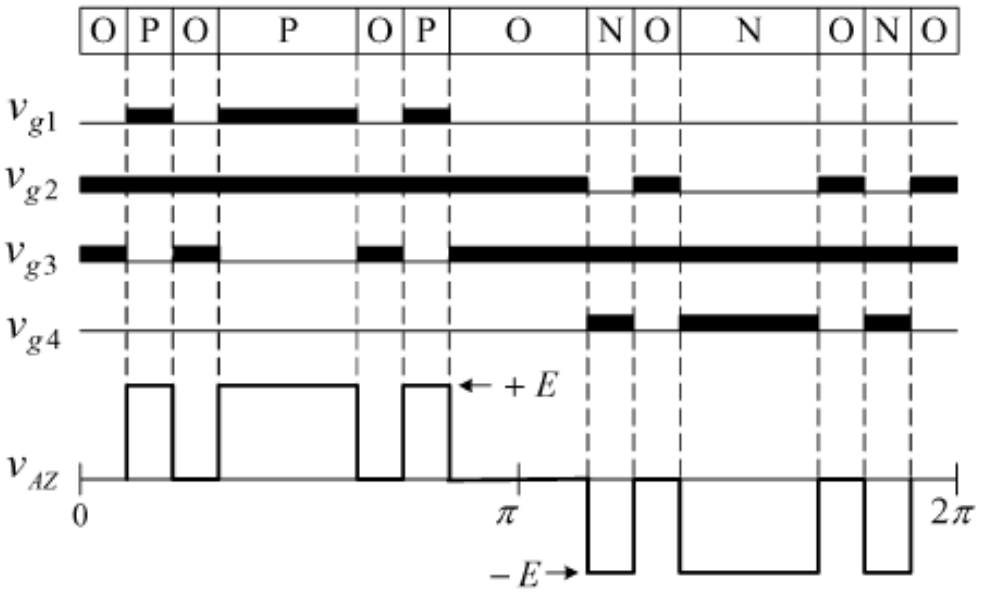

Figure 22: Terminal voltage, switching states and gate signals adapted from [9]

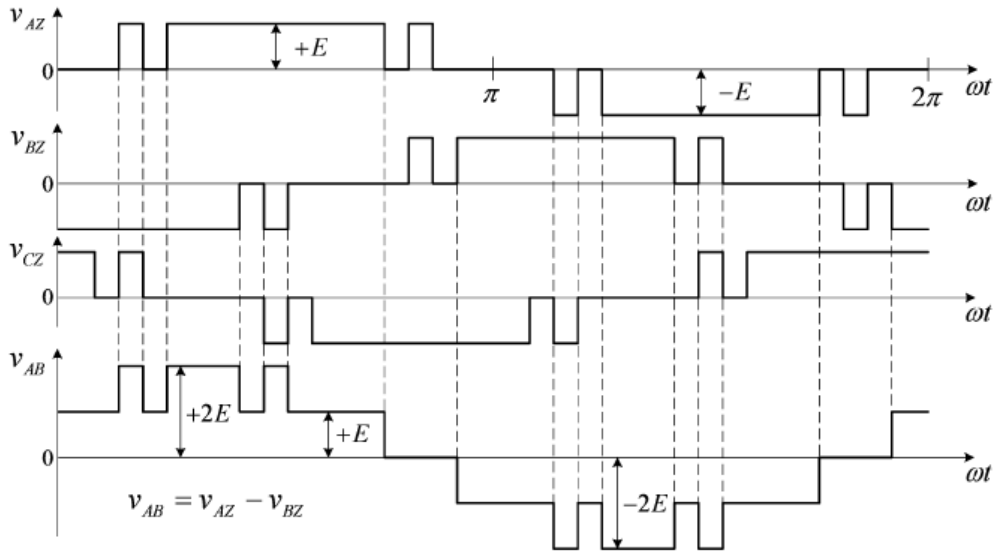

Figure 23: Inverter output voltages adapted from [9]

3.5.2 Flying-Capacitor Multilevel Inverters

Figure 24 shows a 5-level flying capacitor multilevel inverter. There are four pair of switches and eight switches in total for each leg. Each pair has individual gate signal. For instance, switches S_1, S_1' are one pair and one gate signal for both these two switches and 4 individual gate signals for switches in each leg [9].

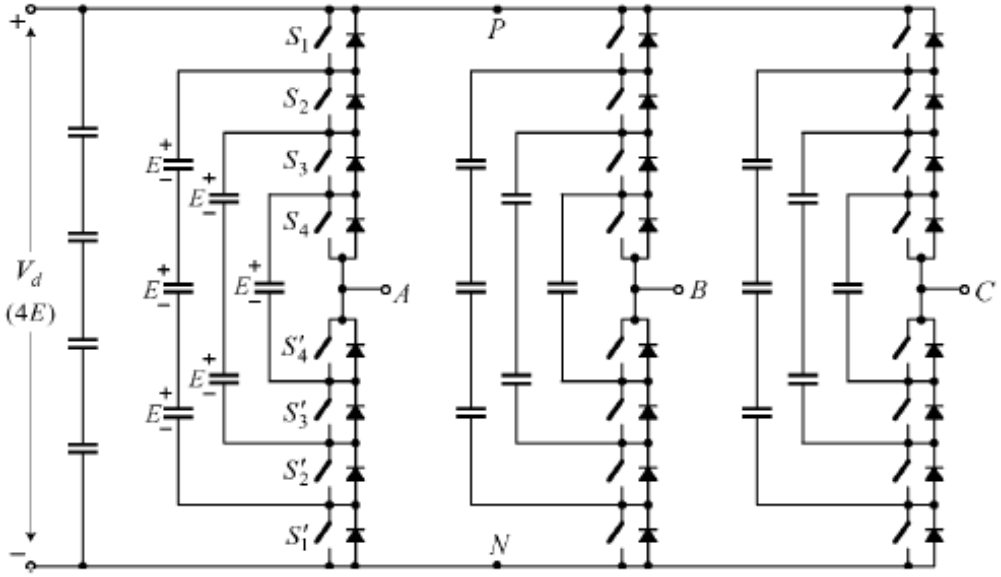

Figure 24: 5-level flying capacitor multilevel inverter adapted from [9]

The output voltage of the 5-level flying capacitor multilevel inverter has 5 voltage levels as shown in Figure 25. When the switches S_1, S_2, S_3 and S_4 are on, phase voltage V_{AN} is 4E. However, there are 4 sets of different switching states for voltage level of 3E and 1E and 6 sets of different switching states for voltage level of 2E as shown in Table 2. The switching frequency is set to 720 Hz for each switch therefore, the equivalent inverter switching frequency is 2880 Hz which is four times of the device switching frequency. Although flying-capacitor multilevel inverters lower the THD, there are some limitations of these type of multilevel configuration. They need several capacitors and their discharge units. Moreover, capacitor voltage balancing is also challenging. Therefore, flying-capacitor multilevel inverters are not commonly used for drive systems [9].

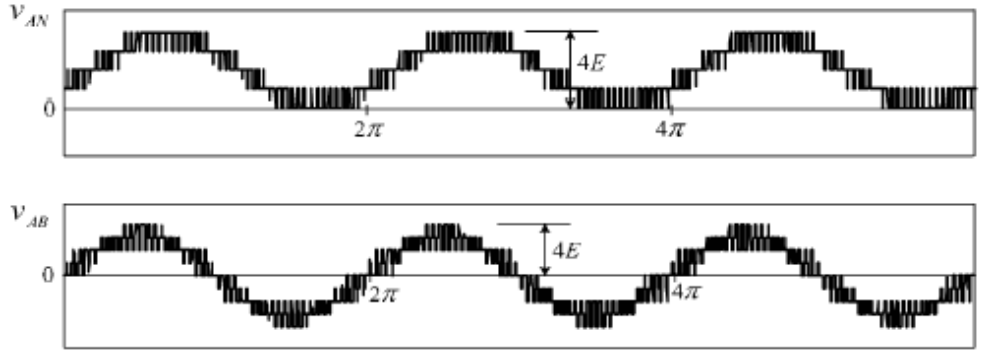

Figure 25: Voltage waveforms of the 5-level flying capacitor multilevel inverter [9]

Table 2: Switching states of 5-level flying capacitor multilevel inverter [9]

Inverter Phase Voltage V_{AN}	Switching State			
	S_1	S_2	S_3	S_4
4E	1	1	1	1
3E	1	1	1	0
	0	1	1	1
	1	0	1	1
	1	1	0	1
2E	1	1	0	0
	0	0	1	1
	1	0	0	1
	0	1	1	0
	1	0	1	0
	0	1	0	1
1E	1	0	0	0
	0	1	0	0
	0	0	1	0
	0	0	0	1
0	0	0	0	0

3.5.3 Cascaded H-Bridge Multilevel Inverters

Cascaded H-bridge multilevel inverters are one of the most popular multilevel inverter used for medium voltage motor drive systems [9, 11]. Figure 26 shows a single-phase H-bridge power cell of inverter. Multiple of these power cells are used in order to build cascaded H-bridge multilevel inverter. Each cell needs isolated DC supplies which are the outputs of the multipulse diode rectifiers explained in section 3.3. Each leg includes two IGBT switching devices.

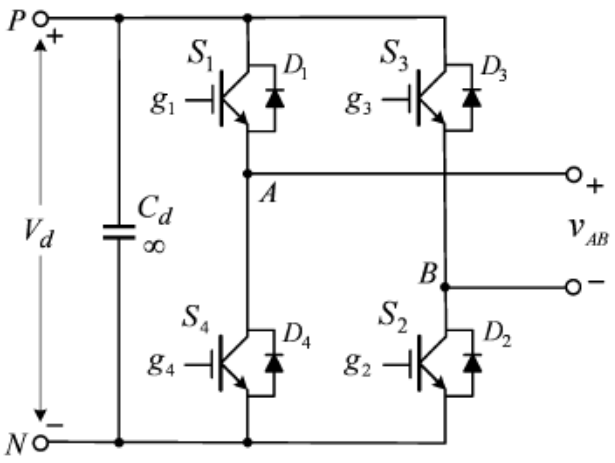

Figure 26: A single phase H-bridge cell adapted from [9]

Unipolar pulse-width modulation (PWM) is usually used for gate signals. Two modulating sinusoidal signals are compared with the triangular carrier v_r in order to generate two gate signals for the upper switches S_1 and S_3 as shown in Figure 27.

Modulating sinusoidal signals have same magnitude and amplitude but 180° out of phase. For the example, switching frequency is 900 Hz. Dominant harmonic orders are $2m_f \pm 1$ *and* $2m_f \pm 3$ *at the* output voltage of the inverter which means that dominant harmonics are neighbor to 1800 Hz as shown in Figure 28.

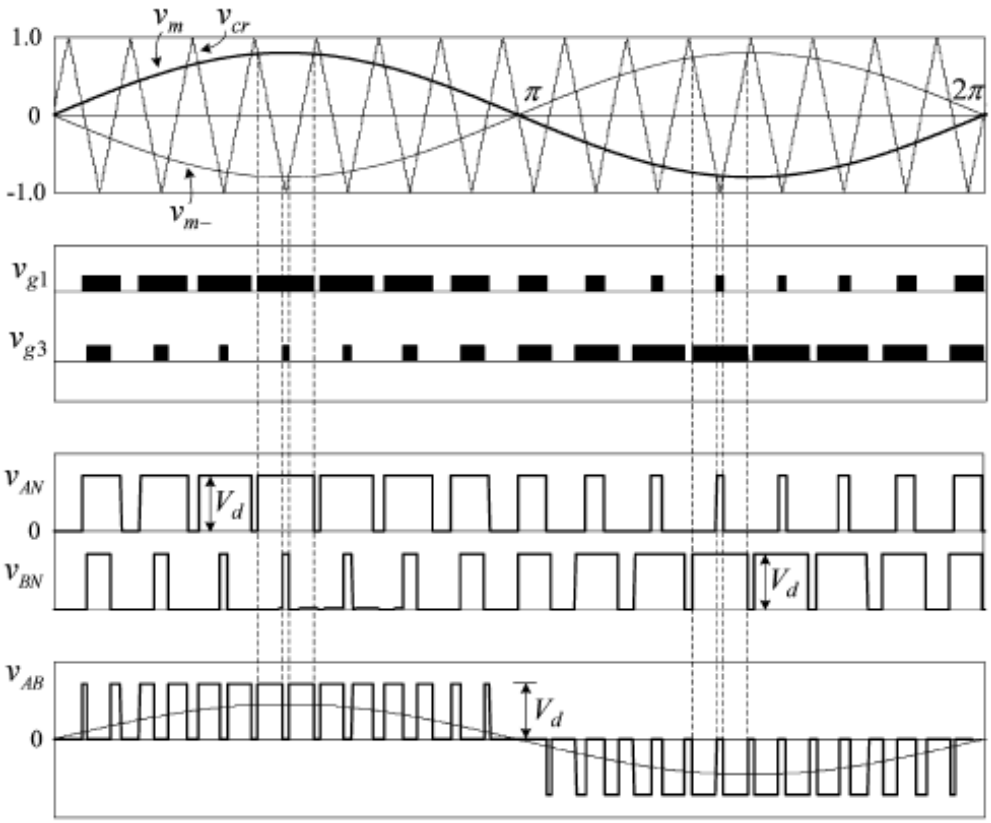

Figure 27: PWM waveforms adapted from [9]

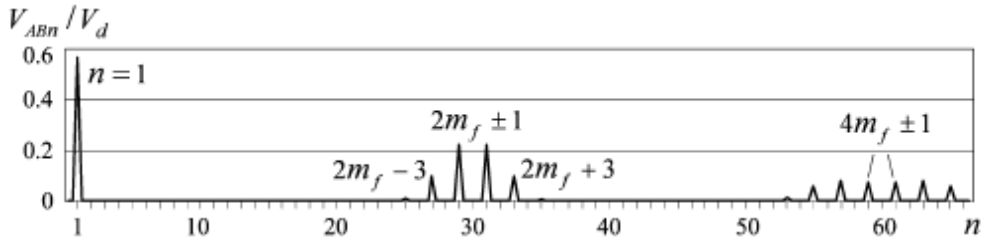

Figure 28: Harmonic spectrum adapted from [9]

Figure 29 shows an example of three-phase five-level cascaded H-bridge multilevel inverter. The level of the inverter can be calculated

$$m = 2H + 1$$

where m is the level number and H is the number of H-bridge cells for one phase. Phase shifting between the H-bridge cells can be calculated

$$\delta = 360°/(m - 1)$$

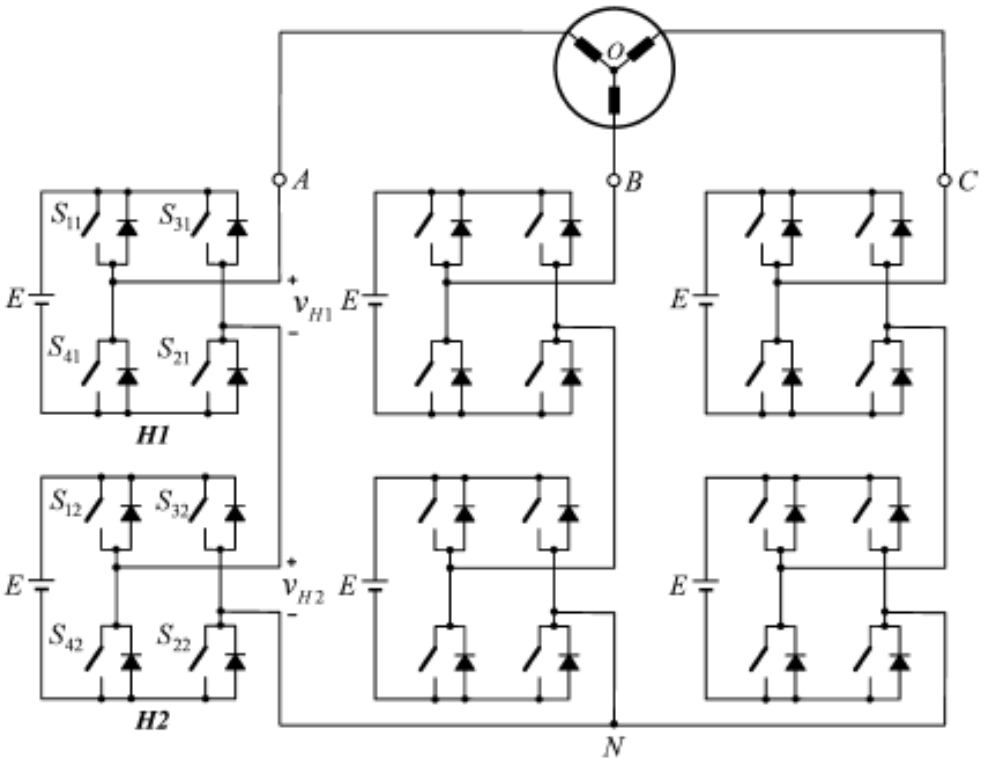

Figure 29: An example of a five-level H-bridge cascaded multilevel inverter adapted from [9]

3.5.4 Comparing Multilevel Inverter Topologies

All these multilevel inverter topologies have some advantages and disadvantages. For the same input voltage, double inverter output voltage can be obtained from cascaded H-bridge multilevel inverter as compared to other two topologies. Moreover, cascaded H-bridge multilevel inverters do not include any flying capacitors and clamping diodes which lower the size and cost.

Cascaded H-bridge multilevel inverter topology has the advantage of weight and cost as compared to the other two multilevel inverter topologies. Figure 30 shows the weight comparison of the 5-level multilevel topologies and Figure 31 shows the cost comparison as well [12].

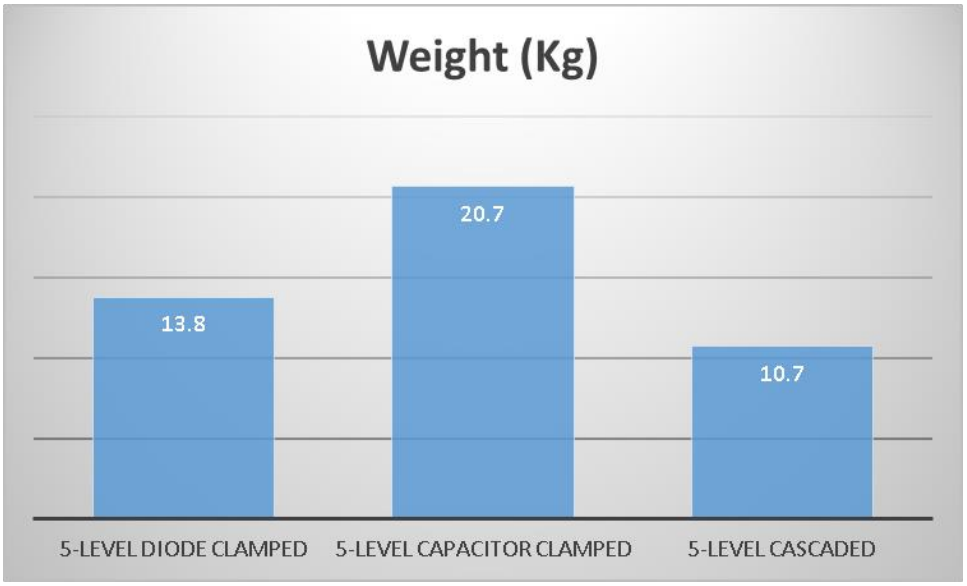

Figure 30: Weight comparison between multilevel inverter topologies

Figure 31: Cost comparison between multilevel inverter topologies

3.6 Subsea Umbilical Cable

Subsea umbilical cables are widely used for off-shore oil platforms. Traditional transmission lines longer than 250 km are known as long lines. Although, subsea cables can be up to 80 km long, they are called as long cables. Long cable can be modeled with several π-sections as shown in Figure 32. Shunt capacitors can be ignored for low frequencies. However, they should not be ignored for drive systems because of their high switching frequencies [8].

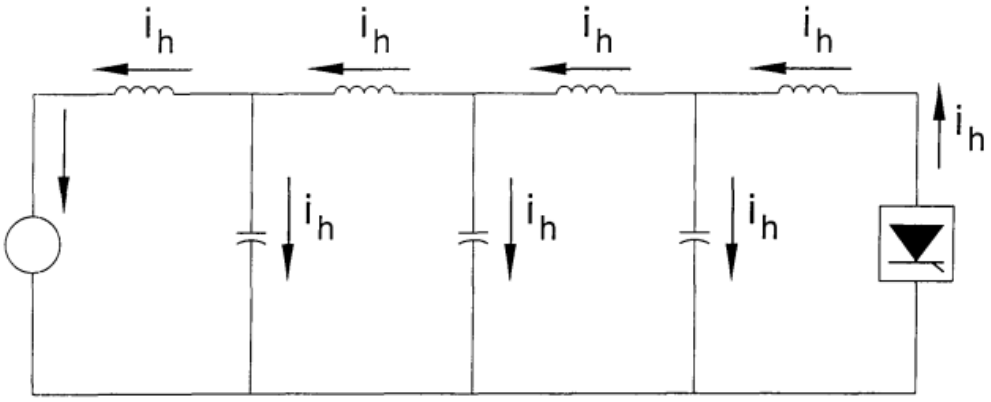

Figure 32: Long line equivalent circuit adapted from [8]

3.6.1 Modeling the Cable

Transmission lines are analyzed by lumped parameters in order to approximate the real line systems. The line can be modelled by T-sections or π-sections [13]. In this study, π-section model has been used for all simulations and all analysis has been done using ANSYS Simplorer and MATLAB Simulink.

$$2N^2 \gg |jB * (R + jX)|$$

where,

R: total resistance,

X: total inductive reactance,

B: total susceptance

N: number of the π-sections

In figure 33, curve has been obtained from the equation above and curve b is for adequate representation [13]. 10 π-sections have been applied for a 5 km cable for simulation.

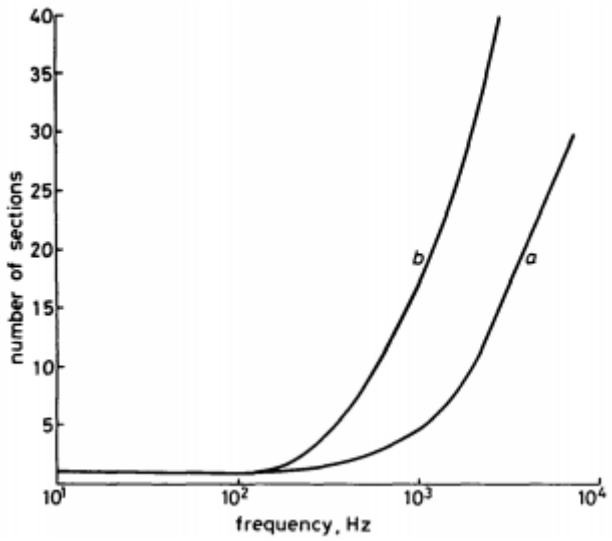

Figure 33: Number of π-sections adapted from [13]

In this study, General Cable Exzhellent XXI has been chosen as shown in Figure 34. This cable can supply three different three-phase systems but only one three-phase has been used for the simulations. Figure 35 shows the cross-section of the coaxial cable in order to calculate the inductance parameters.

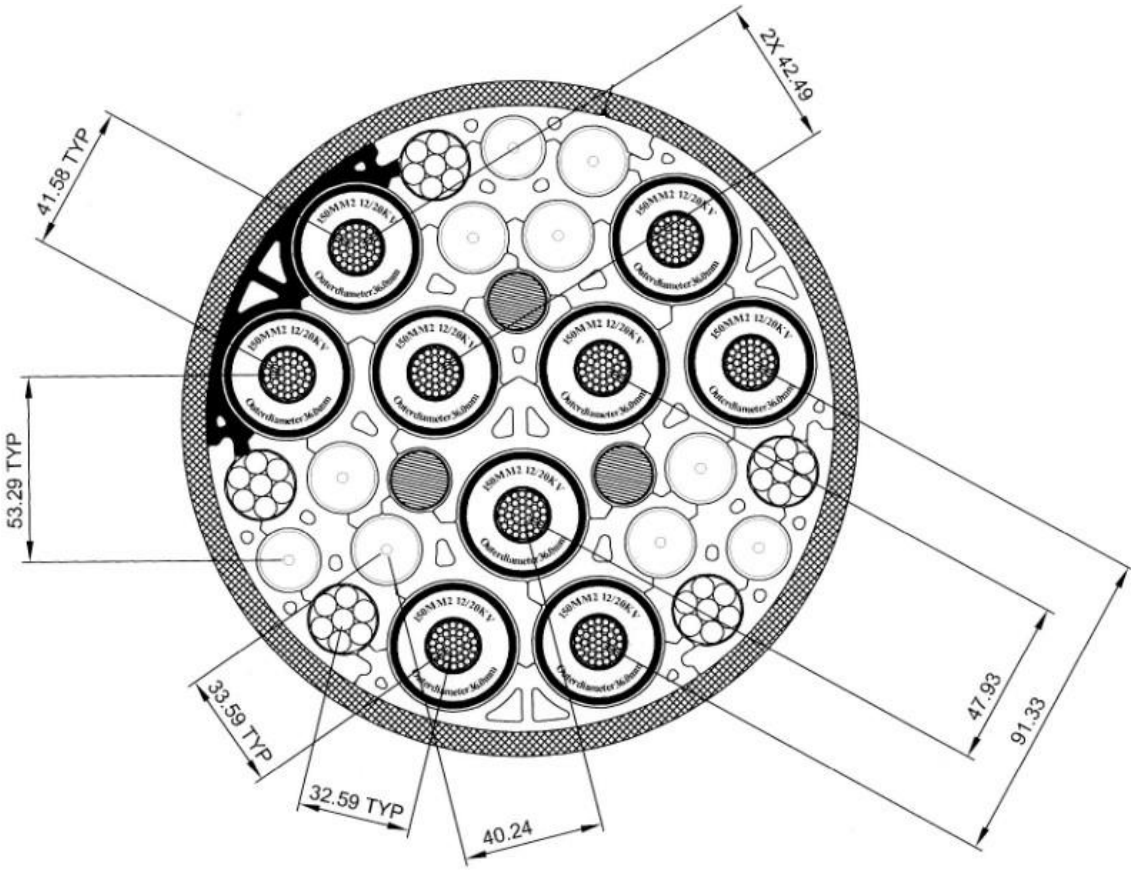

Figure 34: Umbilical subsea cable adapted from [14]

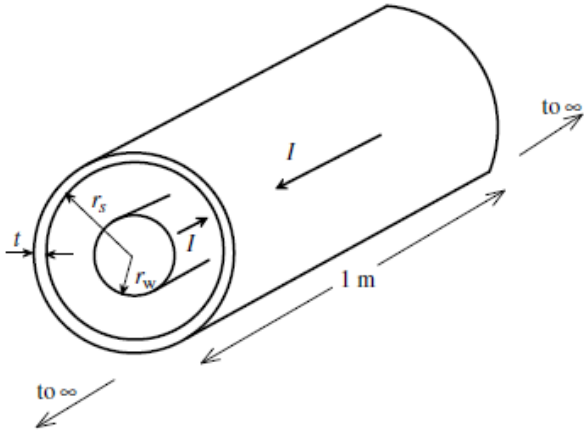

Figure 35: Cross-section of a coaxial cable adapted from [14]

Internal inductance of the cable can be calculated as

$$L_{internal} = \frac{\mu_0}{8\pi}\ H/m$$

External inductance of the cable can be calculated as

$$L_{external} = \frac{\mu_0}{2\pi} ln \frac{r_s}{r_w} [H/m]$$

where,

K= 1
S= distance between conductor of cable axes
r_w: wire radius

Mutual inductance can be calculated as

$$L_{mutual} = \frac{\mu_0}{2\pi} ln \frac{(KxS)}{r_w} [mH/km]$$

3.6.2 Skin Effect

Alternating current tends to flow on the skin of the cable. Due to the higher frequency harmonics caused by VFDs, skin effect should be accounted for the cable model for drive systems. For the modeling of skin effect, ladder branch method has been used as shown in Figure 36 and an example of MATLAB Simulink model of the cable is given in Figure 37. x is found as $\sqrt{10}$ and additional branches can be added for each decade of the frequency which can be calculated as in Table 3 [15].

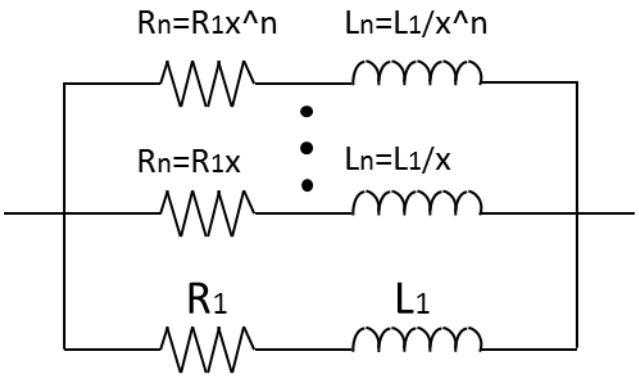

Figure 36: R-L Ladder adapted from [15]

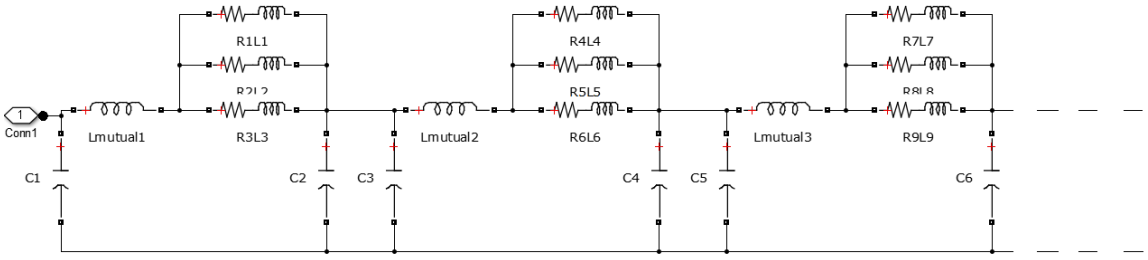

Figure 37: A part of the umbilical cable modeled in MATLAB Simulink

Table 3: Skin effect R and L factors adapted from [15]

# of Branches	R_1	L_1
1	R_{DC}	L_{int}
2	1.32 R_{DC}	1.68 L_{int}
3	1.42 R_{DC}	1.94 L_{int}
4	1.45 R_{DC}	2.03 L_{int}
5	1.457 R_{DC}	2.06 L_{int}
6	1.461 R_{DC}	2.07 L_{int}

3.6.3 Calculating Cable Parameters for Each π-Sections

Cable parameters have been calculated for each π-sections for a 5 km cable from Table 4 [14].

Table 4: Cable parameters

R_{DC}	0.124 Ω/km
L_{int}	50 μH/km
L_{mut}	316 μH/km
C	0.252 μF/km

$$R_{DC-\pi} = \frac{rxL}{10} = 0.062\ \Omega/\pi - section$$

$$L_\pi = \frac{(l_{internal} + l_{mutual})xL}{10} = (25 + 158)\ \mu H/\pi - section$$

$$C_\pi = \frac{cxL}{10} = 0.126\ \mu F/\pi - section$$

For the ladder model, 3 branches have been calculated

$$R_1 = 1.42 \times R_{DC} = 0.08804\ \Omega$$

$$R_2 = R_1 \times x = 0.27841\ \Omega$$

$$R_3 = R_1 \times x^2 = 0.8804\ \Omega$$

$$L_1 = 1.94 \times L_{int} = 48.5\ \mu H$$

$$L_2 = L_1/x = 15.337\ \mu H$$

$$L_3 = L_1/x^2 = 4.85\ \mu H$$

Shunt capacitors have been calculated as

$$C_1 = C_2 = \frac{C_\pi}{2} = 0.063\ \mu F$$

3.7 Induction Motor

Induction motors are commonly used in oil pumping systems due to its advantages. There are the some advantages of induction motors;

- low cost
- simple and almost unbreakable
- less maintenance required
- higher power factor
- high efficiency

Induction motors are connected to electrical submersible pumps (ESP) for oil production in offshore as shown in Figure 38. They can be driven by VFDs as explained in previous sections. Due to producing high harmonic distortion of the VFDs, there are some issues occur in induction motors such as more copper and core losses, motor starting issues and voltage ripple. In this study, only core losses have been analyzed and other issues have left as a future work. These induction motors designed for FPSOs are generally large machines and can be up to 40 MW. However, simulation results have been obtained on a smaller scale induction motor which will be described in following sections.

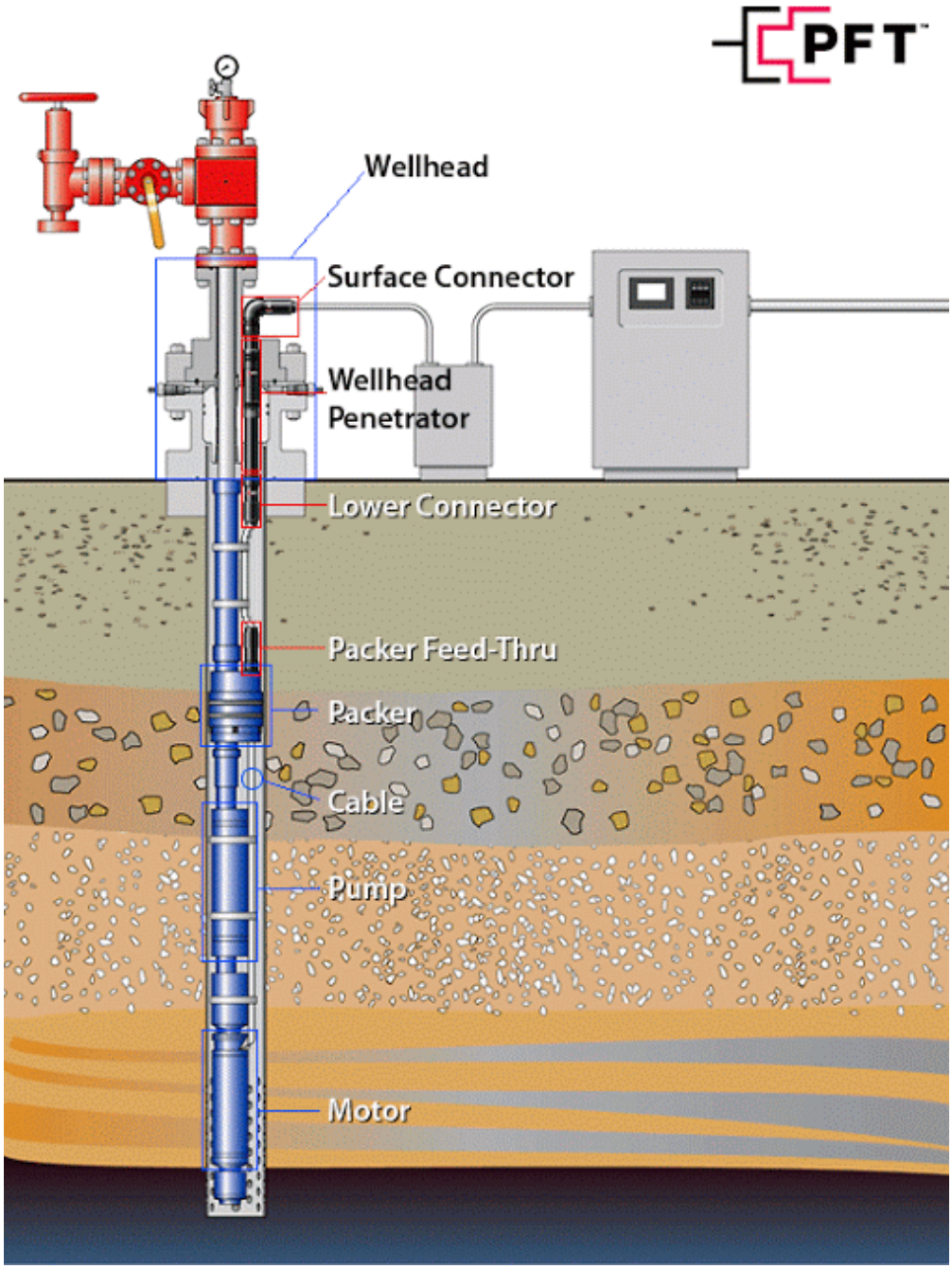

Figure 38: Electrical Submersible Pump adapted from PFT [16]

4. HARMONIC ANALYSIS

Due to DC link in the middle of the rectifier and the inverter, harmonic analysis can be presented as utility side harmonics caused by the multipulse rectifier and motor side harmonics caused by multilevel inverter.

4.1 Multipulse Diode Rectifier Harmonics

Six-pulse diode rectifier causes high order current harmonics on the utility side. Due to the limitation of current harmonic distortion by IEEE Standard 519-1992, rectifier pulse number is increased in order to keep harmonic distortion in the limits. The DC link is connected to a resistive load for all following diode rectifier simulations and multipulse diode rectifiers are series connected. Secondary side windings are zigzag connected to have desired phase shifting for all rectifier pulse levels.

Figure 39 shows a six pulse diode rectifier which is connected to a synchronous generator through a delta/wye connected transformer and Figure 40 shows the primary side current waveform. 3^{rd} harmonic cancelled by the transformer thus; 5^{th} and 7^{th} harmonics are the dominant harmonics as shown in Figure 41. While 22% THD occurs on the primary side windings, 29% THD occurs on the secondary side windings.

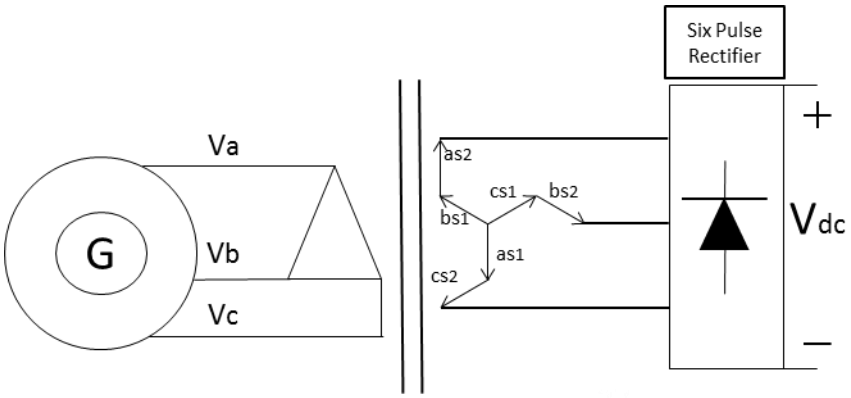

Figure 39: Six pulse rectifier is connected to a generator

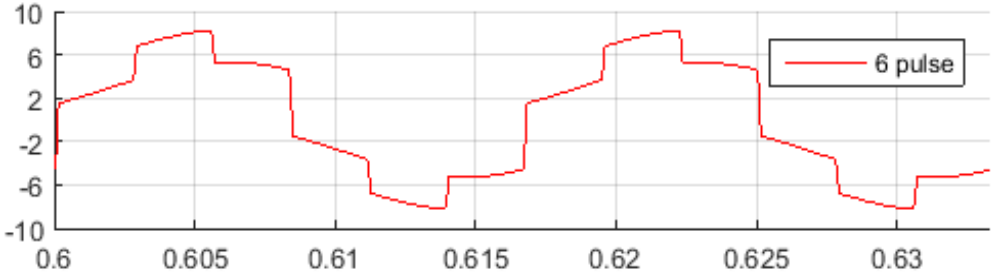

Figure 40: Primary side current waveform of the six pulse rectifier

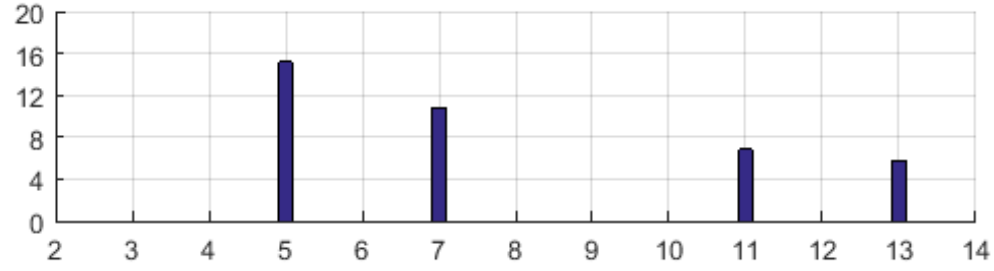

Figure 41: Current harmonic order of the six pulse rectifier

Two six-pulse diode rectifiers are connected to series to see the effect of the 12-pulse diode rectifier on the primary side windings of the phase shifting transformer as shown in Figure 42. Phase shifting angle $\delta = {}^{60}/_{2} = 30°$ between the secondary side windings. Figure 43 shows the primary side current waveform. 11^{th} and 13^{th} are the dominant harmonics while cancelling low order harmonics with the phase displacement in the transformer as shown in Figure 44, and THD is about 12%.

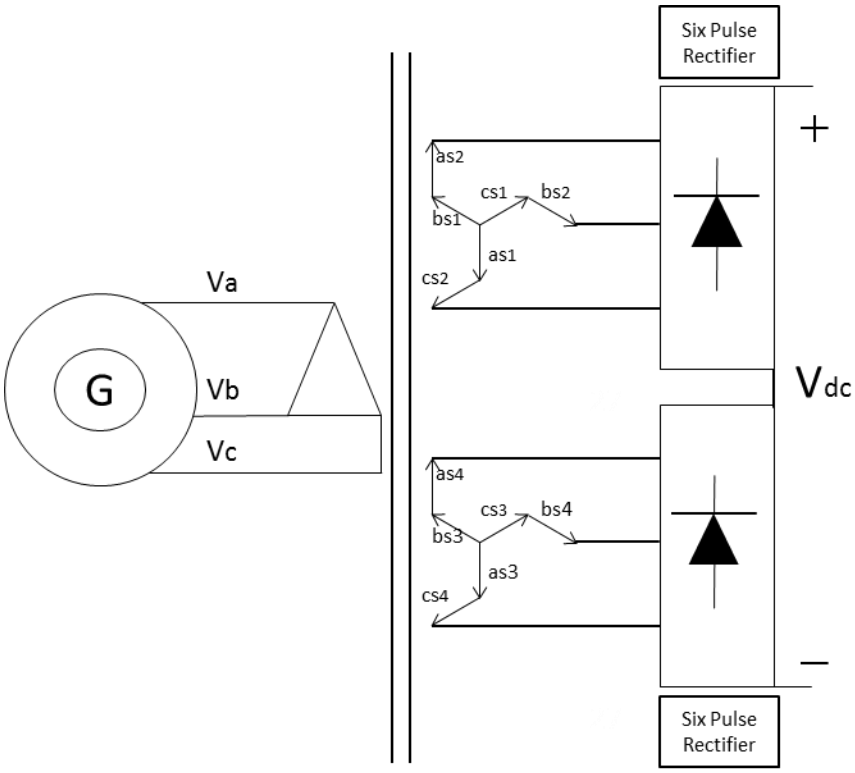

Figure 42: Twelve pulse rectifier is connected to a generator

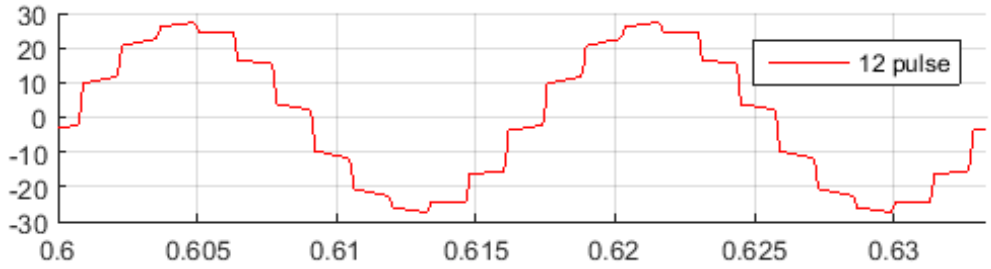

Figure 43: Primary side current waveform of the twelve pulse rectifier

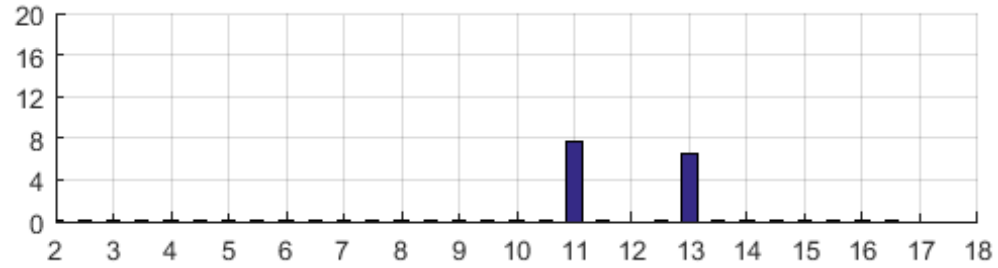

Figure 44: Current harmonic order of the twelve pulse rectifier

18-pulse diode rectifier is built by 3 series connected diode rectifiers as shown in Figure 45. Required phase shifting angle $\delta = {}^{60}/_{3} = 20°$ between the zig-zag connected secondary side windings of the phase shifting transformer. Primary side current waveform is illustrated in Figure 46. 17^{th} and 19^{th} harmonics are the dominant harmonics for the 18-pulse diode rectifier as shown in Figure 47, and THD occurs about 7% in the primary side windings of the phase shifting transformer.

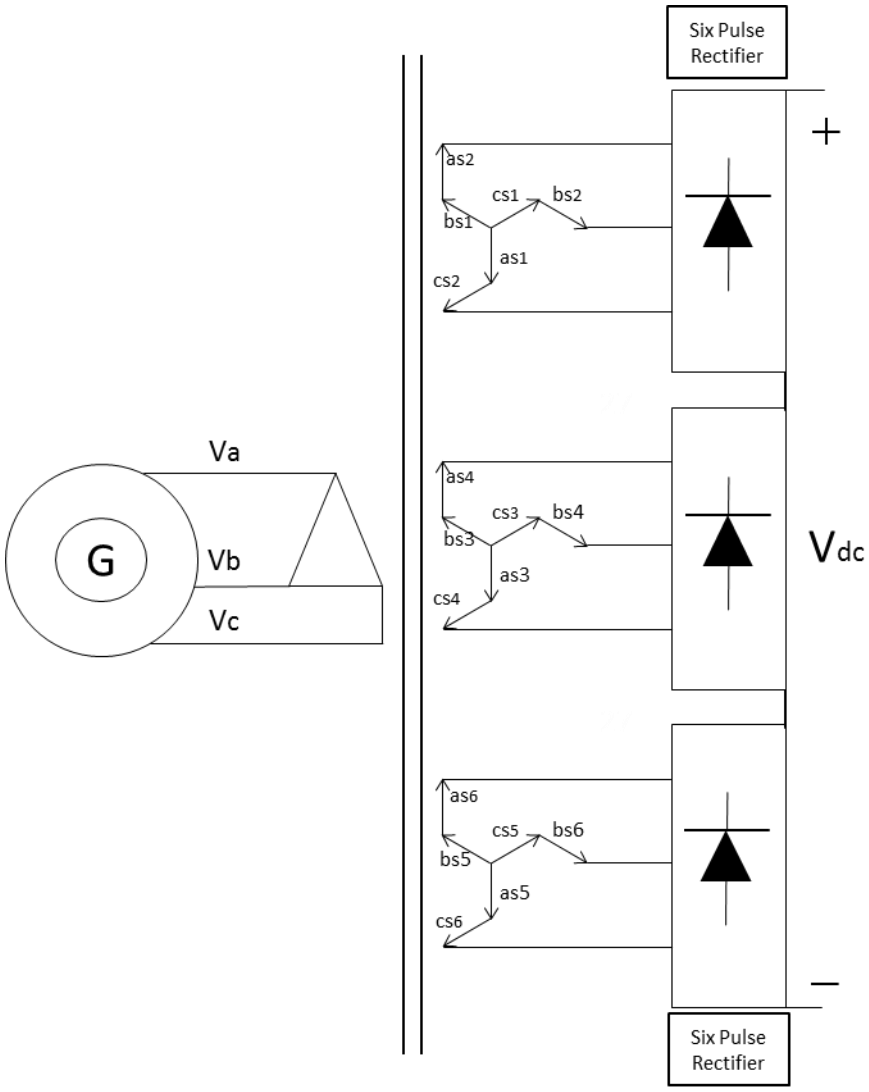

Figure 45: Eighteen pulse rectifier is connected to a generator

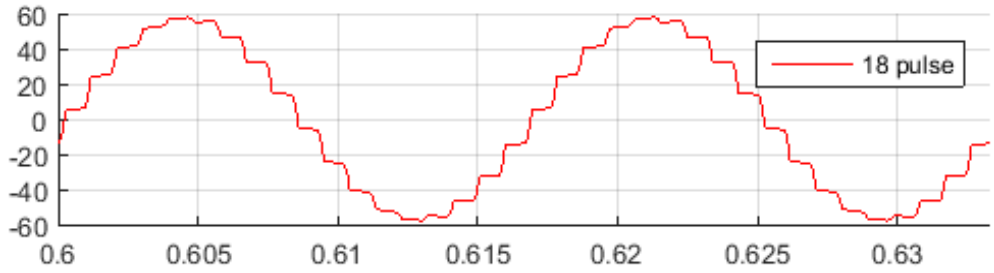

Figure 46: Primary side current waveform of the eighteen pulse rectifier

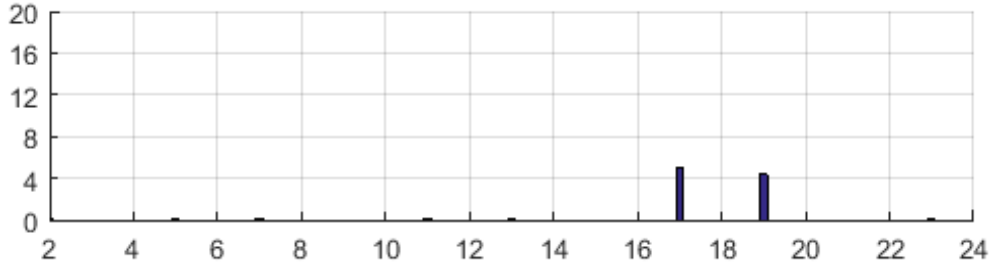

Figure 47: Current harmonic order of the eighteen pulse rectifier

4 six-pulse diode rectifiers are series connected for 24-pulse rectifier as shown in Figure 48. Required phase shifting angle $\delta = {}^{60}/_{4} = 15°$ between the secondary side windings of the phase-shifting transformer. Figure 49 shows the primary side current waveform of the phase-shifting transformer and THD is about 5%. 23rd and 25th are the dominant harmonics for the 24-pulse rectifier as shown in Figure 50.

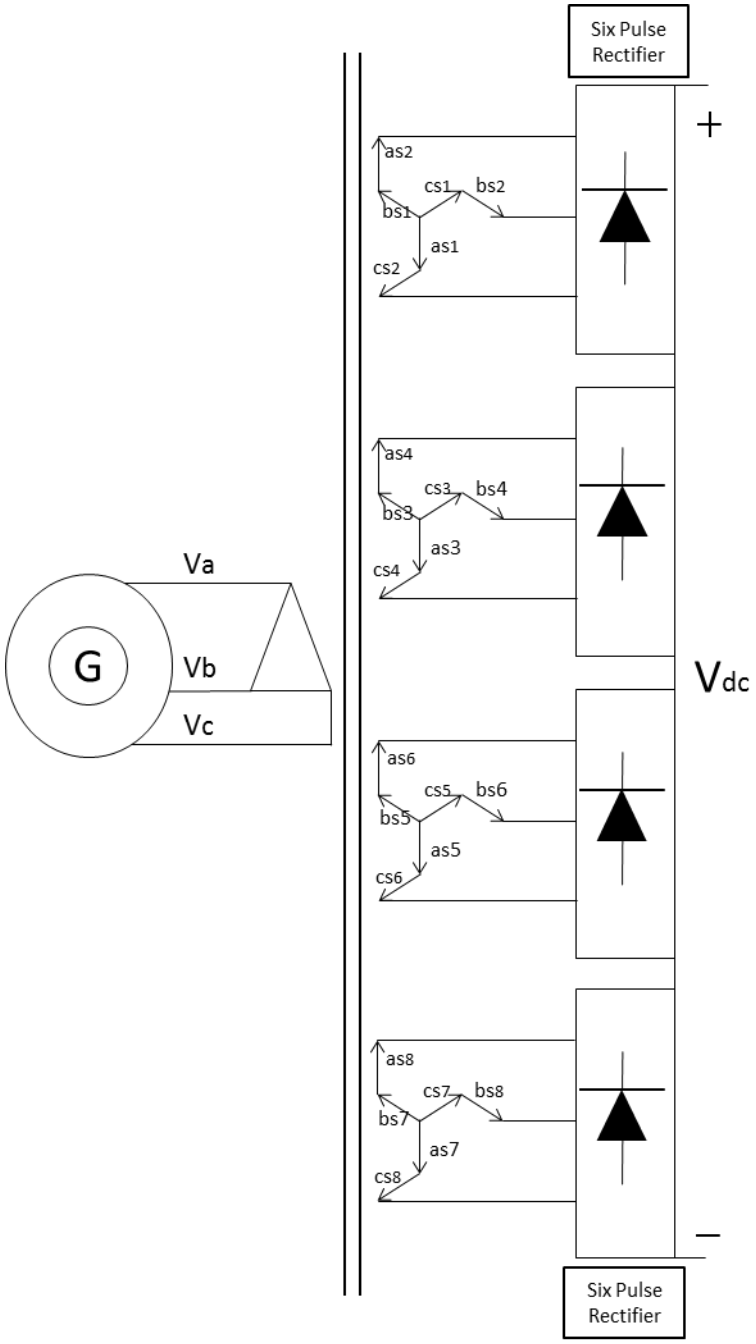

Figure 48: Twenty-four pulse rectifier is connected to a generator

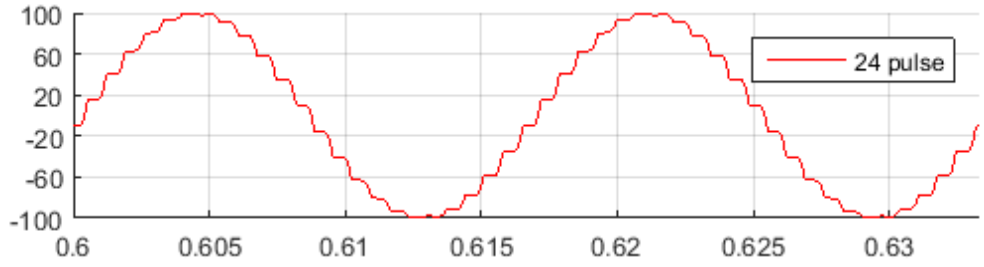

Figure 49: Primary side current waveform of the twenty-four pulse rectifier

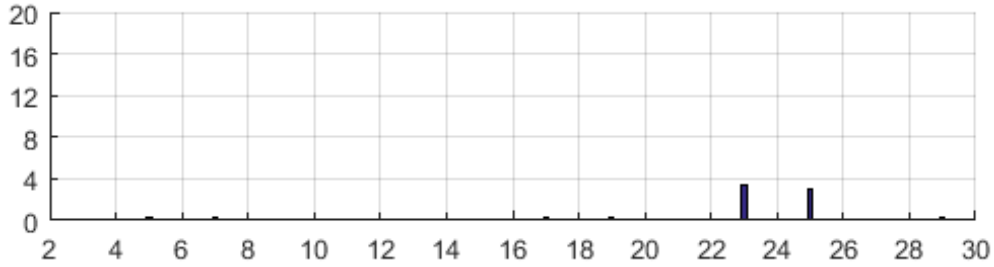

Figure 50: Current harmonic order of the twenty-four pulse rectifier

30-pulse diode rectifier consists of 5 series connected six-pulse diode rectifiers as shown in Figure 51. Phase shifting angle $\delta = {}^{60}/_{5} = 12°$ between secondary side windings of the phase-shifting transformer. The primary side current waveform is shown in Figure 52 and THD is about 3%. 29^{th} and 31^{st} are the dominant harmonics for the 30-pulse rectifier as shown in Figure 53.

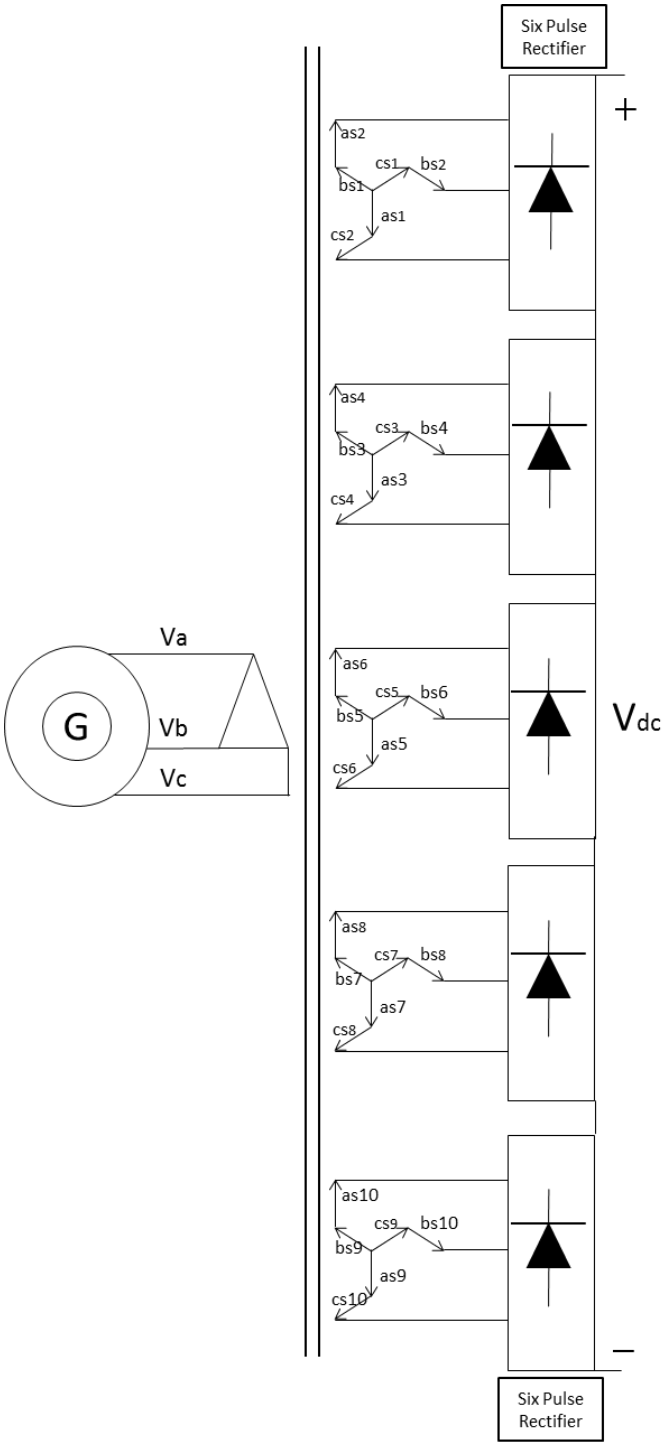

Figure 51: Thirty pulse rectifier is connected to a generator

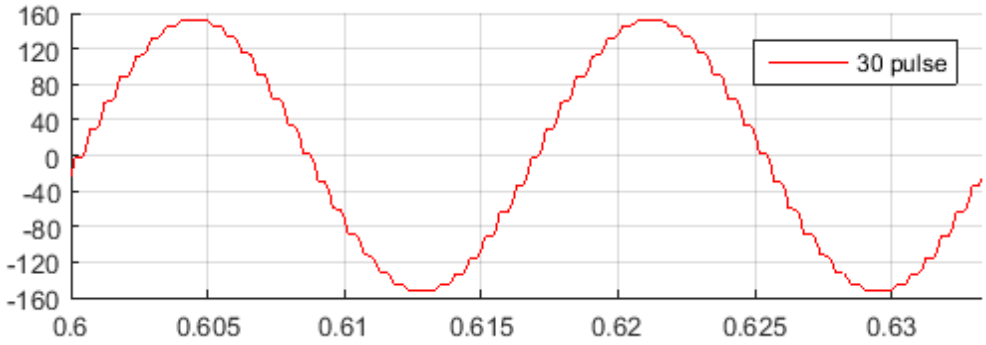

Figure 52: Primary side current waveform of the thirty pulse rectifier

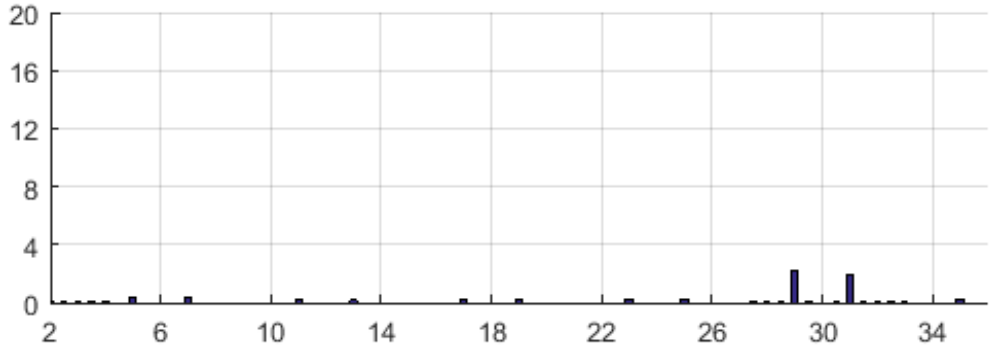

Figure 53: Current harmonic order of the thirty pulse rectifier

6 six-pulse diode rectifiers are series connected for 36-pulse rectifier as shown in Figure 54. Desired phase shifting angle $\delta = {}^{60}/_{6} = 10°$ between the secondary side windings of the transformer. The primary side current waveform is closer to sine wave as shown in Figure 55 and THD is about 2% which is within the limits. 35^{th} and 37^{th} are the dominant harmonics for the 36-pulse rectifier as shown in Figure 56.

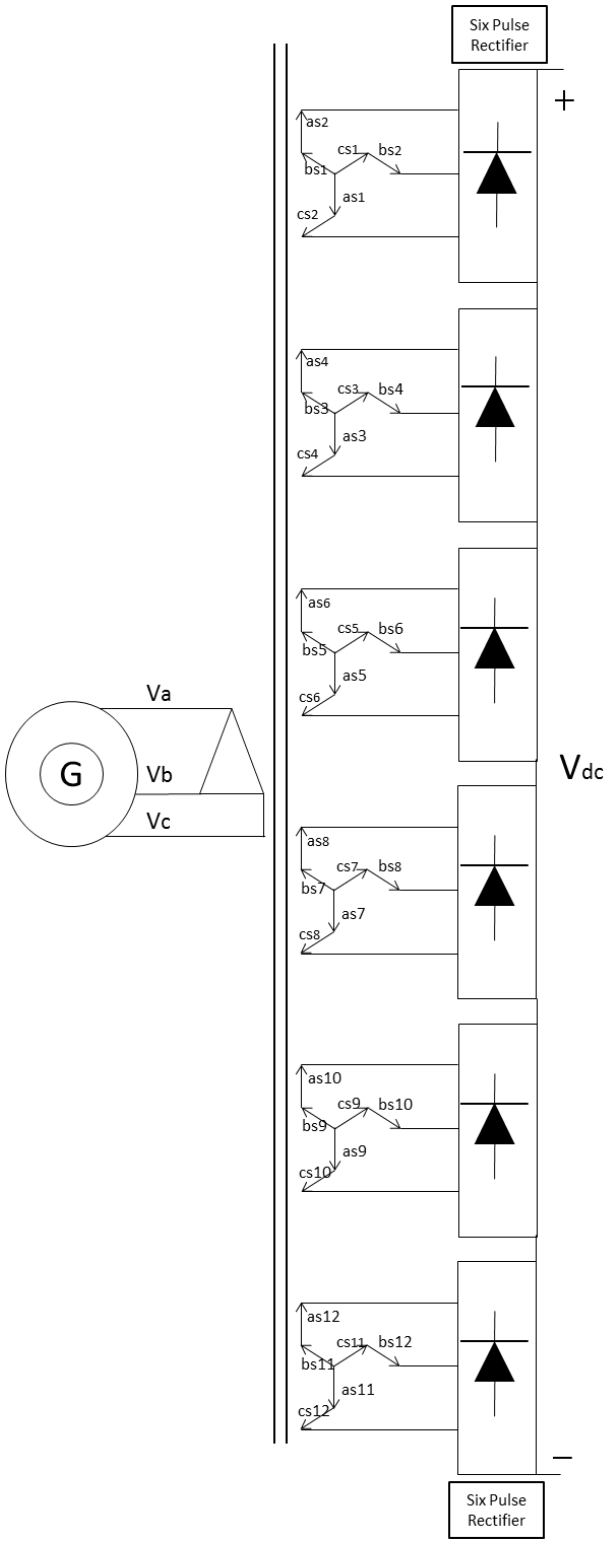

Figure 54: Thirty-six pulse rectifier is connected to a generator

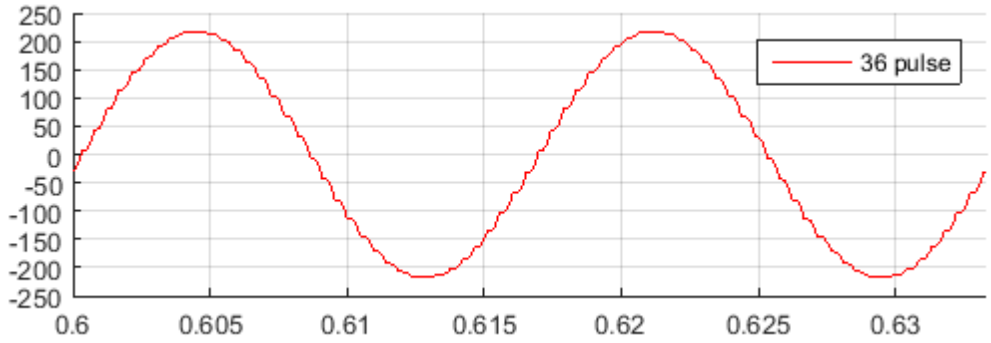

Figure 55: Primary side current waveform of the thirty-six pulse rectifier

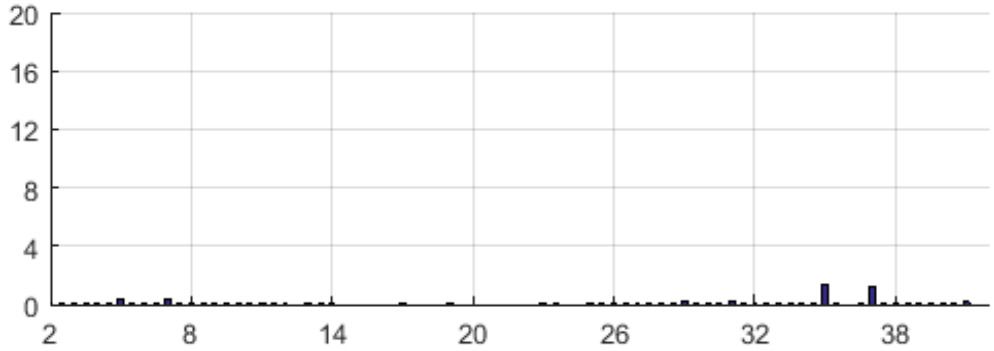

Figure 56: Current harmonic order of the thirty-six pulse rectifier

It is possible to achieve almost sine primary side current waveform with the 48-pulse rectifier and 72-pulse rectifier as shown in Figure 57 and Figure 58 respectively. Although the rectifier pulse number can be increased more to achieve less THD, it is costly and unnecessary. The phase-shifting transformer size will also be much larger for more pulses. Figure 59 shows the reducing THD graph up to 72-pulse diode rectifier. 36-pulse rectifier provides THD in the limits of the harmonic distortion standards, thus the system should be designed with the 36-pulse rectifier.

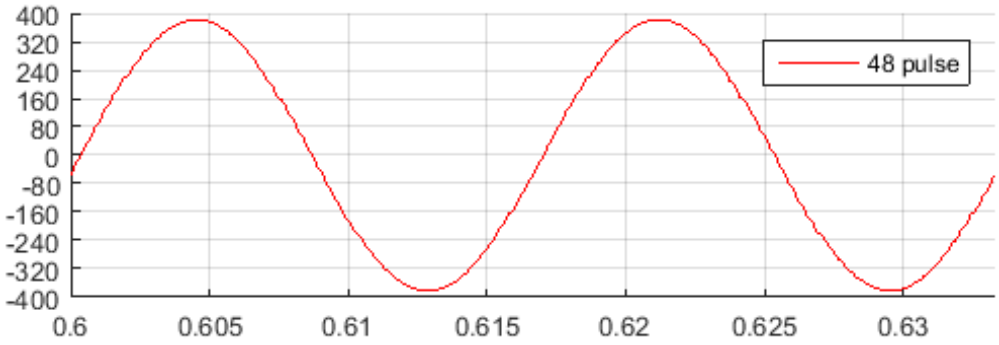

Figure 57: Primary side current waveform of the forty-eight pulse rectifier

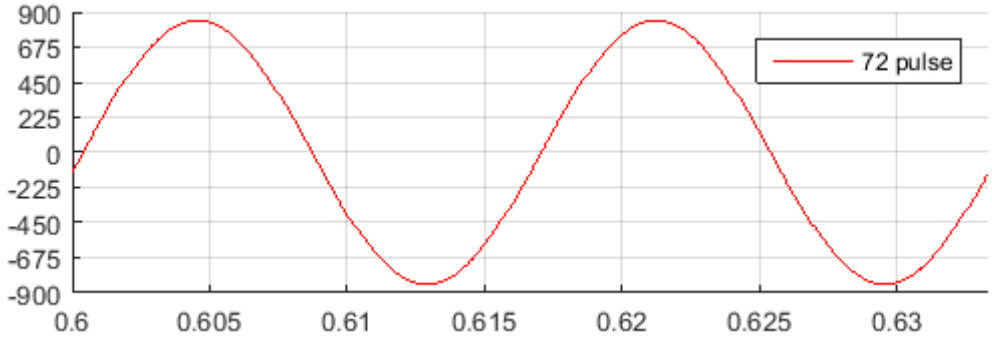

Figure 58: Primary side current waveform of the seventy-two pulse rectifier

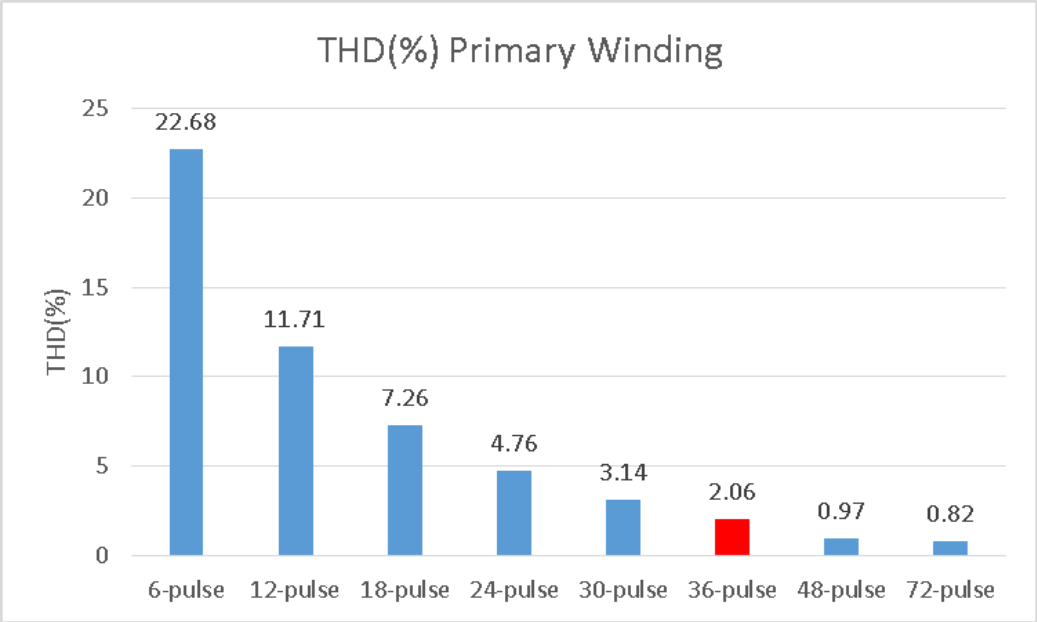

Figure 59: THD occurring in the secondary side windings

Table 5: Total harmonic distortion for the primary side and the secondary side windings

Pulse number	THD(%) Primary Winding	THD(%) Secondary Winding
6	22.68	29.81
12	11.71	29.41
18	7.26	29.08
24	4.76	28.83
30	3.14	28.61
36	2.06	28.27
48	0.97	27.95
72	0.82	27.28

4.2 Multilevel Inverter

In this section, output voltage harmonics of the cascaded H-bridge inverter harmonic results are simulated from 3-level to 17 level. 100 Volt DC supply is used for each H-bridge inverter cell. Each cell consists of 4 IGBTs and proposed PWM method is used for switching them. Triangular carrier frequency is 900 Hz for all simulation results.

3-level H-bridge multilevel inverter cell is supplied with a 100 V DC voltage source shown in Figure 60 and output voltage of the cell V_{AC} as shown in Figure 61. THD of the V_{AC} is around 76%.

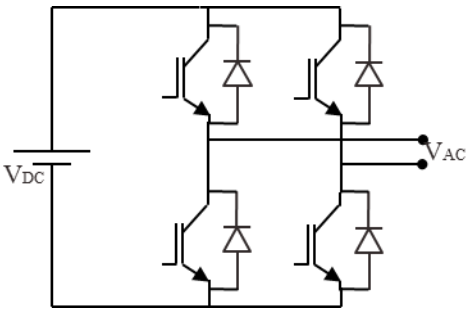

Figure 60: 3-level H-bridge multilevel inverter

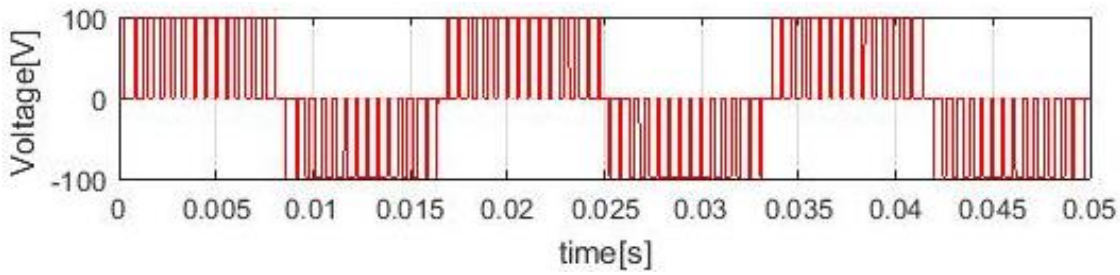

Figure 61: 3-level output voltage waveform

5-level cascaded H-bridge multilevel inverter cells are connected to 100 V DC voltage sources as shown in Figure 62. Output AC peak voltage is 200 V as shown in Figure 63 and THD is measured 38%.

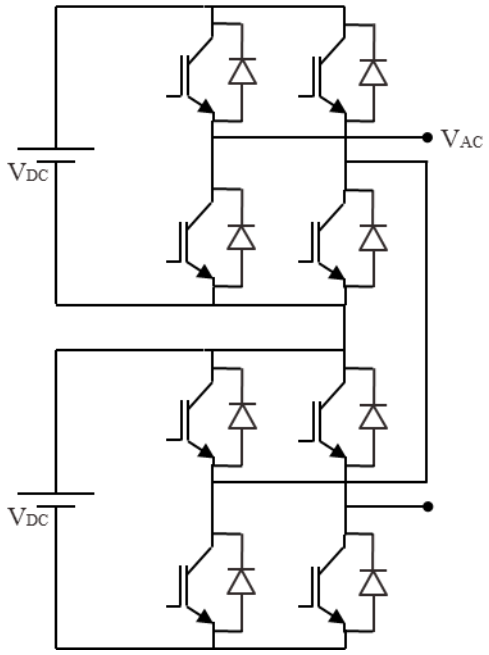

Figure 62: 5-level H-bridge multilevel inverter

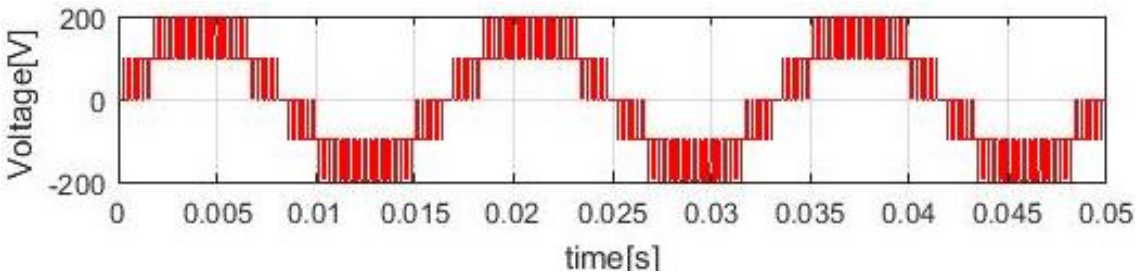

Figure 63: 5-level output voltage waveform

7-level cascaded H-bridge multilevel inverter cells are connected to the DC voltage sources as shown in Figure 64. Output AC peak voltage is 300 V as shown in Figure 65 and THD is measured 38%.

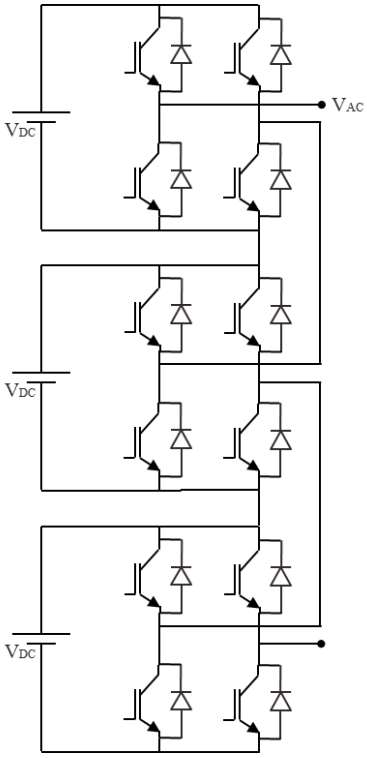

Figure 64: 7-level H-bridge multilevel inverter

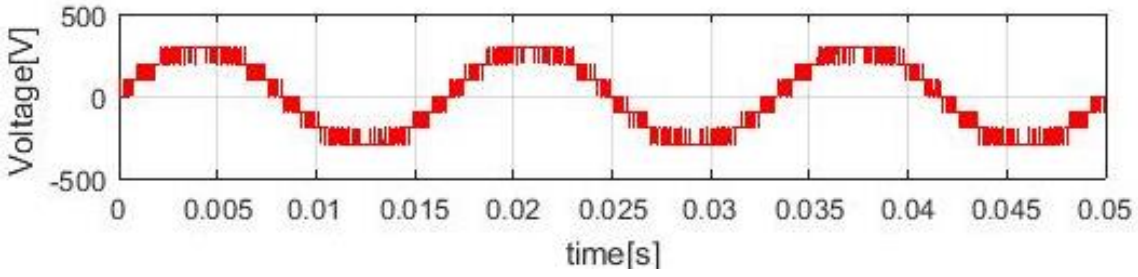

Figure 65: 7-level output voltage waveform

9-level cascaded H-bridge multilevel inverter is connected as shown in Figure 66. Output peak voltage is 400 V as shown in Figure 67 and THD is measured 14%.

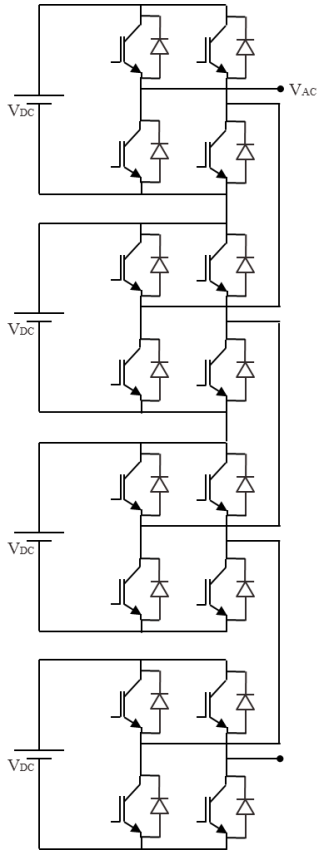

Figure 66: 9-level H-bridge multilevel inverter

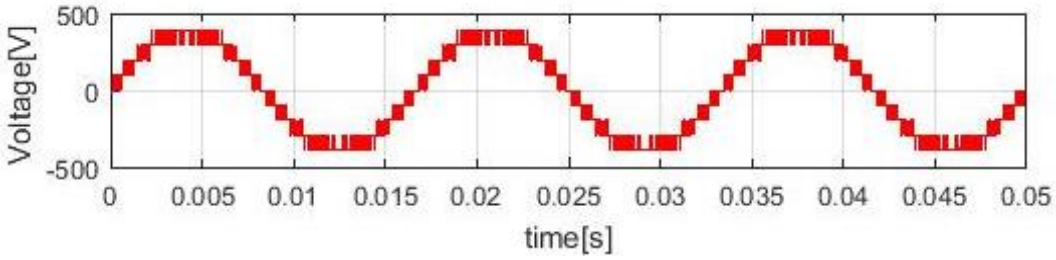

Figure 67. 9-level output voltage waveform

11-level cascaded H-bridge multilevel inverter is connected as shown in Figure 68. Output peak voltage is 500 V as shown in Figure 69 and THD is measured 11.1%.

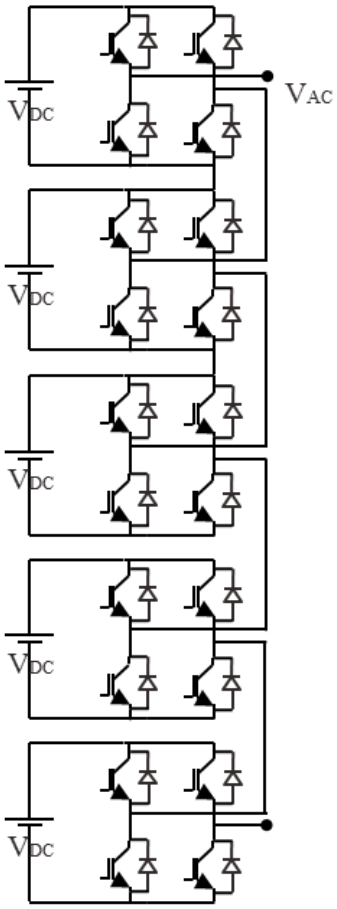

Figure 68: 11-level H-bridge multilevel inverter

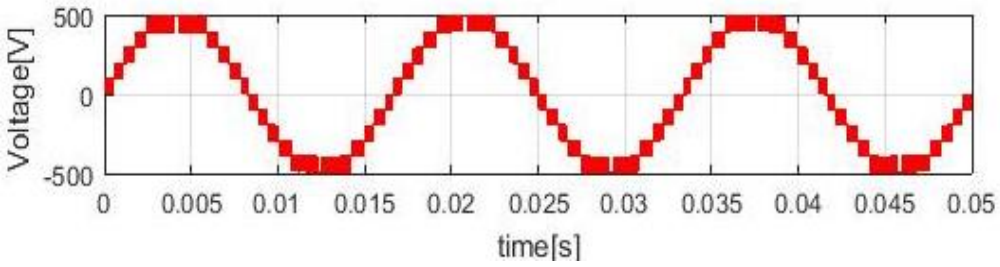

Figure 69: 11-level output voltage waveform

13-level cascaded H-bridge multilevel inverter is connected as shown in Figure 70. Output AC voltage waveform is closer to sine wave with 600 peak voltage as shown in Figure 71 and THD is reduced to 9.2% for 13-level cascaded H-bridge inverter.

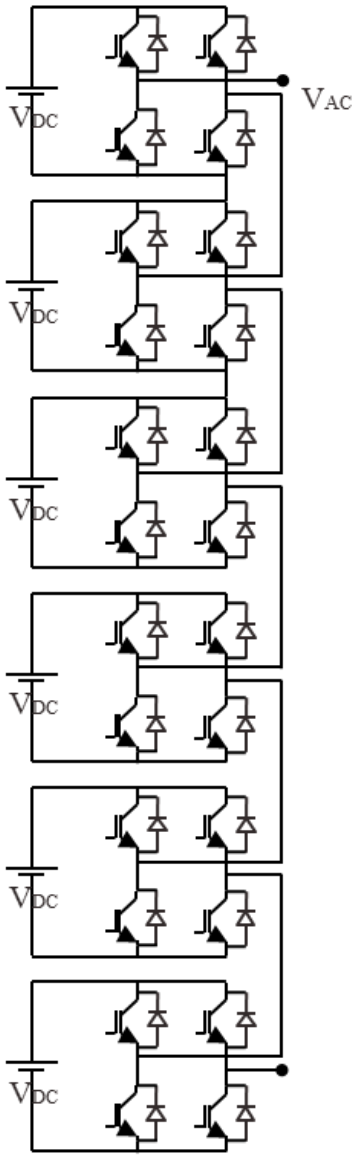

Figure 70: 13-level H-bridge multilevel inverter

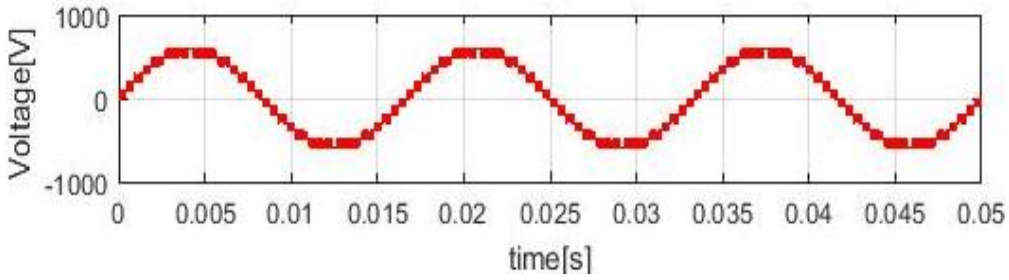

Figure 71: 13-level output voltage waveform

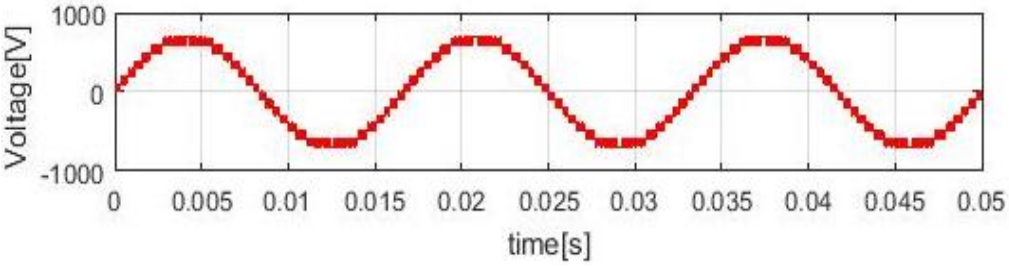

Figure 72: 15-level output voltage waveform

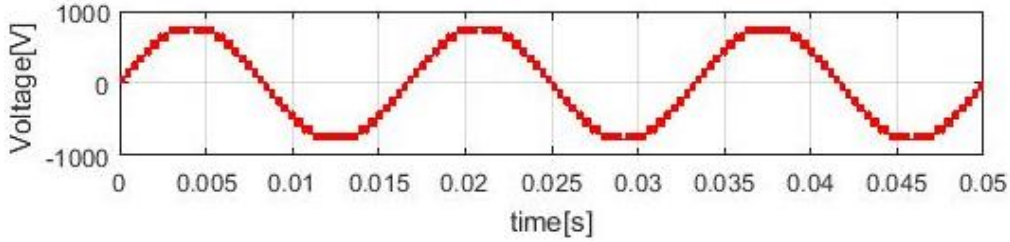

Figure 73: 17-level output voltage waveform

Output voltages waveforms of 15-level and 17-level cascaded H-bridge inverter are almost pure sine wave as shown in Figure 72 and Figure 73 respectively. The harmonic standards limit the utility side harmonic percentage, thus cascaded H-bridge inverter level should be depended on the pulse number of the multipulse rectifier. As explained before, 36-pulse rectifier causes current THD within the limits, thus 13-level H-bridge cascaded inverter should be the best for most of the motor drive applications. Even though increasing the inverter level above 13-level is able to obtain a better output voltage waveform, it is not efficient due to cost and size. THD reduction is not big for 13-level cascaded H-bridge multilevel inverter and higher levels as shown in Figure 74.

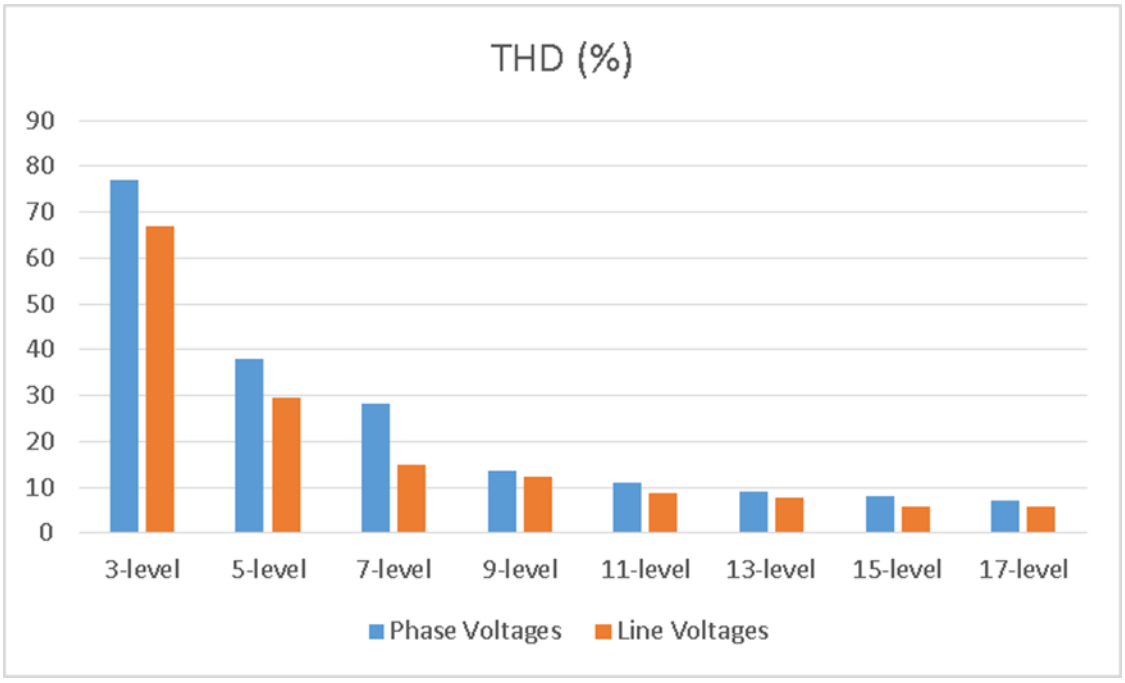

Figure 74: Total harmonic distortion of multilevel inverter

5. CORE LOSSES

Core loss occurs in a magnetic material when the alternating magnetic field is applied to the material. Traditionally, hysteresis and eddy current losses are called as core losses of the material [17, 18]. Core loss equations are ordinarily performed with the varying magnitude and frequency of the magnetic field. Where P_h represents the hysteresis losses, P_e represents the eddy current losses and Pc is the total core loss [18].

$$P_h = k_h f B^{1.5}$$

$$P_e = k_e f^2 B^2$$

$$P_c = P_h + P_e$$

where k_h, k_e are the hysteresis and eddy current coefficients respectively, B is the flux density, f is the frequency of the alternating flux. Core loss coefficients depend on the conductivity and lamination of the material [18]. In order to explain core losses, numerous methods and models have been discussed [18, 19, 20, 21].

5.1 Hysteresis Loss

Hysteresis loss is due to the reversal of magnetization of the material which can be explained on the B-H loop as shown in Figure 75. While the magnetizing force is changed, the magnetic flux is measured in order to obtain the hysteresis loop. H is increased from

zero when the material has never been previously magnetized. When H is increased to point a, core material reaches the magnetic saturation. When the magnetizing force is reduced to zero, still some magnetic flux remains in the material, which is called retentivity point. While H is reversed and increased in the negative direction, flux density becomes zero at point c which is called coercivity. The material will again reach the magnetic saturation point in the opposite direction at point d as the magnetizing force is increased in the negative direction. When the magnetizing force is reduced to zero, equal remanence occurs in the opposite direction at point e. As H is increased, B becomes zero and the loop is completed. In order to remove the remanence in the material, a force is needed which is called coercive force. This coercivity of the material causes heat in the core which is called hysteresis loss [17].

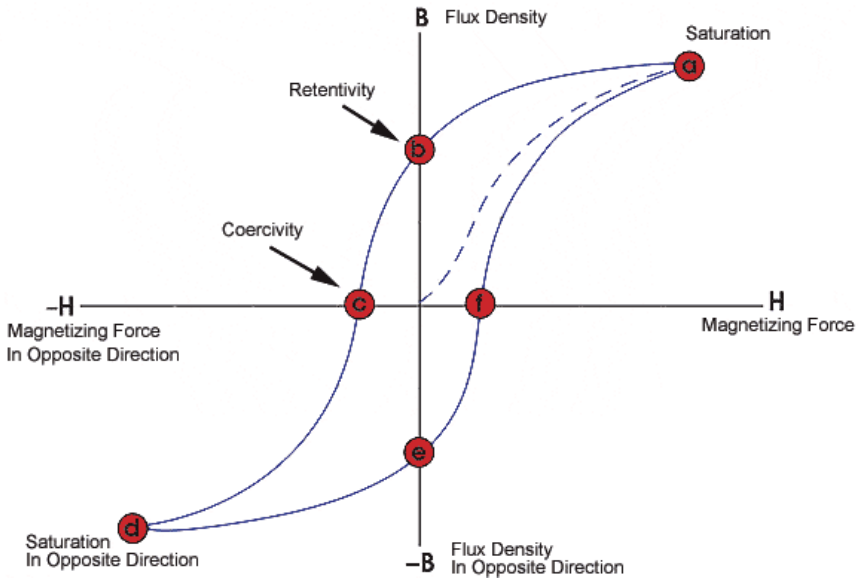

Figure 75: Hysteresis loop adapted from [17]

5.2 Eddy Current Losses

Circulating currents occur in the conducting core material due to the induced voltage in the material called as eddy currents as shown in Figure 76. These currents cause heat in the core material which is called as eddy current losses. Laminated core material is normally used to lower the eddy current losses.

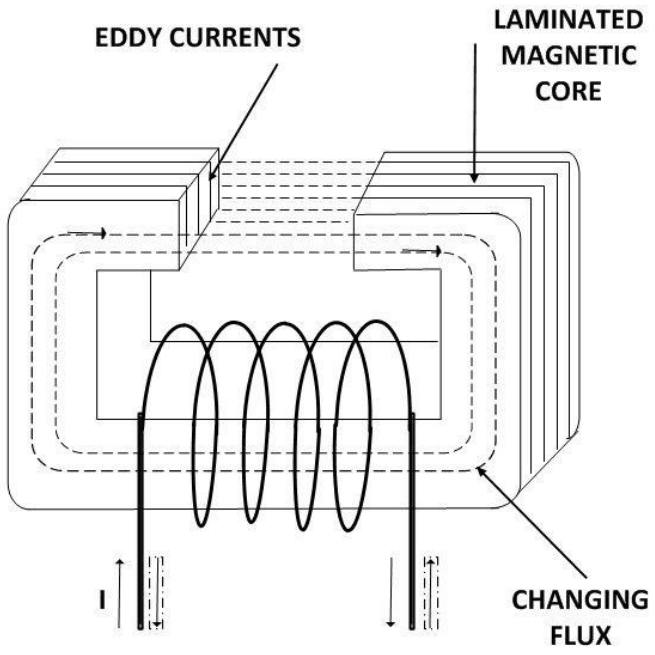

Figure 76: Eddy currents in the laminated magnetic core

6. SIMULATION AND EXPERIMENTAL RESULTS

Simulation results are obtained for both synchronous generator and induction motor and experimental results are obtained for the synchronous generator. MATLAB Simulink and ANSYS Simplorer have been used for harmonic analysis and ANSYS Maxwell FEA has been used for core loss analysis. In order to show the harmonic effects in the synchronous generator and induction motor, MATLAB Simulink, ANSYS Simplorer and ANSYS Maxwell FEA has been co-simulated.

6.1 Core Losses in the Synchronous Generator

In this study, a 5 kVA, 4 poles, 3-phase synchronous generator has been selected. Stator of the synchronous generator has 48 slots as shown in Figure 77.

Figure 77: Stator of the synchronous generator with no windings

12 coils of #17 wired 24 turns each, 4 coils in each phase connected in series as illustrated in Figure 78. Turn span is 9 slots as shown in Figure 79. Black color represents phase A, red color is for phase B and blue color is for phase C.

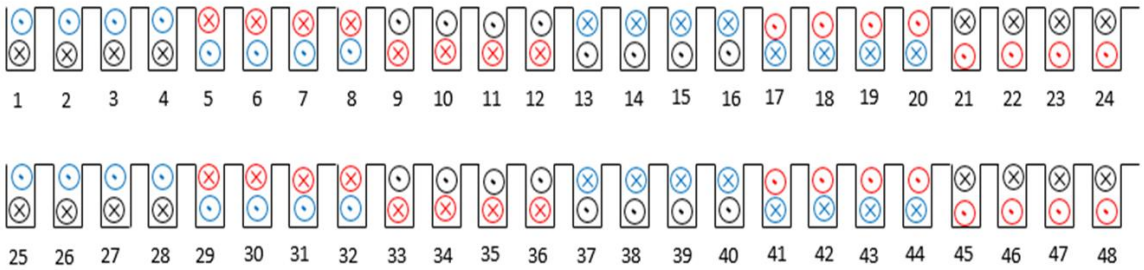

Figure 78: Winding configuration of the stator slots

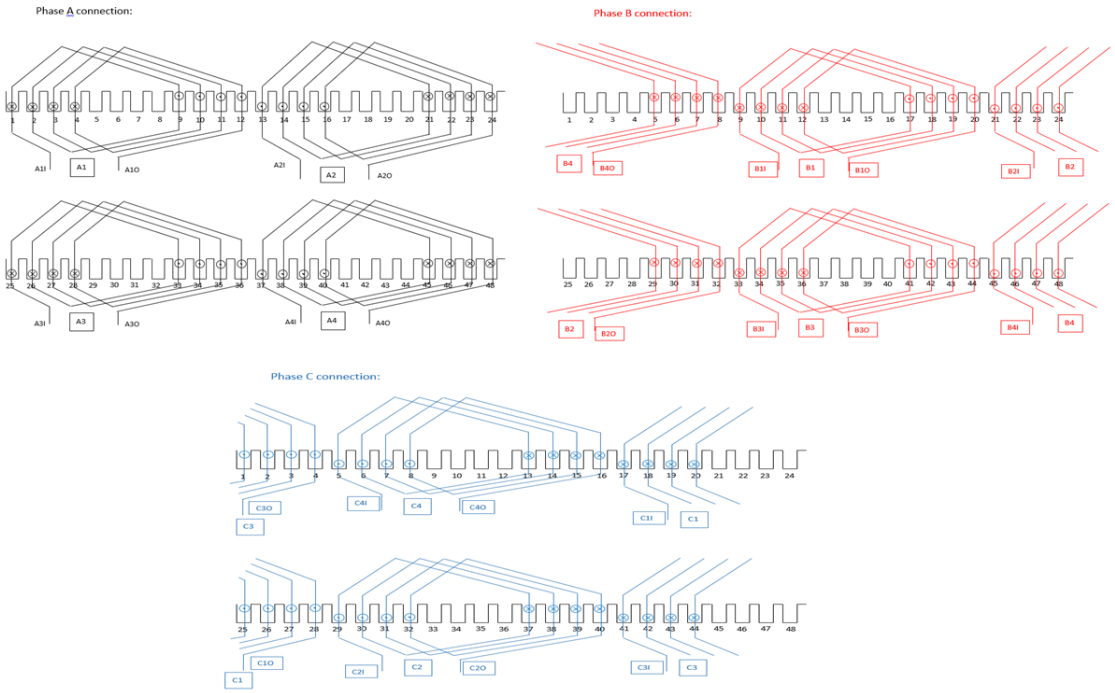

Figure 79: Turn span is 9 slots

Figure 80 shows the Maxwell ANSYS FEA model of the synchronous generator. Synchronous generator has been set to 1800 rpm rated speed for the FEA analysis and in the experiment, 5 kW DC motor has been operated as a prime mover of the synchronous generator to drive it at rated frequency of 60 Hz. DC machine has been driven manually by DC power sources. A force cell has been attached to the bottom of the synchronous generator to measure the force which has been used in the calculation of input power of the synchronous generator as shown in Figure 81.

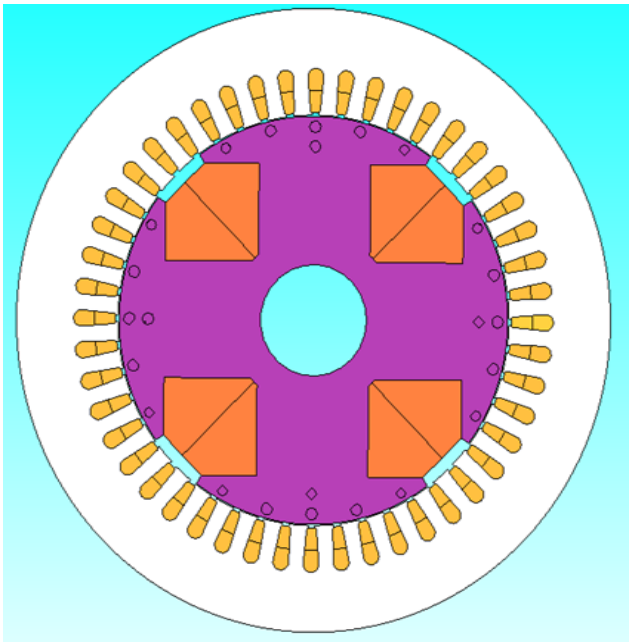

Figure 80: FEA model of the synchronous generator

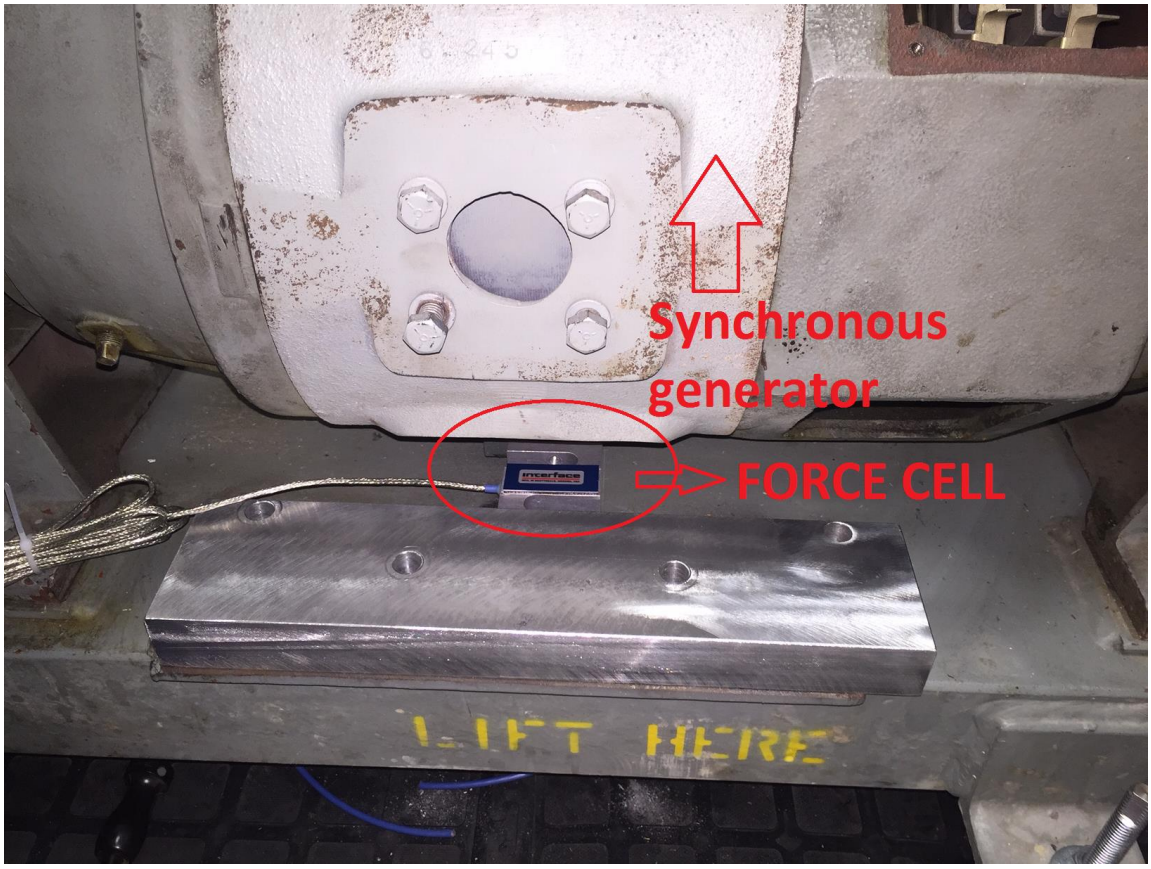

Figure 81: Force cell connection under the synchronous generator

Although simulation study provides the flexibility to obtain more results for numerous configurations, experimental study is limited due to the equipment costs and space. Experimental results have been obtained for the 1 kW, 2 kW and 3 kW output power of the synchronous generator and three different configurations have been applied for each load level. Experimental setup includes a synchronous generator, DC motor, DC power supplies, transformers, 6-pulse rectifiers and the force cell as shown in Figure 82.

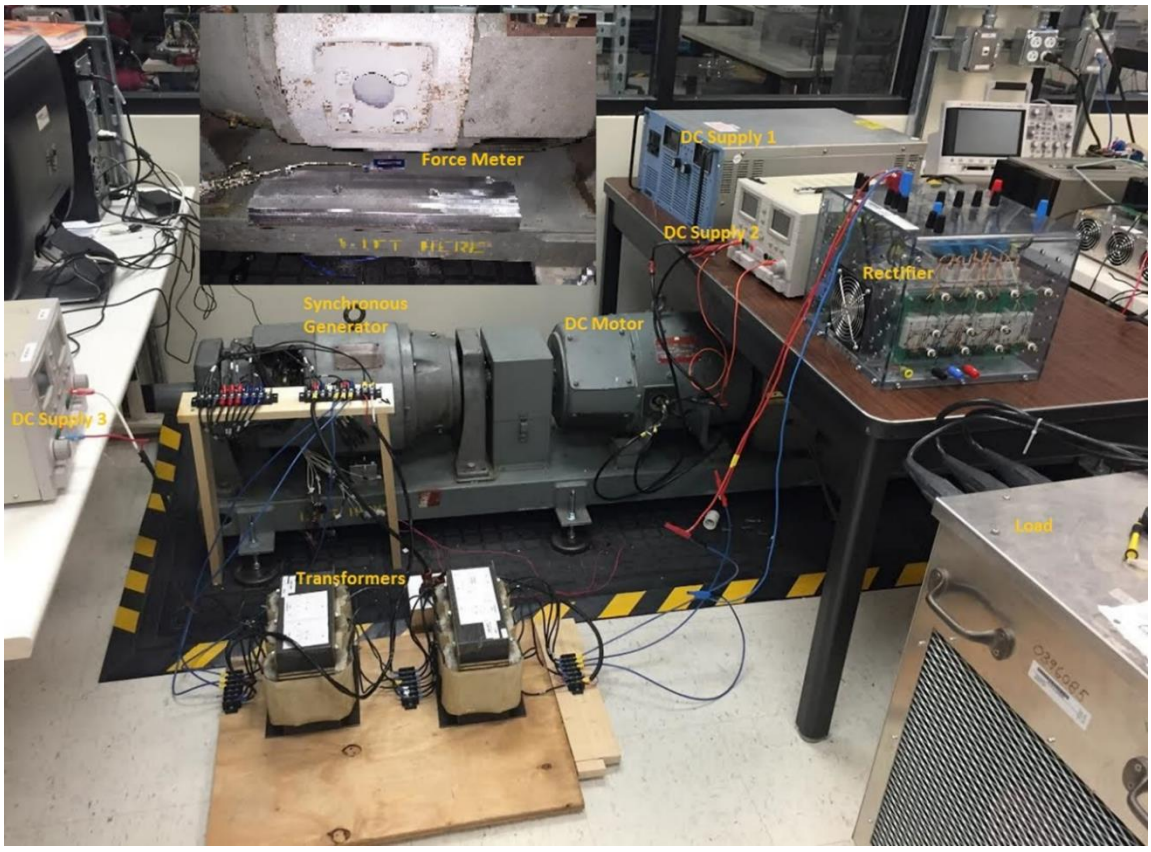

Figure 82: Experiment setup for the synchronous generator

Synchronous generator is connected to a three-phase resistive load without rectifier in configuration 1 as shown in Figure 83. In configuration 2, resistive load is connected to transformer through 6-pulse rectifier as shown in Figure 84. In configuration 3, resistive load is connected wye/delta phase-shifting transformer through 12-pulse rectifier as shown in Figure 85.

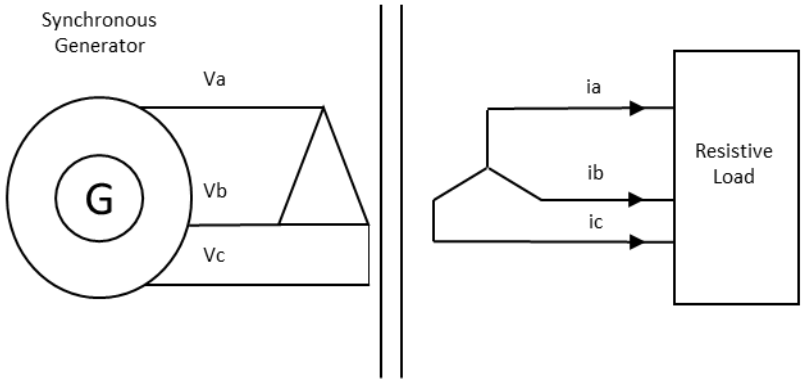

Figure 83: Configuration 1

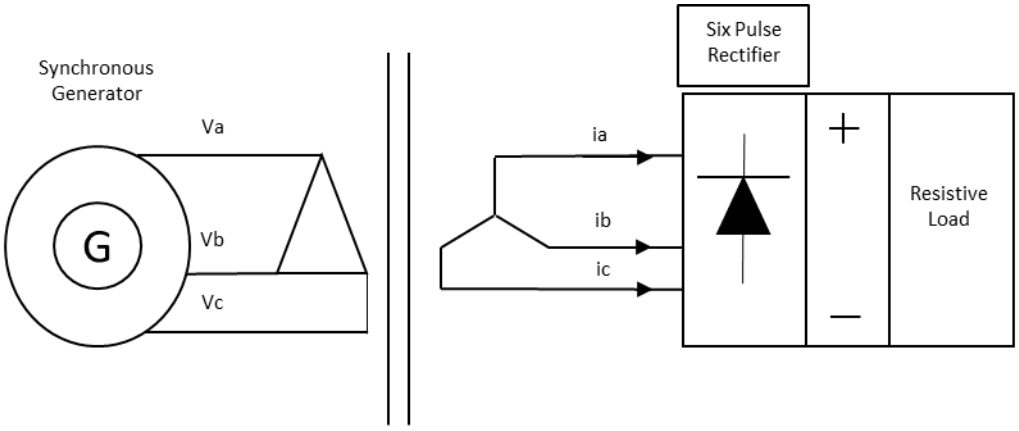

Figure 84: Configuration 2

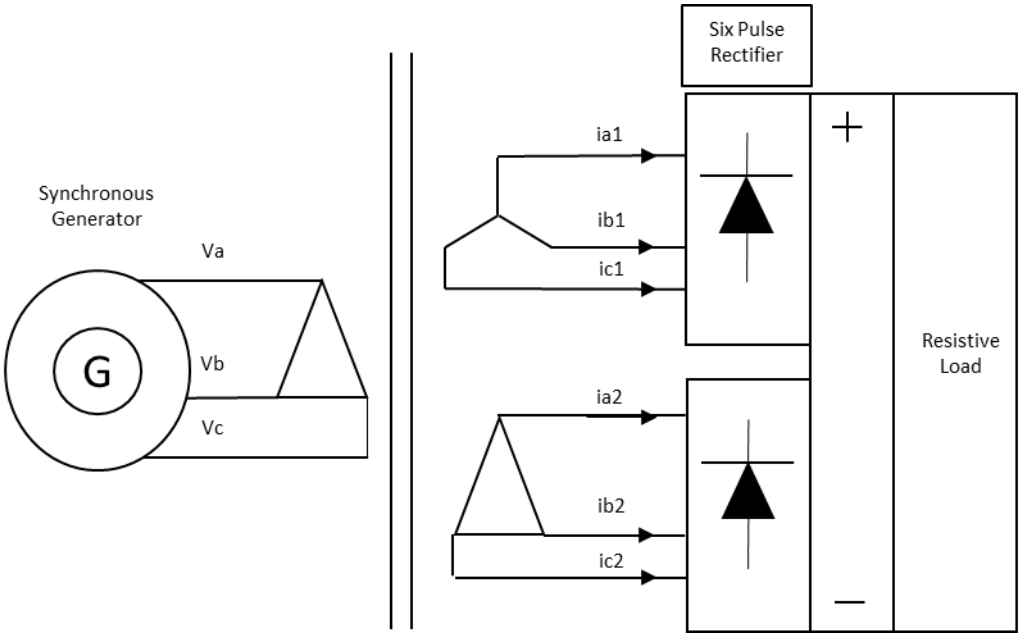

Figure 85: Configuration 3

For each configuration, output power of the synchronous generator has been set to 1 kW, 2 kW and 3 kW power levels. Force of the synchronous generator shaft is measured in order to calculate input power of the generator as shown in Table 6.

Table 6: Measured force

pound-force [lbf]			
	1 kW	**2 kW**	**3 kW**
no rectifier	11.85	21.90	28.75
6-pulse	14.05	22.70	29.70
12-pulse	12.75	22.35	29.10

Measured force values have been multiplied by the distance between the rotor and the force cell which is about 5.5 inches as shown in Table 7.

Table 7: Calculated pound-force-inches

pound-force inches [lbf.in]			
	1 kW	**2 kW**	**3 kW**
no rectifier	65.18	120.45	158.13
6-pulse	77.28	124.85	163.35
12-pulse	70.13	122.93	160.05

Calculated lbf.in values has been multiplied by 0.113 in order to calculate the torque values as shown in Table 8.

Table 8: Calculated torque

Torque [Nm]			
	1 kW	**2 kW**	**3 kW**
no rectifier	7.36	13.61	17.87
6-pulse	8.73	14.11	18.46
12-pulse	7.92	13.89	18.09

Calculated torque values multiply by the angular speed in order to calculate input power of the synchronous generator as shown in table 9.

Table 9: Calculated input power

Input Power [W]			
	1 kW	**2 kW**	**3 kW**
no rectifier	1388.23	2565.59	3368.07
6-pulse	1645.96	2659.31	3479.36
12-pulse	1493.67	2618.31	3409.07

Finally the efficiency is calculated for each configuration by

$$\%efficiency = \frac{Pout}{Pin} x100\%$$

Table 10: Calculated % efficiency of the synchronous generator

% Efficiency			
	1 kW	**2 kW**	**3 kW**
no rectifier	72.03	77.95	89.07
6-pulse	60.75	75.21	86.22
12-pulse	66.95	76.39	88.00

Synchronous generator efficiency results show that more harmonic components occurring at the terminal of the generator cause less efficiency. Applying 12-pulse rectifier in same power level causes less losses and higher efficiency comparing to 6-pulse rectifier configuration. The efficiency is the lowest for 1 kW output power configuration for no load, six-pulse rectifier and 12-pulse rectifier connections as shown in Figure 86. Increasing the load 2 kW causes higher efficiency than 1 kW output power as shown in

Figure 87. Highest efficiency has been achieved at 3 kW output power as shown in Figure 88.

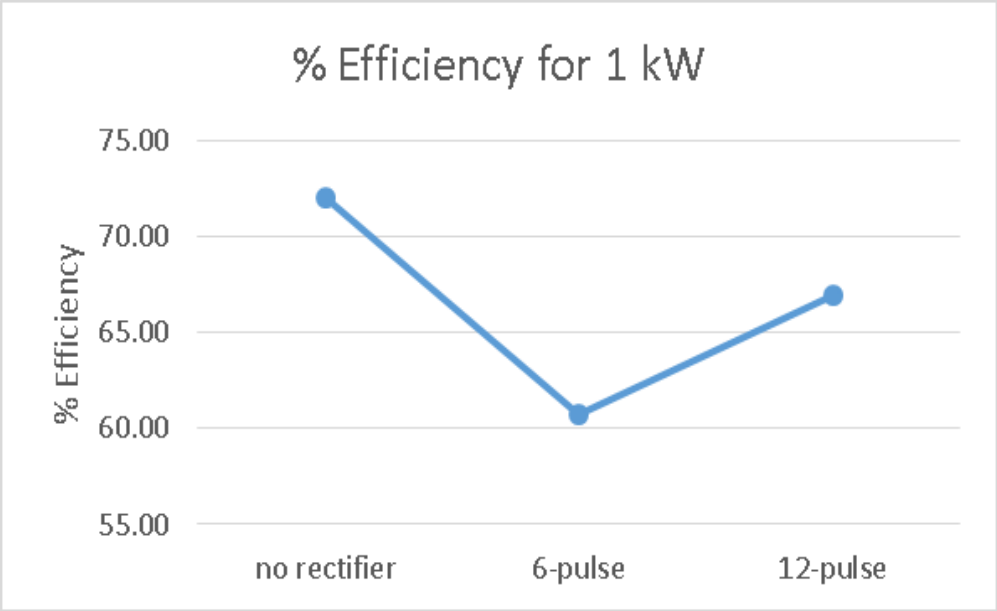

Figure 86: % Efficiency for 1 kW output power

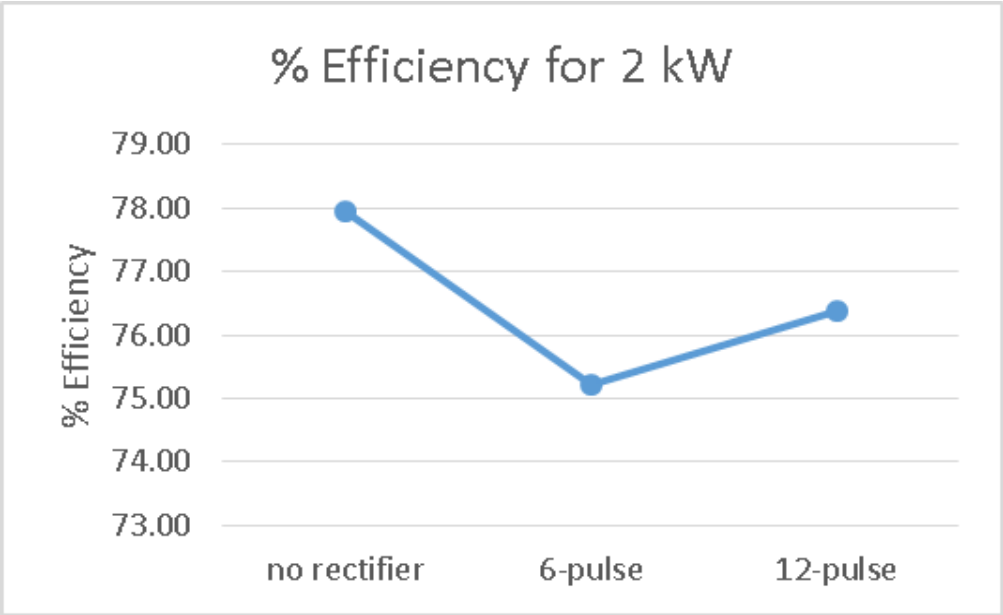

Figure 87: % Efficiency for 2 kW output power

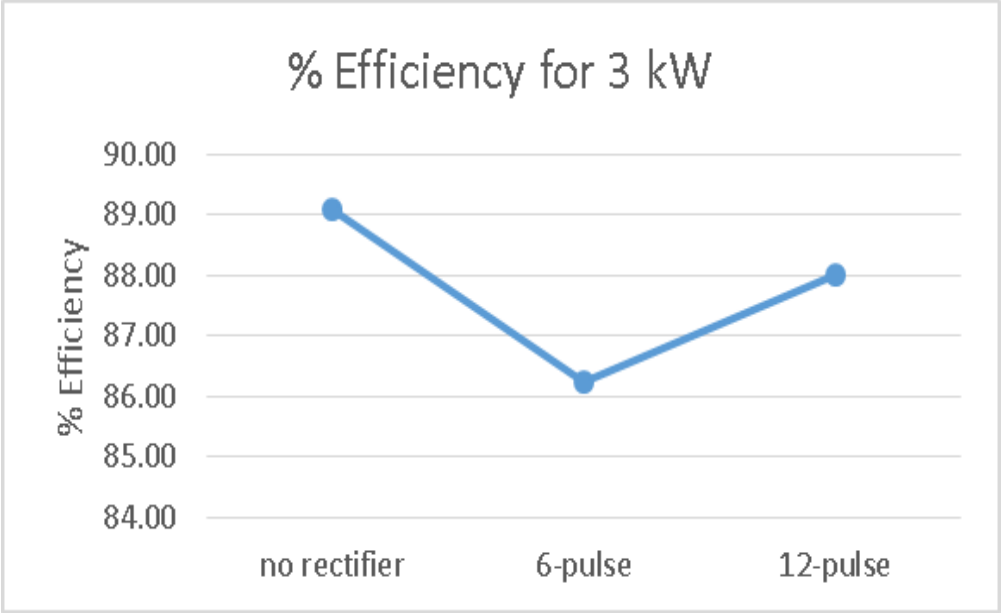

Figure 88: % Efficiency for 3 kW output power

6.1.2 Comparison of the Simulation & Experimental Results

M-19 26 gauge material has been used for the synchronous generator. Total core loss vs. magnetic field by frequency data is given in the data sheet of this material as shown in Figure 89. All core loss values have been entered to FEA for each frequency up to 2 kHz. FEA total core loss values are calculated for all three configurations as shown in Table 11.

Table 11: FEA total core loss values in watts

	FEA		
	no rectifier	**6-pulse**	**12-pulse**
1 kW	89.93	99.58	93.87
2 kW	96.85	111.74	105.54
3 kW	105.96	136.36	117.20

Calculation of experimental total core losses is more challenging since all the calculations must be done manually. Each frequency value of the magnetic field has been matched with the given data in the material data sheet in Microsoft Excel. Core loss coefficients ke and kh are also calculated from the same data in MATLAB. Core losses have been calculated per pound, and the stator weight has been calculated 42 pounds from given generator parameters, thus total core loss has been calculated as shown in Table 11.

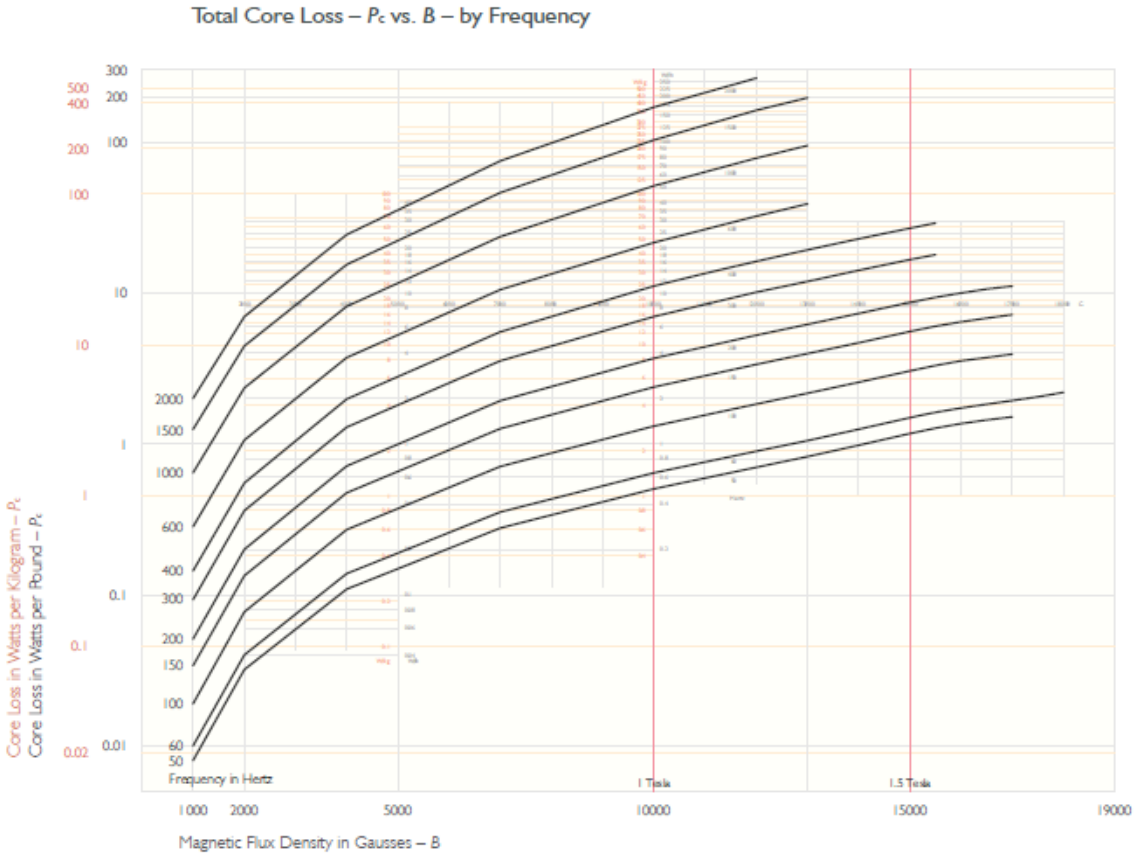

Figure 89: Total core loss Pc vs. magnetic field B by frequency

Total core losses from both FEA and experiment are almost equal in all three configurations for three output power levels of the synchronous generator as shown in Figure 90, Figure 91 and Figure 92 respectively.

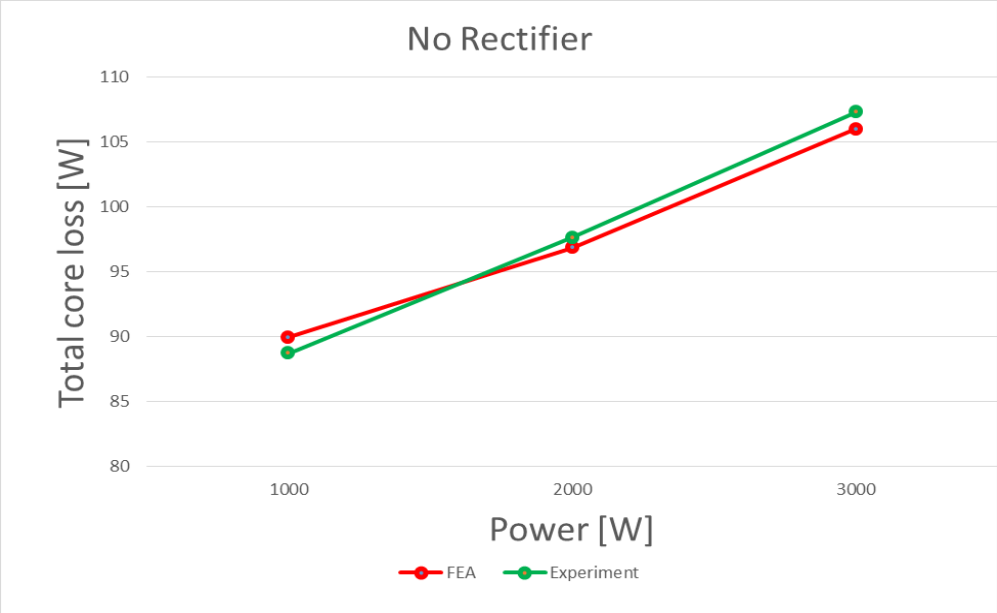

Figure 90: Comparison of total losses when there is no rectifier

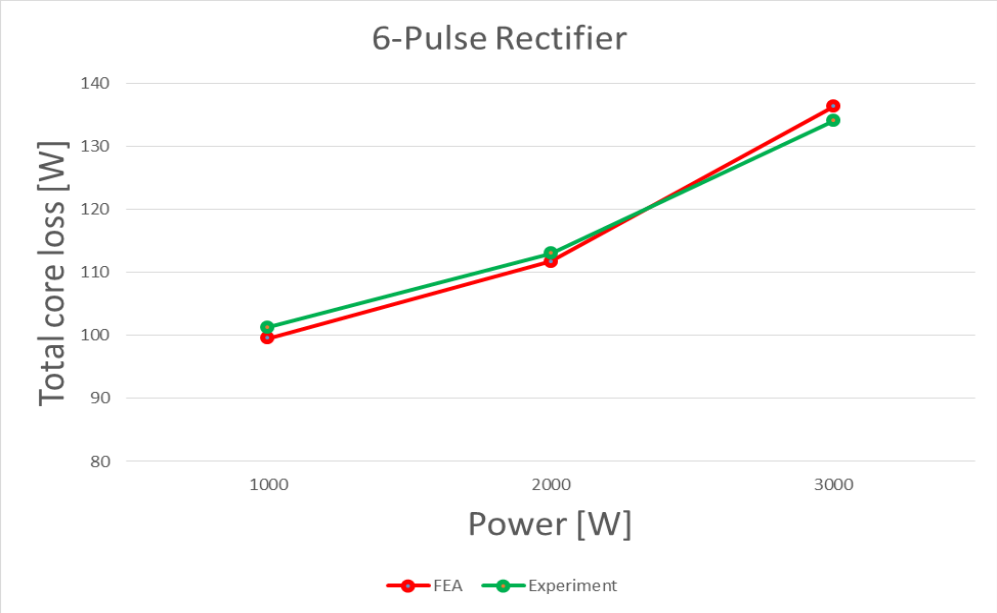

Figure 91: Comparison of total losses when the load connected to six pulse rectifier

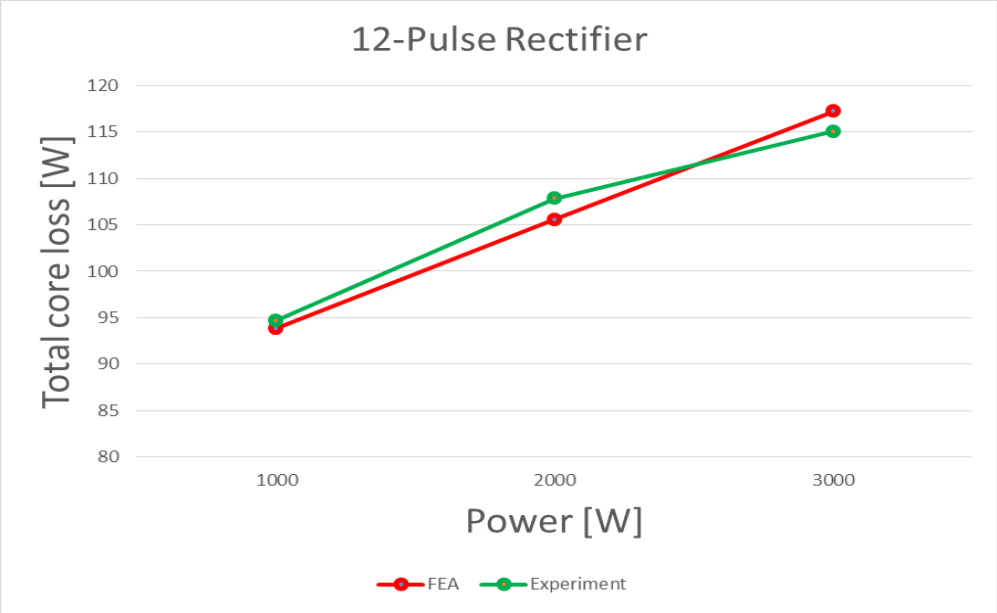

Figure 92: Comparison of total losses when the load connected to twelve pulse rectifier

Same total core loss values have been used for comparison of the same output power levels as shown Figure 93, Figure 94 and Figure 95 respectively. Total core loss is the highest at 6-pulse diode rectifier connection for all power levels due to its high harmonic distortion.

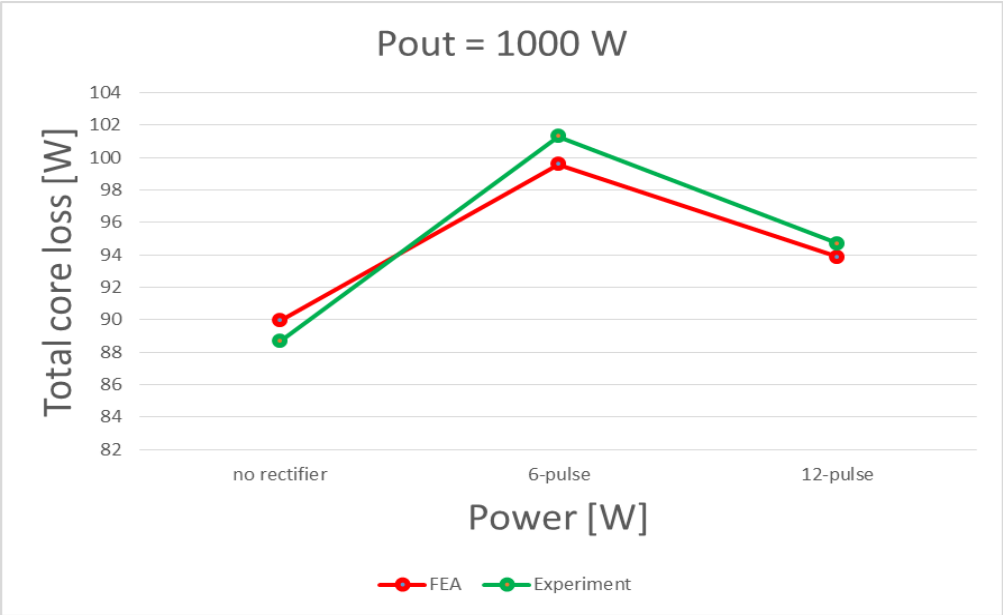

Figure 93: Total core losses at Pout = 1kW

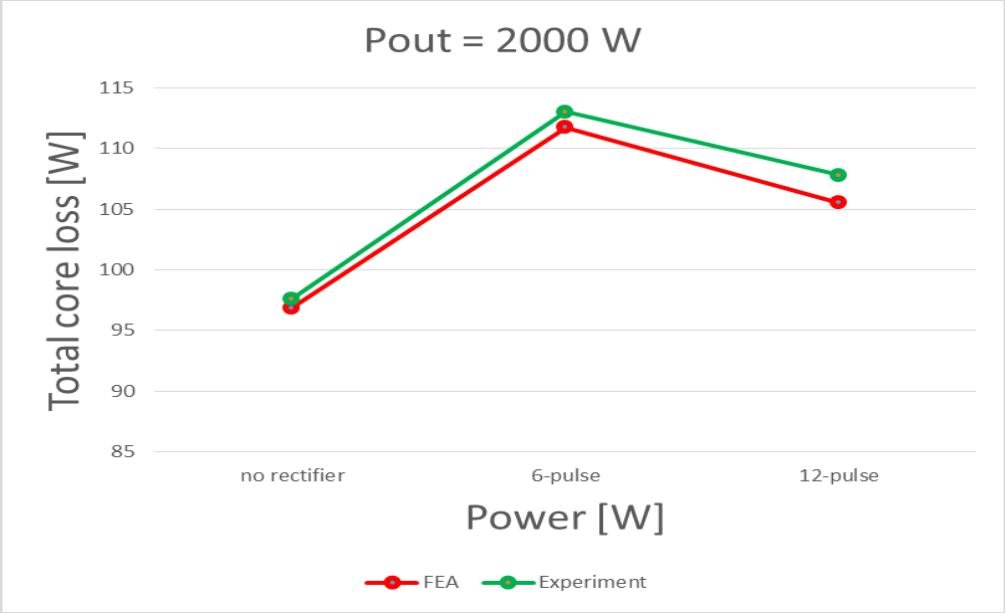

Figure 94: Total core losses at Pout = 2kW

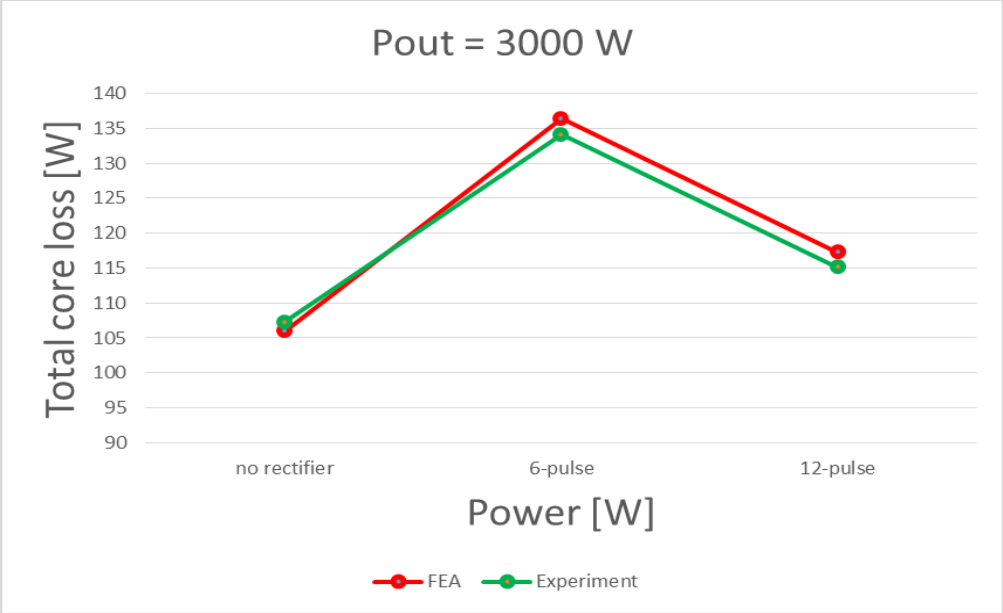

Figure 95: Total core losses at Pout = 3kW

6.2 Total Core Losses in the Induction Machine

In this dissertation, total core losses have been calculated with only FEA simulation. A 7.5 HP, 4 poles, 3-phase squirrel cage induction motor has been performed. Some other parameters of the induction motor are given in Table 12. M19 26 gauge non-oriented silicon steel material has been used for the induction machine as well. Therefore, same total core loss vs. magnetic field values have been used for FEA simulation.

Table 12: Induction motor parameters

Output Power (HP)	7.5
Voltage(V)	460
Current(A)	10.5
Shaft Torque (Nm)	30.88
Efficiency (%)	89.1
Power Factor	0.81
Shaft Speed (rpm)	1730
Minimum Air Gap (inch)	0.016
Rotor Inner Diameter (inch)	1.551
Rotor Outer Diameter (inch)	4.968
Stator Inner Diameter (inch)	5.00
Stator Outer Diameter (inch)	9.00
Number of Stator Slots	36
Stator Winding Coil Pitch	8
Number of Winding Turns per Slot	60
Number of Winding Layers Per Slot	2

Induction machine has been connected to different levels of multilevel inverters through the long cable as shown in Figure 96. Separated DC sources supply for each H-bridge inverter cell which was already described in section 4.2. DC source, multilevel inverter and long cable have been modeled in MATLAB and Simplorer then co-simulated with FEA simulation. Total core loss values have been obtained when no inverter in the system and when 3-level, 5-level, 7-level, 9-level, 11-level, 13-level, 15-level and 17-level multilevel inverters are connected to the motor as shown in Figure 97. The results show that increasing the level of the multilevel inverter causes less harmonic distortions and less total core losses. There is a major difference in total core loss between 3-level and 5-level

connected configurations and less core loss difference occurs between 7-level and other higher level configurations.

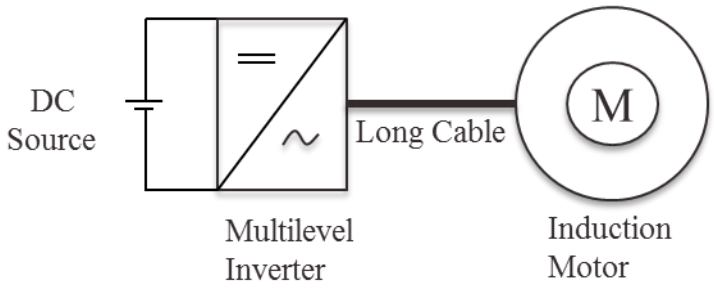

Figure 96: Simplified model of the motor side connection

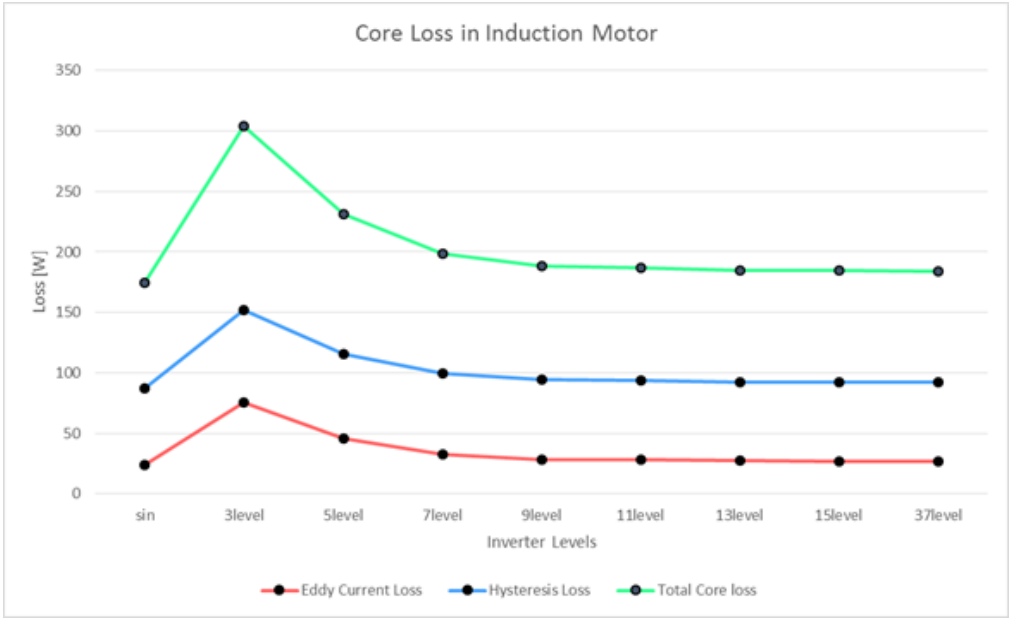

Figure 97: Total core losses in induction motor

7. CONCLUSIONS AND FUTURE WORK

In this dissertation, a system-based modeling and simulations for main power components of a FPSO are built and core losses in synchronous generator and induction motor are studied under different harmonic levels of current. Due to the complexity of the FPSO power system, each components have been simulated and analyzed separately before connecting to each other.

Phase-shifting transformer has a significant role in reducing utility side harmonics which is limited by the harmonic standards. Harmonic analysis has been done on the utility side as well as the motor side.

Core losses are the second largest losses after the copper losses in a machine. Determining these losses is crucial before building large real applications as FPSOs. Lower core losses in a machine can be achieved with a good design of the machine lamination and reducing harmonic distortion at the machine terminals. FEA simulation results show that increasing the pulse number of the VFDs causes lower harmonic distortion which reduces core losses in synchronous generator and induction motor. Simulation results are also supported and proved with the experimental results for the synchronous generator core losses.

Future work can include:

- Resonance issues caused by the subsea cable for core loss analysis of the induction motor.

- Experimental studies for the induction motor.
- Size and cost analysis on a small scale experiment in order to predict real application size and cost.

REFERENCES

[1] R. R. Brown, "FPSO: Lessons learned," IEEE Industry Applications Magazine, vol. 10, pp. 18-23, Mar-Apr 2004.

[2] P. Pandele, E. Thibaut, and E. Meyer, "All-Electrical FPSO Scheme With Variable-Speed Drive Systems," IEEE Transactions on Industry Applications, vol. 49, pp. 1188-1197, May-Jun 2013.

[3] X. D. Liang, S. O. Faried, and O. Ilochonwu, "Subsea Cable Applications in Electrical Submersible Pump Systems," IEEE Transactions on Industry Applications, vol. 46, pp. 575-583, Mar-Apr 2010.

[4] Bluewater 2017, accessed 12 January 2017, http://www.bluewater.com/fleet-operations/what-is-an-fpso/

[5] Oil & Gas and Chemicals, ABB Inc 2017, accessed 12 January 2017, http://new.abb.com/oil-and-gas/systems-and-solutions/electrical-systems/onshore-process-electrification/e-houses

[6] N. Mohan, T. M. Undeland, and W. P. Robbins, Power Electronics Converters, Applications, and Design, third ed. New York: John Wiley & Sons, Inc, 2003.

[7] J. A. Alves, G. Cunha, and P. Torri, "Medium Voltage Industrial Variable Speed Drives," WEG Applications Note, accessed 12 January 2017, http://catalogo.weg.com.br/files/wegnet/WEG-medium-voltage-industrial-variable-speed-drives-technical-article-english.pdf

[8] "IEEE Recommended Practices and Requirements for Harmonic Control in Electrical Power Systems," in IEEE Std 519-1992, ed. New York, NY: The Institute of Electrical and Electronics Engineers, Inc, 1992.

[9] B. Wu, High-Power Converters and AC Drives. Hoboken, New Jersey: A John Wiley & Sons, Inc., Publication, 2006.

[10] M. R. Banaei and P. A. Shayan, "Solution for Selective Harmonic Optimization in Diode-Clamped Inverters Using Radial Basis Function Neural Networks," IET Power Electronics, vol. 7, pp. 1797-1804, Jul 2014.

[11] P. W. Hammond, "A New Approach to Enhance Power Quality for Medium Voltage AC Drives," IEEE Transactions on Industry Applications, vol. 33, pp. 202-208, Jan-Feb 1997.

[12] M. Derakhshanfar, "Analysis of Different Topologies of Multilevel Inverters," Master of Science, Department of Energy and Environment, Chalmers University of Technology, Goteborg, Sweden, 2010.

[13] J. R. Smith and W. W. Bell, "Selection of Transmission-Circuit Models for Power-System Transient Studies," IEE Proceedings-C Generation Transmission and Distribution, vol. 131, pp. 1-4, 1984.

[14] E. Ozkentli, "High Frequency Effects of Variable Frequency Drives (VFD) on Electrical Submersible Pump (ESP) Systems," Master of Science, Electrical Engineering, Texas A&M University, College Station, Texas, 2012.

[15] B. K. Sen and R. L. Wheeler, "Skin Effects Models for Transmission Line Structures Using Generic SPICE Circuit Simulators," Electrical Performance of Electronic Packaging, pp. 128-131, 1998.

[16] Power Feed-Thru Systems & Connectors LLC 2016, accessed 12 January 2017, http://pftsys.com/products.php

[17] P. Parthasaradhy and S. V. Ranganayakulu, "Hysteresis and Eddy Current Losses of Magnetic Material by Epstein Frame Method-Novel approach," The International Journal of Engineering and Science, pp. 85-93, 2014.

[18] Y. C. Chen and P. Pillay, "An Improved Formula for Lamination Core Loss Calculations in Machines Operating with High Frequency and High Flux Density Excitation," Conference Record of the 2002 IEEE Industry Applications Conference, Vols 1-4, pp. 759-766, 2002.

[19] M. Amar and F. Protat, "A Simple Method for the Estimation of Power Losses in Silicon-Iron Sheets under Alternating Pulse Voltage Excitation," IEEE Transactions on Magnetics, vol. 30, pp. 942-944, Mar 1994.

[20] G. Bertotti, F. Fiorillo, and M. Pasquale, "Measurement and Prediction of Dynamic Loop Shapes and Power Losses in Soft-Magnetic Materials," IEEE Transactions on Magnetics, vol. 29, pp. 3496-3498, Nov 1993.

[21] H. Pfutzner, P. Schonhuber, B. Erbil, G. Harasko, and T. Klinger, "Problems of Loss Separation for Crystalline and Consolidated Amorphous Soft Magnetic-Materials," IEEE Transactions on Magnetics, vol. 27, pp. 3426-3432, May 1991.

APPENDIX A

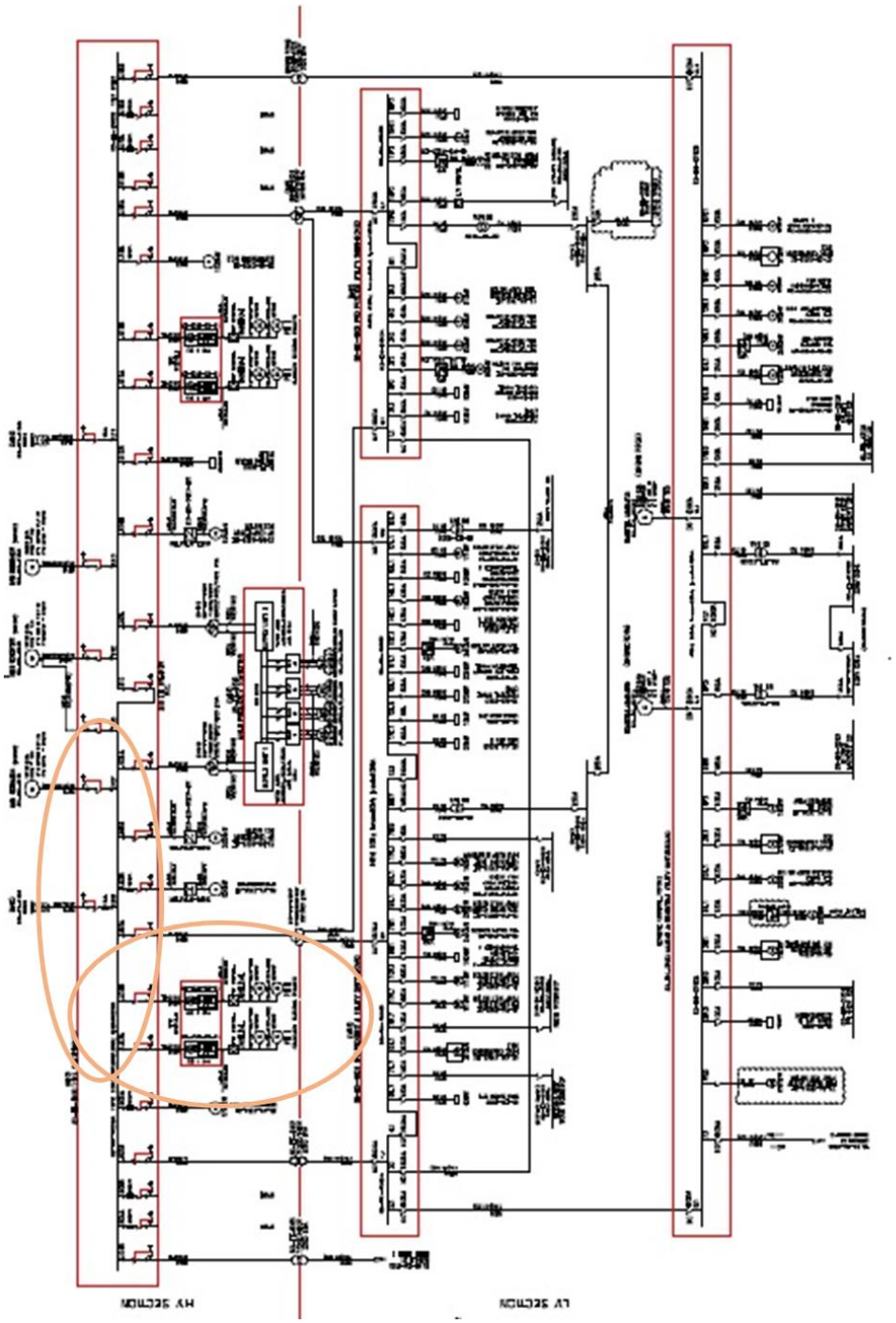

Figure 98: Electric schematic of an FPSO

APPENDIX B

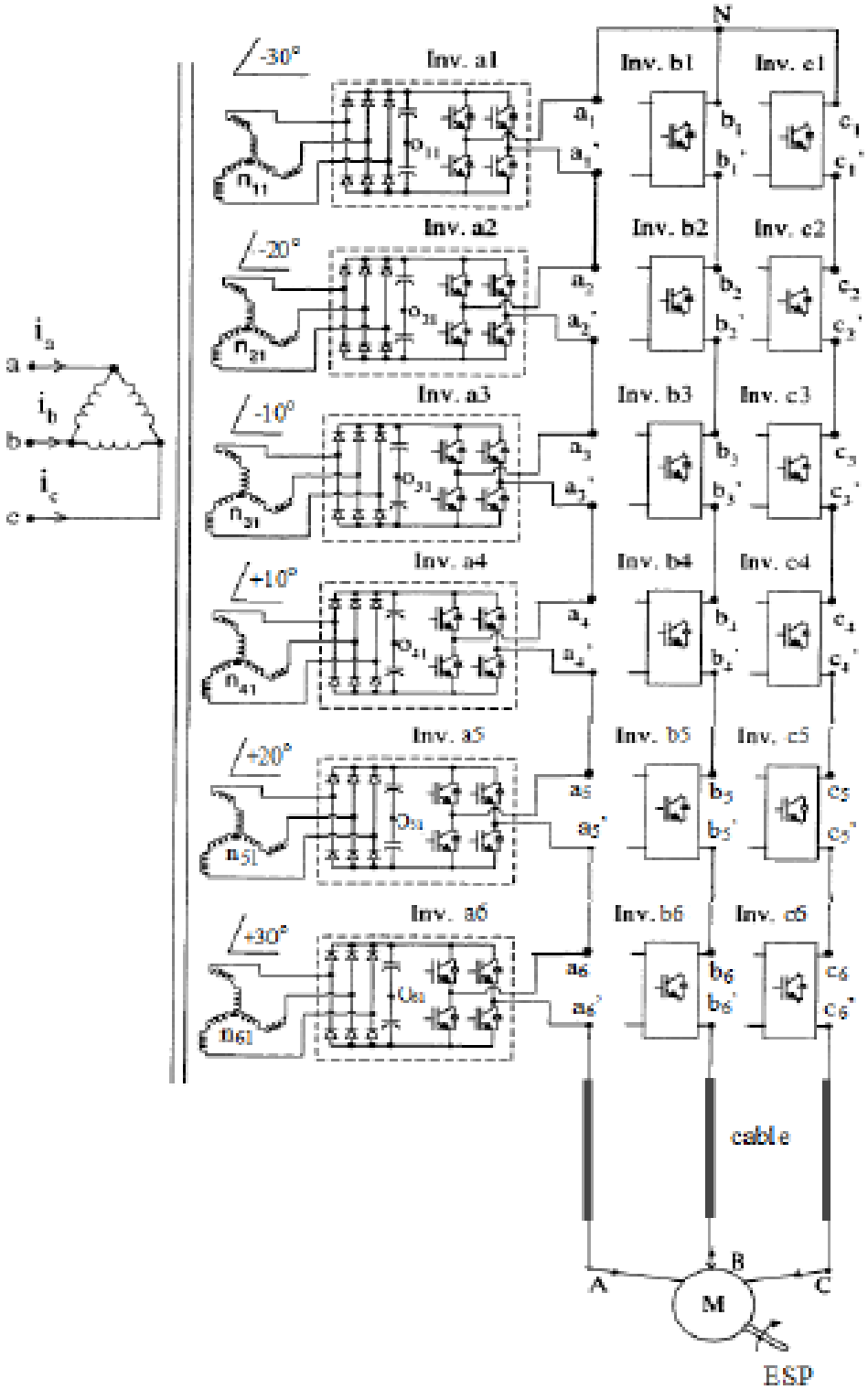
N
-30°
Inv. a1
Inv. b1
Inv. c1
-20°
Inv. a2
Inv. b2
Inv. c2
-10°
Inv. a3
Inv. b3
Inv. c3
+10°
Inv. a4
Inv. b4
Inv. c4
+20°
Inv. a5
Inv. b5
Inv. c5
+30°
Inv. a6
Inv. b6
Inv. c6
a
b
c
cable
A
B
C
M
ESP

APPENDIX C

Table 13: Synchronous generator specifications

Manufacturer	General Electric
Model	5SJ4254Y2Y2
Serial	MF7493B07
Frame	254Z
Rated speed	1800 RPM
Frequency	60 Hz
Rated power	5 kVA
Power factor	0.8
Rated voltage	120/240 V
Phases	3
Rated current	27/13.5 A
Field maximum current	1.2 A
Field rated voltage	125 V
Number of poles	4 Poles
Number of stator slots	48 Slots
Stator slot pitch	7.5°
Stator windings resistance	0.6 Ω/phase
Stator outer diameter	266 mm
Stator inner diameter	175 mm
Stack length	97.35 mm
Rotor windings number of turns	560 turns/pole
Rotor windings connections	Series
Rotor windings total resistance	28 Ω
Rotor outer diameter	174 mm
Shaft diameter	47.5 mm

APPENDIX D

General Cable
exZhellent XXI
EL CABLE DEL NUEVO SIGLO

Offer nº :
Order nº :
Page nº : 1

	MEDIUM & HIGH VOLTAGE CABLES	Units	ITEM1
1	Cable code		0341035
2	Cable type		RHC-2OL
3	Standard		IEC 60502-2
4	Nominal voltage	kV	12/20
5	Nº of cores x C.S.A.		1 x150 mm²
6	Conductor material		Cu
7	Shape		Circular
8	Class / Standard		2 / CEI-60228
9	Nominal diameter	mm	14,95
10	W.B. conductor		YES
11	Swellable semi-conducting tape over conductor		NO
12	Conductor screen material		Extruded semi-conducting layer
13	Nominal radial thickness	mm	1,2
14	Insulation material		XLPE
15	Nominal radial thickness	mm	5,5
16	Nominal diameter over insulation	mm	28,2
17	Insulation screen material (non metallic)		Extruded semi-conducting layer
18	Nominal radial thickness	mm	0,5
19	Swellable semi-conducting tape under metallic screen		NO
20	Insulation screen (metallic)		CWS
21	Nº of wires x Diameter	N x mm	60x0,584
22	Nominal tape thickness / Overlap	mm / %	
23	C.S.A. (Cu wires)	mm²	16
24	W.B. metallic screen (swellable yarn)		YES
25	Swellable tape over metallic screen		NO
26	Metallic / Copolymer tape		NO
27	Nominal total C.S.A. (Cu wires + Metal/Copolymer tape)	mm²	16
28	Metallic sheath bedding material		N/A
29	Nominal radial thickness	mm	
30	Metallic sheath material		N/A
31	Nominal radial thickness	mm	
32	Armour bedding material		N/A
33	Nominal radial thickness / Minimum at any point	mm	
34	Armour material		N/A
35	Nominal under armour diameter	mm	
36	Nº of wires (approx.) x Diameter / Metallic uncounter tape	N x mm	
37	Nominal tapes thickness	mm	
38	Outer sheath material		HDPE
39	Nominal radial thickness / Minimum at any point	mm	2,0 / --
40	Nominal overall diameter	mm	36,8
41	Minimum overall diameter	mm	35,9
42	Maximum overall diameter	mm	37,4
43	Nominal total weight	kg/km	2325
44	Minimum bending radius	mm	609
45	Maximum conductor DC resistance, at 20 ºC	Ohm/km	0,124
46	Star reactance per phase, at 50 Hz	Ohm/km	0,116
47	Capacitance per phase	µF/km	0,252
48	Charging current per phase, at Uo, 50 Hz	A/km	0,949
49	Maximum permanent current rating (*)	A	435 (1) / 340 (2)
50	Maximum conductor temperature in service / in short-circuit	ºC	90 / 250
51	Maximum adiabatic short-circuit current rating (0,1/0,5/1,0 s)	kA	57,8 / 38,5 / 27,4

Figure 99: Cable data sheet

APPENDIX E

VITA

Abdulkadir Bostanci received his B.S. and M.S. degrees from Yildiz Technical University, Istanbul, Turkey in 2006 and 2008 respectively. Both degrees are in electrical engineering. He joined the doctoral program of the Department of Electrical Engineering at Texas A&M University and received his Ph.D. in May 2017.

He can be reached at akadbos@gmail.com or through Prof. Hamid A. Toliyat, Department of Electrical and Computer Engineering, Texas A&M University, College Station, Texas, 77843-3128.